Master Thesis

Investigation of the effect of prior austenite grain size and transformation temperature on the phase transformation kinetics of bainite using in-situ synchrotron XRD

Anniken Tefs

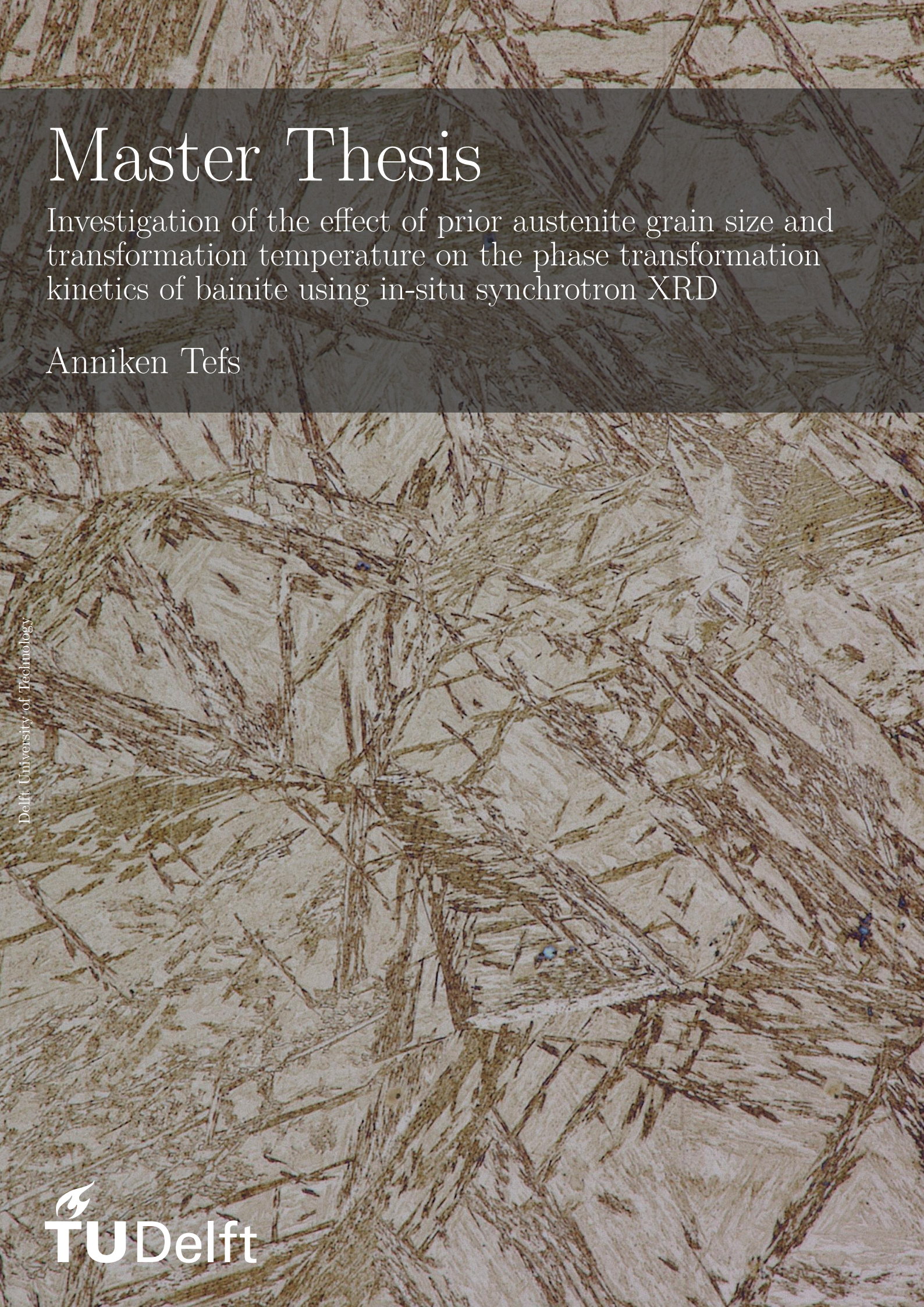

Delft University of Technology

TU Delft

Investigation of the effect of prior austenite grain size and transformation temperature on the phase transformation kinetics of bainite using in-situ synchrotron XRD

by

Anniken Tefs

to obtain the Master of Science (M.Sc.) degree in Materials Science and Engineering,
at the Delft University of Technology,
to be defended publicly on February 19, 2025 at 10:15 AM.

Student number:	5857112	
Project duration:	May 13, 2024 – February 19, 2025	
Thesis committee:	Dr. Daniel dos Santos Avila,	TU Delft Department of MSE, supervisor
	Prof. Dr. Maria Santofimia Navarro,	TU Delft Department of MSE, supervisor
	Dr. Poulumi Dey,	TU Delft Department of MSE
	Dr. Ir. Niels van Dijk,	TU Delft Department of FAME (TNW)

Cover: Bainite transformed at 380°C in a low-carbon high-silicon steel.

TU Delft

Acknowledgements

Finishing the master's thesis is the final step toward obtaining the Master of Science degree in Materials Science and Engineering. This accomplishment is a very special one for me, as I started this journey 2.5 years ago with little background in materials science. The first months of the program were particularly challenging, and at that time, I could not have imagined that I would investigate the phase transformation kinetics of bainite using data from in-situ synchrotron XRD experiments in my master thesis project. Throughout the thesis project, I enjoyed studying the phase transformation kinetics of bainite and it was fascinating to develop in-depth knowledge in this field with the guidance of my supervisors.

First of all, I would like to express my gratitude to my supervisors, Dr. Daniel dos Santos Avila and Prof. Dr. Maria Santofimia Navarro, for supporting me throughout the thesis project with weekly discussions, critical feedback and valuable suggestions to guide me to a successful completion of the master thesis. A special thanks is given to Dr. Daniel dos Santos Avila, who dedicated many hours to help me developing in depth understanding and critical thinking over the past nine month of research.

Furthermore, I would like to thank Prof. Dr. Jilt Sietsma for reviewing and discussing the results of my analyses and giving suggestions for the progress of my thesis. Additionally, thanks to Prof. Dr. Leo Kestens, for facilitating the EBSD measurements at Ghent University. My appreciation also goes to Dr. Tuan Nguyen Minh, who performed the EBSD measurements and determined the prior austenite grain sizes of the specimens in his weekends to support me staying within the timeline of my thesis.

Finally, special thanks are given to my family and friends, who supported and believed in me throughout the time of my master master's studies. Their encouragement and confidence in my ability to complete this journey successfully have meant the world to me.

Abstract

Studies on the effect of the prior austenite grain size on the phase transformation kinetics of bainite are contradictory. Literature explains these contradictions by the presence of two different types of nucleation sites, the prior austenite grain boundaries and the tips of previously formed bainitic ferrite sub-units. The difference in their activation energies for nucleation, ΔQ, is known to determine whether the phase transformation kinetics of bainite are accelerated by prior austenite grain refinement or coarsening. However, the factors that influence ΔQ are not entirely understood, which is the reason why the contradictory results regarding the effect of the prior austenite grain size on the phase transformation kinetics of bainite observed in the different studies cannot be explained yet.

This master thesis investigates the effect of the prior austenite grain size on the phase transformation kinetics of bainite at different transformation temperatures in a low-carbon high-silicon steel. The experiments were divided into two groups, with one group consisting of specimens with finer prior austenite grains and one with coarser prior austenite grains. Specimens were transformed to bainite at three different isothermal transformation temperatures, 440 °C, 410 °C and 380 °C. Bainite formation was investigated by in-situ synchrotron XRD experiments performed at DESY to study the evolution of the phase fractions, lattice parameters and microstrains of bainitic ferrite and austenite. Furthermore, microstructure investigations on the specimens transformed at DESY and additional interrupted quenching experiments were conducted to understand the effect of the prior austenite grain size and the isothermal transformation temperature on the microstructure and the sheaf morphology formed in the early stages of the phase transformation. Finally, simulations were performed to determine the effect of the prior austenite grain size and the transformation temperature on ΔQ.

The experiments showed that, by decreasing the transformation temperature, the phase transformation kinetics of the group with fine prior austenite grains were decelerated, whereas the phase transformation kinetics of the group with coarse prior austenite grains were accelerated. The simulations exhibited an increase in ΔQ as the isothermal transformation temperature was decreased, indicating that sheaf growth by successive nucleation events at the tips of previously formed sub-units becomes increasingly prevalent. While the specimens with coarse prior austenite grains provide more potential nucleation sites at the tips of previously formed sub-units, the specimens with fine prior austenite grains provide more nucleation sites for grain boundary nucleation, which explains the reverse effect of the transformation temperature on the phase transformation kinetics of the two experiment groups. Microstructure observations have shown that the effect of the transformation temperature on processes, such as carbon partitioning and the transition from upper to lower bainite, could play an important role in explaining the observed effect of the prior austenite grain size on the phase transformation kinetics of bainite.

Contents

List of figures

List of tables

Nomenclature

Abbreviations

AHSS	Advanced high-strength steels
APT	Atom probe tomography
BCC	Body-centered cubic
BCT	Body-centered tetragonal
DESY	Deutsches Elektronen-Synchrotron
EBSD	Electron backscatter diffraction
FCC	Face-centered cubic
IQ	Interrupted quenching
NIST	National Institute of Standards and Technology
OM	Optical microscopy
PAG	Prior austenite grain
Q&P	Quench and partitioning
SEM	Scanning electron microscopy
TRIP	Transformation induced plasticity
TTT	Time-temperature-transformation
TWIP	Twinning induced plasticity
XRD	X-ray diffraction

Symbols

Symbol	Unit	Definition
2θ	[°]	Diffraction angle of X-rays
α	-	Bainitic ferrite
γ	-	Austenite
γ^+	-	Carbon-rich austenite
ΔG_m	[J/mol]	Maximum change in Gibbs free energy for ferrite nucleation
$\Delta G^{\gamma\rightarrow\alpha}$	[J/mol]	Change in Gibbs free energy during diffusionless bainite formation
ΔQ	[J/mol]	Difference in activation energy for grain boundary and autocatalytic nucleation of bainite
Δt	[s]	Difference in time required to form 45 wt% of bainitic ferrite
λ	[Å]	Wavelength
σ	[J/m^2]	Interfacial energy per unit area
A_{c1}	[°C or K]	Temperature at which the steel starts to transform to austenite on heating
A_{c3}	[°C or K]	Temperature at which the steel finishes to transform to austenite on heating
B_s	[°C or K]	Bainite start temperature
D	[m^2/s]	Diffusion coefficient
d_γ	[µm]	Prior austenite grain size
E	[eV]	Beam energy
G^α	[J/mol]	Gibbs free energy of bainitic ferrite
G^α_m	[J/mol]	Gibbs free energy of bainitic ferrite at the condition of maximum free energy reduction
G^γ	[J/mol]	Gibbs free energy of austenite
G^γ_m	[J/mol]	Gibbs free energy of austenite at the condition of maximum free energy reduction
G_N	[J/mol]	Universal nucleation function

Symbol	Unit	Definition
G_{SB}	[J/mol]	Stored energy of bainite
I	[counts]	Peak intensity
M_s	[°C or K]	Martensite start temperature
Q_A	[J/mol]	Activation energy for autocatalytic nucleation of bainitic ferrite
Q_{GB}	[J/mol]	Activation energy for grain boundary nucleation of bainitic ferrite
R	[J/molK]	Gas constant
T	[°C or K]	Temperature
T_0	[°C or K]	Temperature at which $\Delta G^{\gamma\rightarrow\alpha}$ is zero
T_0'	[°C or K]	Temperature at which $\Delta G^{\gamma\rightarrow\alpha}$ equals -G_{SB}
T_h	[°C or K]	Temperature at which ΔG_m equals G_N
$t_{45wt\%}$	[s]	Time required to form 45 wt% of bainitic ferrite
u'	[nm]	Bainitic ferrite sub-unit thickness
v	[m/s]	Lengthening rate of bainitic ferrite plates
V_m	[m^3/mol]	Molar volume of ferrite
WB_s	[°C or K]	Widmanstätten and bainite start temperature
x_0	-	Nominal mole fraction of carbon in the steel alloy
$x^{\alpha\gamma}$	-	Mole fraction of carbon in bainitic ferrite at paraequilibrium with austenite
$x^{\gamma\alpha}$	-	Mole fraction of carbon in austenite at paraequilibrium with bainitic ferrite

1 Introduction

Materials used in automobile applications have to satisfy a complex set of requirements. Besides passenger safety, material and manufacturing costs are some of the most important ones. Nowadays, the aim to reduce fuel consumption, and hence greenhouse gas emissions, makes the development of materials for the automobile industry even more challenging [1, 2]. Therefore, automobile and steel manufacturers started to develop advanced high-strength steels (AHSS). Figure 1 plots two of the most important material properties that are to be improved with the development of AHSS: tensile strength and elongation [2, 3]. Both properties are known to be antagonistic, which makes their simultaneous improvement challenging. Besides these two properties, the material's yield strength and lightweight design are of high importance and thus are considered during the development [1].

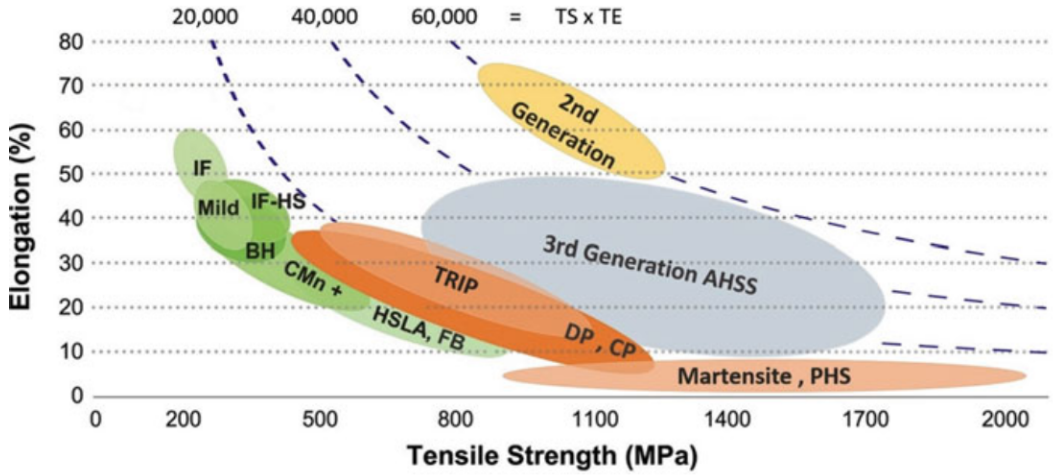

Figure 1: Representation of multiple steel grades in an elongation vs. tensile strength diagram [2].

There are three generations of advanced high-strength steels, with the third one being currently under development. The first generation of AHSS started with the development of dual-phase steels and steels deforming by the transformation induced plasticity (TRIP) effect, which are also known as TRIP steels [1]. With the focus on improving ductility, high-manganese-containing steels that deform by twinning induced plasticity (TWIP) have been developed in the second generation of AHSS. However, their low yield strength, poor weldability and high costs limit their use in automobile manufacturing to very specific components. Nowadays, the development of the third generation of AHSS is in progress, which includes quench and partitioning (Q&P) steels, duplex medium-Mn steels and carbide-free bainitic steels [2].

As a phase providing favorable mechanical properties, bainite is often used as a microstructure constituent of many different steel types, such as complex phase steels, bainitic multiphase steels or Q&P [3]. As part of the third generation of AHSS, the combination carbide-free bainite and retained austenite has been developed to produce steels providing high formability while at the

same time possessing high strength [4, 5]. Their microstructural features, consisting of carbide-free plate-shaped bainitic ferrite and carbon enriched retained austenite, have been observed to improve the mechanical performance of steels significantly. The carbide-free bainitic ferrite improves the mechanical properties by increasing the steel's strength due to its high dislocation density and its uniform, fine plate-shaped microstructure. Furthermore, the retained austenite enhances the steel's ductility, since it enables deformation by the TRIP effect. The properties of bainitic steels depend on size, morphology and fraction of bainitic ferrite and retained austenite, as well as on the austenite stability at room temperature [6, 7].

The production of carbide-free bainitic steels starts with an austenitization step, followed by rapid cooling to the isothermal holding temperature. During isothermal holding bainitic ferrite forms and carbon partitioning takes place. The partitioning process results in an increased carbon concentration in the remaining austenite, which can be retained at room temperature if it is sufficiently enriched in carbon. After isothermal holding, the steel is quenched to room temperature. From an industrial point of view, the acceleration of the bainitic phase transformation is favorable, since it decreases the steel's manufacturing time and costs [4, 8]. The development of economical manufacturing routes, resulting in optimal mechanical properties requires a detailed understanding of the isothermal bainitic phase transformation and carbon partitioning process.

Therefore, the master thesis aims to investigate the prior austenite grain size and the isothermal transformation temperature as two of the factors that affect the phase transformation kinetics of bainite. The work of the thesis is divided into seven sections. In section 2 a comprehensive literature review is provided to develop a profound understanding on the phase transformation mechanism of bainite and the factors influencing its phase transformation kinetics. Furthermore, the literature review is meant to uncover research gaps, part of which are investigated in the master thesis. Section 3 describes the experimental procedure applied to investigate the defined research objectives, followed by section 4, which presents the results observed during the experiments. Subsequently, the results are discussed in section 5. The challenges and limitations of the thesis are given in section 6. Finally, section 7 summarizes the conclusions and recommendations for future research based on the results and discussions provided in the previous sections.

2 Literature review

2.1 Microstructure of bainite

In general, bainite can be described as a microstructure consisting of bainitic ferrite plates, which are separated by carbides [9]. Its formation can be observed in a temperature range between 250 °C and 550 °C. So-called carbide-free bainite forms under conditions in which carbide precipitation between the bainitic ferrite plates is inhibited, which results in carbon enrichment of the remaining austenite as the phase transformation progresses. Austenite that is sufficiently enriched in carbon becomes metastable at room temperature, while the unstable part transforms into martensite during final quenching. Therefore, retained austenite and martensite can be part of the microstructure of carbide-free bainitic steels [10].

Bainite forms in an intermediate temperature range between the reconstructive pearlite formation and the displacive martensite formation [9]. Figure 2 depicts a schematic of a Time-Temperature-Transformation (TTT) diagram of steel with two separate C-curves. While the upper C-curve is associated with the transformation of austenite to phases such as ferrite or pearlite, which progress in a reconstructive manner [11], the lower C-curve is associated with the transformation of austenite to bainite. In contrast to the schematic depicted in Figure 2, overlapping C-curves can be observed for plain carbon steels [12]. Researchers found bainite to exhibit features of both pearlite and martensite transformation, which made the bainitic phase transformation mechanism a subject of debate for decades [9]. Therefore, two theories have been developed in the past. While one of them describes the transformation from austenite to bainite as a diffusional phase transformation, the other one describes it as diffusionless [6, 13]. To gain a better understanding of both theories, section 2.2 is dedicated to discuss them in more detail.

2.1.1 Upper and lower bainite

During bainite formation, face-centered cubic (FCC) austenite decomposes into a fine aggregate of body-centered cubic (BCC) ferrite plates and carbides. Depending on the transformation temperature, bainite can be divided into upper and lower bainite [12, 14]. The following explanations of the formation mechanisms of upper and lower bainite are based on the assumptions of the diffusionless theory. Upper bainite generally forms during transformation in the temperature range between 400 °C and 550 °C [14]. Figure 3 a) shows the plate morphology of bainitic ferrite in upper bainite, surrounded by fresh martensite, which has formed during final cooling to room temperature [14]. The microstructural features of upper bainite result from its two characteristic transformation stages. In the first stage, bainitic ferrite nucleates at the prior austenite grain boundaries. The diffusivity of carbon is relatively high in the temperature range at which upper bainite forms, which is the reason why carbon partitioning from bainitic ferrite proceeds fast

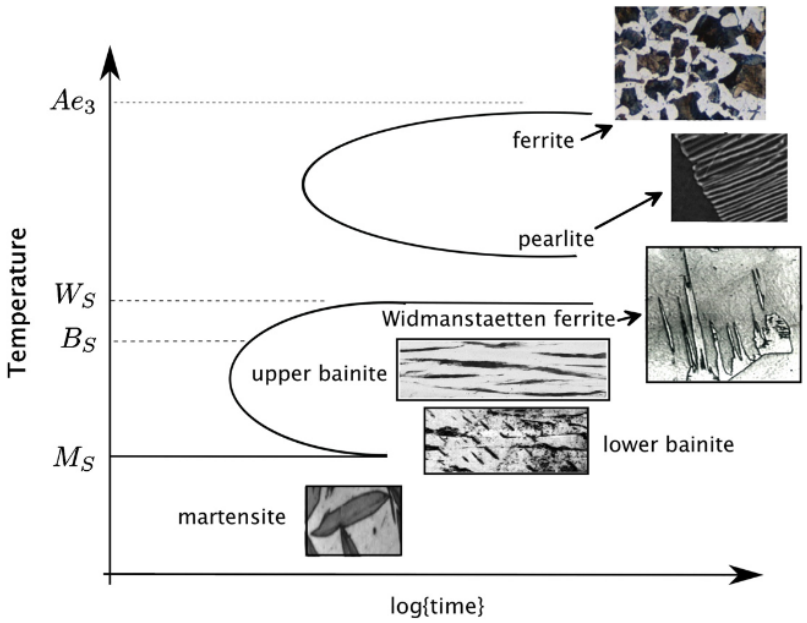

Figure 2: Schematic illustration of a TTT diagram of steel with separate C-curves [14].

and a relatively low carbon concentration is retained in solid solution within the bainitic ferrite. Thus, the remaining austenite becomes enriched in carbon, which may result in the precipitation of carbides from areas of austenite with high carbon concentrations in the second transformation stage. Usually, the austenite films in between bainitic ferrite plates are significantly enriched in carbon, which is the reason why carbide precipitation predominates in such areas. Depending on the steel's carbon content, these precipitates can appear as individual particles or as a continuous layer [14].

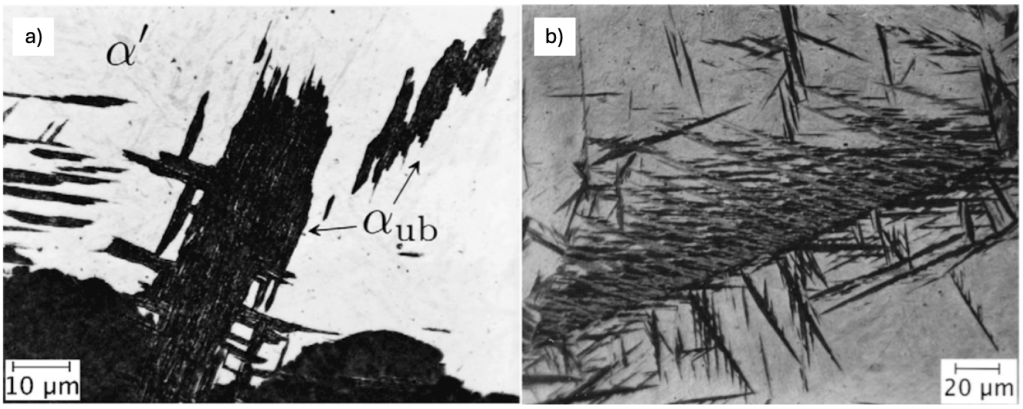

Figure 3: Optical microscopy image of a) upper bainite and b) lower bainite [14].

A transition from upper to lower bainite occurs at around 400 °C. The plate morphology of bainitic ferrite in lower bainite is depicted in Figure 3 b). One of the main microstructural differences of lower bainite, in comparison to upper bainite, is the presence of carbides inside bainitic ferrite. The transition from upper to lower bainite can be explained by the competing effect of carbon partitioning from the bainitic ferrite into the remaining austenite and carbide precipitation inside the

supersaturated bainitic ferrite. At elevated temperatures, carbon diffusion is relatively fast, which is the reason why the decarburization process of bainitic ferrite is too rapid to allow for carbide precipitation inside bainitic ferrite and hence upper bainite is formed. As the transformation temperature is reduced, the time required for excess carbon to partition from bainitic ferrite into the remaining austenite increases. When the driving force for carbide precipitation inside the bainitic ferrite overcomes the kinetics of carbon partitioning into the remaining austenite, a fraction of the carbon escapes the solid solution by precipitating as fine carbides inside the bainitic ferrite. This results in a smaller fraction of carbon to partition to the remaining austenite and hence fewer and finer carbides precipitate from the remaining austenite in lower bainite. This is the reason why lower bainite preserves higher toughness, even though it also has superior strength in comparison to upper bainite. It has been observed that the carbides present in lower bainite exhibit a specific orientation relationship with the bainitic ferrite from which they precipitate, which is similar to the one present when carbides precipitate during tempering of martensite [12, 14].

2.1.2 Phase constituents of bainite

Bainitic ferrite

Bainitic ferrite grows in the morphology of plates, which are assembled of smaller sub-units. Figure 4 shows an image, taken by transmission electron microscopy (TEM), with such a sub-unit structure. The sub-units first nucleate at prior austenite grain boundaries, followed by nucleation of further sub-units at the tip of already existing ones. This process is known as autocatalytic nucleation. Several sub-units together form a sheaf, which can be resolved by optical microscopy [14, 15].

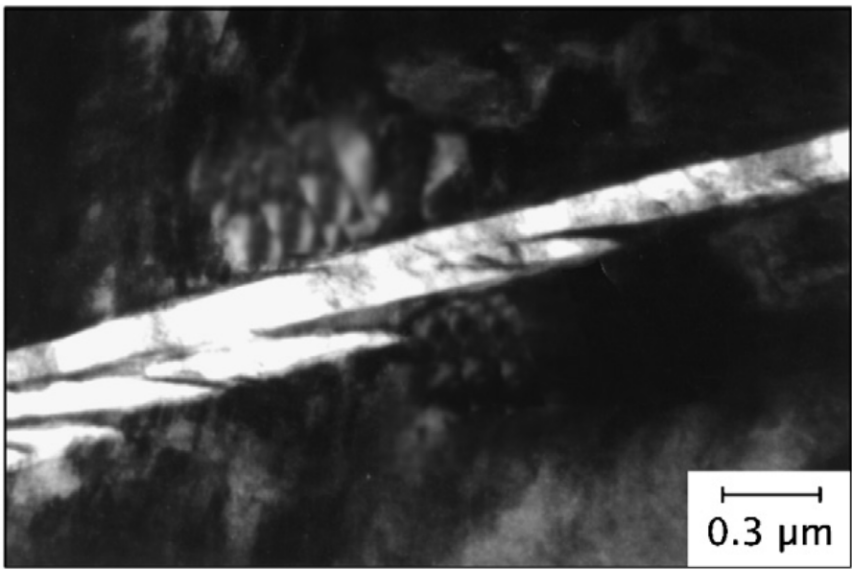

Figure 4: TEM image of a sub-unit structure [14].

Experimental observations have shown that the bainitic phase transformation results in the form-

ation of a surface relief, similar to the one present after martensite formation, which is known to progress via a displacive phase transformation mechanism [16, 17]. During displacive transformations, a change in crystal structure at low transformation temperatures is enabled by a coordinated motion of atoms, instead of reconstruction by diffusion. To minimize the strains resulting from such a transformation mechanism, the product phase grows as thin plates [11].

Furthermore, experimental observations have shown that bainitic ferrite is supersaturated in carbon after its formation [10, 18, 19]. Part of the increased carbon content in bainitic ferrite can be attributed to the trapping of carbon at defect sites, such as dislocations. However, there seems to be evidence that the elevated concentration of carbon kept in solid solution distorts the body-centered cubic unit cell. Thus, some researchers argue that bainitic ferrite could form taking a body-centered tetragonal (BCT) or body-centered orthorhombic structure [18]. The role of carbon atoms at the migrating interface is perhaps one of the most debated features of the bainitic phase transformation and will be explained in more detail in section 2.2.

Remaining austenite

In the case of carbide-free bainite, the remaining austenite becomes increasingly enriched in carbon as the phase transformation progresses. When the remaining austenite reaches a critical carbon concentration, the formation of bainitic ferrite stops prematurely, which is known as the incomplete transformation phenomenon since the phase transformation ceases before austenite reaches carbon concentration at paraequilibrium. The higher the transformation temperature, the lower the critical carbon concentration in the remaining austenite at which the phase transformation ceases. Thus, the formation of smaller fractions of bainitic ferrite can be expected at increasing transformation temperatures [9, 14]. Carbon enrichment stabilizes the remaining austenite, and hence lowers its martensite start temperature M_s [20], which can lead to the presence of retained austenite at room temperature [10].

The growth characteristics of bainitic ferrite lead to the formation of remaining austenite of different morphologies and sizes, such as blocky, film-like or slab-like remaining austenite [6, 10]. The size and shape of the remaining austenite unit, as well as the surrounding structure, affect its carbon enrichment. While film-like units, being located between two plates of bainitic ferrite, are relatively flat and small, blocky units are large areas between sheaves of bainitic ferrite. Therefore, film-like austenite becomes enriched in carbon much faster than blocky austenite [6]. This results in the development of carbon-poor and carbon-rich regions of remaining austenite, which can observed by the splitting of austenite peaks in XRD patterns [21, 22]. The morphologies of film-like and blocky units of remaining austenite are depicted in Figure 5, which has been taken using scanning electron microscopy (SEM).

Carbides

Carbides are an important part of the microstructure of bainite. The loss of carbon concentration

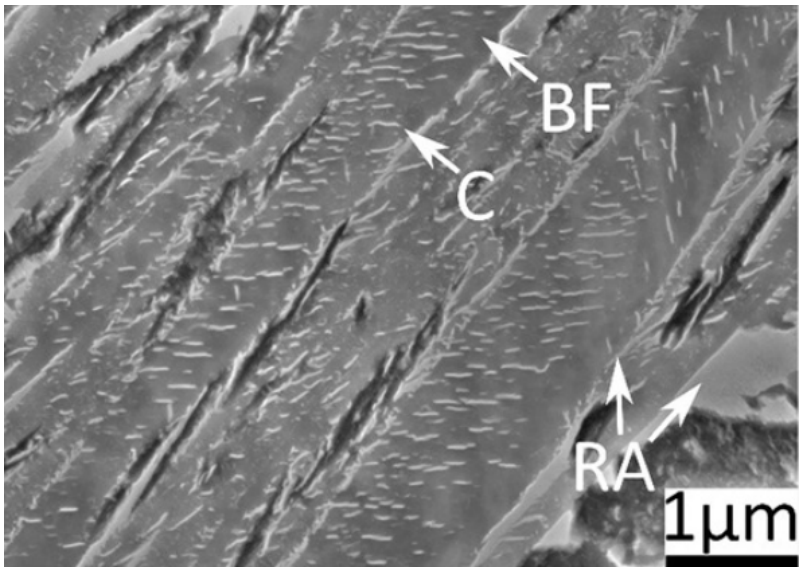

Figure 5: SEM image showing different morphologies of remaining austenite [6]. BF: bainitic ferrite, C: carbides, RA: remaining austenite.

in the remaining austenite due to carbide precipitation prevents the austenite from reaching the critical carbon concentration at which the phase transformation stops. This results in a decrease in austenite stability, and hence its decomposition to bainitic ferrite can continue [9, 15]. In carbide-free bainite, however, the precipitation of carbides is retarded by the addition of alloying elements, such as Si or Al. This causes all or most of the carbon to be kept in solid solution in the remaining austenite, which results in its stabilization as the phase transformation progresses. Carbide-free bainite can also be observed in steels with extremely low carbon concentrations below 0.02 wt. % carbon [9].

2.2 Phase transformation mechanism

2.2.1 Diffusionless theory

The diffusionless theory assumes that the bainitic phase transformation proceeds via a diffusionless-displacive transformation mechanism. Thereby, all carbon is trapped by the advancing interface, and hence bainitic ferrite inherits the carbon content of the parent austenite during its formation [6, 14]. Subsequently, carbon partitions from the supersaturated bainitic ferrite into the remaining austenite. As mentioned previously, bainitic ferrite sheaves are assembled of sub-units. These sub-units have an identical crystallographic orientation and may be separated by low misorientation boundaries, cementite or austenite [14]. The bainitic phase transformation starts with the nucleation of sub-units at prior austenite grain (PAG) boundaries. The sub-units have been observed to have a Kurdjumov-Sachs orientation relationship with the austenite after nucleation at the prior austenite grain boundary [12]. This orientation relationship can be described as follows [23]:

$$\{111\}_\gamma \| \{110\}_\alpha$$

$$\langle 1\bar{1}0\rangle_\gamma \| \langle 1\bar{1}1\rangle_\alpha$$

The macroscopic shape change left after the bainitic phase transformation can be described as an invariant-plane strain with a large shear component in addition to the volume strain caused by a displacive transformation mechanism of the crystal structure. The high strains resulting from this shape change are accommodated by plastic deformation of the adjacent remaining austenite. Thus, the dislocation density in the plastically deformed austenite is increased, which in turn increases the strength of the remaining austenite until it prevents the bainitic ferrite sub-unit from growing further. Therefore, the sub-units can only reach a limited size, which is substantially smaller than the size of a prior austenite grain [9, 14]. The growth of sheaves continues via autocatalytic nucleation, as schematically demonstrated in Figure 6. Hence, the diffusionless theory assumes the presence of two different types of nucleation sites for bainitic ferrite, namely the initial prior austenite grain boundaries and the newly created, incoherent interface boundaries between bainitic ferrite sub-unit tips and the austenite matrix [24].

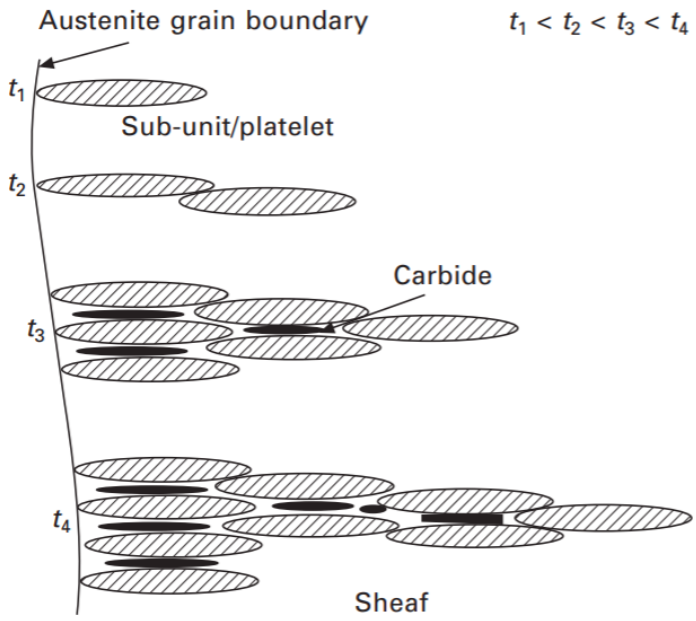

Figure 6: Schematic illustration of sheaf growth via autocatalytic nucleation [9].

Experimental observations using hot-stage photoemission electron microscopy have shown that bainitic ferrite sub-units exhibit a much faster lengthening rate than expected from a diffusion-controlled process. However, measurements of sheaf growth rates reveal deviations from the rapid growth rates of sub-units. The deviation in their lengthening rates is explained by a time interval between successive nucleation of sub-units [9, 14].

The decomposition from austenite to bainite occurs at temperatures at which the free energy of bainitic ferrite G^α is lower than the free energy of austenite G^γ at the same composition. The

temperature at which the free energies of both phases are equal defines T_0 and is demonstrated in Figure 7 [6, 14]. As the phase transformation progresses, carbon partitions from the bainitic ferrite and the new sub-units nucleate from carbon enriched austenite. The carbon enrichment of remaining austenite causes T_0 to decrease. At the point at which T_0 and the transformation temperature are equal, the diffusionless phase transformation becomes thermodynamically impossible and the transformation reaches stasis. This is known as the incomplete transformation phenomenon, since the phase transformation ceases before austenite reaches its carbon content at equilibrium, which is given by the Ae_3 line [9, 14].

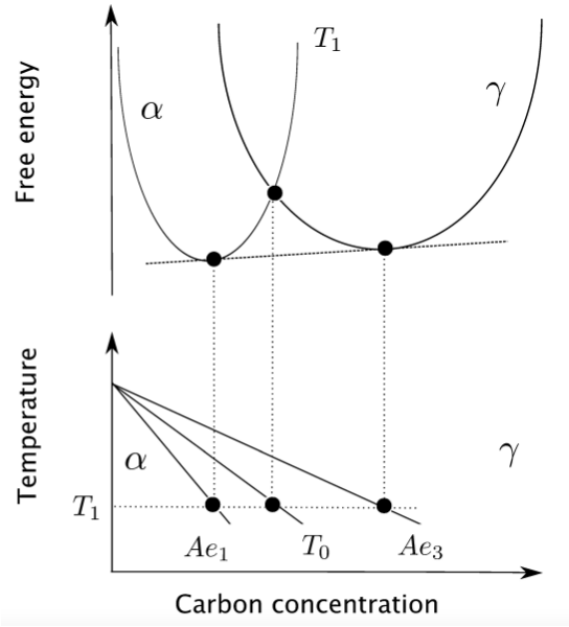

Figure 7: Schematic illustration of the origin of the T_0 construction [14].

Furthermore, the gain in free energy $\Delta G^{\gamma \to \alpha}$ from bainite formation also has to overcome an additional energy barrier G_{SB} associated with the energy required for the creation of interfaces and the shape change caused by the displacive phase transformation mechanism [6]. This criterion is defined by the following equations:

$$\Delta G^{\gamma \to \alpha} < -G_{SB} \tag{1}$$

$$\Delta G^{\gamma \to \alpha} = G^{\alpha} - G^{\gamma} \tag{2}$$

The additional energy barrier has an influence on the theoretical thermodynamic limit at which the bainitic transformation ceases. The corrected thermodynamic limit is known as T_0' [6, 14] and is defined by the temperature at which the gain in free energy from bainite formation equals the energy barrier ($\Delta G^{\gamma \to \alpha} = G_{SB}$) [15]. This energy barrier is often suggested to be about 400 Jmol^{-1} [10, 14, 15].

Another limit considered by the diffusionless-displacive theory is given by T_h, which can be defined as follows:

$$\Delta G_m < G_N \tag{3}$$

$$\Delta G_m = G_m^{\alpha} - G_m^{\gamma} \tag{4}$$

In order for the phase transformation to occur, the maximum driving force for bainitic ferrite nucleation ΔG_m has to be more negative than the universal nucleation function G_N. ΔG_m is the maximum reduction in free energy that can be achieved by bainitic ferrite nucleation with carbon redistribution without affecting the composition of the adjacent austenite and is defined by Equation 4. G_m^{α} and G_m^{γ} are the free energies of the respective phase at the condition of maximum free energy reduction. The temperature at which the two parameters in Equation 3 are equal is known as T_h and defines another limit of the bainitic phase transformation [15].

Only if the transformation temperature is lower than T_0' and T_h, bainitic ferrite continues to form [14, 15]. The carbon enrichment of the remaining austenite during the phase transformation causes T_h and T_0' to decrease. At the point at which T_h or T_0' becomes equal to the transformation temperature, the phase transformation will cease [15, 24].

2.2.2 Diffusional theory

According to the diffusional theory, the bainitic phase transformation is not fundamentally different from the decomposition of austenite to Widmanstätten ferrite. Thus, their phase transformation rate should be represented by a common C-curve for acicular ferrite in TTT diagrams [25, 26]. In contrast to the diffusionless theory, the diffusional theory assumes carbon to partition during the growth of bainitic ferrite. Therefore, the diffusion of carbon away from the migrating interface into the remaining austenite is defined as the rate-limiting process for the phase transformation [13, 27]. Originally, it was assumed that bainite forms under local equilibrium carbon concentration, which has led to the hypothesis that bainitic ferrite would form without supersaturation in carbon [13]. The presence of carbides in bainitic ferrite in lower bainite was explained by their precipitation from austenite at the bainitic ferrite-austenite interface and subsequent incorporation into the ferrite matrix due to the growth of the product phase [9].

Besides the phenomenon of supersaturation, the shape of the C-curves in TTT diagrams of different steel alloys is one of the main points of discussion between the two theories. As mentioned previously, many alloy systems exhibit two separate C-curves. However, for plain carbon steels only one C-curve can be observed [14]. Two distinct C-curves would imply the presence of two differ-

ent transformation mechanisms, with the upper one being representative for reconstructive phase transformations and the lower one for displacive phase transformations [16]. However, according to the diffusional theory, the existence of the bay between the two C-curves in TTT diagrams is related to the effect of certain alloying elements, known as the "solute drag effect". The solute drag effect arises from specific alloying elements that segregate to the interface between bainitic ferrite and austenite. Thereby, they exert a drag force on the migrating interface, which leads to a decrease in its mobility. A low driving force at higher transformation temperatures in combination with a high drag force causes the kinetics of bainite formation to slow down. At lower temperatures the driving force for transformation increases and overcomes the drag force so that the interface mobility increases again, which results in the appearance of a bay in TTT diagrams. The solute drag model has later been modified to the solute drag-like effect. However, the presence of a transformation bay is observed in many steel alloy systems and seems to be a rather general phenomenon instead of being attributable to the effect of specific alloying elements [9]. Nowadays, many supporters of the diffusional theory accept the formation of bainite to occur by a displacive phase transformation mechanism [6, 28]. However, whether the growth rate is determined by carbon diffusion or not remains a subject of debate.

The Zener-Hillert model is oftentimes used to describe the growth kinetics of bainitic ferrite based on the diffusional growth mechanism [9, 25, 29]. Hillert modified the original equation for diffusion-controlled edgewise growth of plates developed by Zener, to explain the growth of acicular ferrite [16]. He assumed the lengthening rate of bainitic ferrite plates to be controlled by long-range carbon diffusion away from the migrating bainitic ferrite-austenite interface, which creates a local carbon equilibrium [9, 13]. Figure 8 represents a schematic of the edgewise growth mechanism of bainitic ferrite. In the Zener-Hillert model, bainitic ferrite clusters are treated as a single entity, which grows continuously instead of growing by the successive nucleation of sub-units [9]. Thereby, the lengthening rate of bainitic ferrite plates can be calculated by:

$$\frac{v}{D} = \frac{(x^{\gamma\alpha} - x_0)^2}{(x_0 - x^{\alpha\gamma})} \cdot \frac{RT}{8\sigma V_m} \tag{5}$$

where v is the lengthening rate at temperature T, D is the diffusion coefficient of carbon in austenite, x_0 is the mole fraction of carbon in the steel alloy, $x^{\alpha\gamma}$ and $x^{\gamma\alpha}$ are the paraequilibrium mole fractions of carbon in the bainitic ferrite and austenite respectively, V_m is the molar volume of ferrite and σ is the interfacial energy per unit area [9].

However, experimental observations of Hillert and other researchers have shown that the actual growth rates of bainitic ferrite plates are slower than predicted by the Zener-Hillert model. While Kaufman et al. [30] assumed these deviations to be within the range of uncertainties arising from the calculation, Hillert [27] explained this deviation by the existence of a thermodynamic barrier to growth. From his growth rate analyses, Hillert concluded that the experimental growth rates

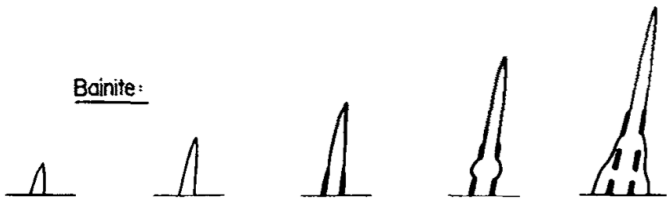

Figure 8: Schematic illustration of the edgewise growth mechanism of bainitic ferrite [27].

are continuous across the temperature range associated with Widmanstätten and bainitic ferrite formation [9, 26]. According to the Zener-Hillert model, the variation in the lengthening rate of acicular ferrite plates at a given temperature is approximately linearly related to the carbon content of the steel alloy. Thus, the extrapolation of the lengthening rate to zero allows to obtain the critical carbon content in austenite above which acicular ferrite cannot grow [26]. This critical carbon content defines the WB_s temperature, the Widmanstätten and bainite start temperature B_s [9, 16, 26]. Hillert [26] found that this critical carbon content deviates significantly from the Ae_3 line, which he used to explain the incomplete transformation phenomenon.

Regardless of the reason for the deviating growth rates, the measurement of even slower growth rates than predicted by calculations using the Zener-Hillert model have been interpreted as a confirmation of the presence of a diffusion-controlled growth mechanism being active during bainite formation. According to the supporters of the diffusional theory, the measured growth rates would be too low to allow for growth of bainitic ferrite with carbon supersaturation [9, 16, 27].

Nevertheless, the deviations of the calculations from the measured growth rates of acicular ferrite remain one of the main criticisms against the Zener-Hillert model [13]. Leach et al. [29] modified the Zener-Hillert model by the introduction of a 'barrier energy', which would increase as the carbon content in austenite increases. Additionally, their work suggested changes to the Zener-Hillert model, which would reduce the existent uncertainties in the calculations.

Benrabah et al. [28] worked on finding a physical explanation for the energy barrier introduced by Leach et al. [29]. They assumed a diffusional-displacive phase transformation mechanism, which proceeds via the movement of disconnections at the migrating interface boundary. According to their theory, the movement of these disconnections controls the rate of bainite formation. The presence of defects in the matrix can exert a force acting opposite to the direction of the migrating interface, due to interactions between the defects and the moving disconnections. Figure 9 shows a schematic representation of such interactions between disconnections and defects. The minimum force required to activate disconnection motion at the interface is called the back stress and originates from both dislocation-disconnection interactions, as well as from disconnections-solute interactions. When the driving force for transformation overcomes the energy barrier that arises from the back stress, the bainitic phase transformation proceeds [28].

Another point of criticism raised against the Zener-Hillert model is the fact that it cannot predict

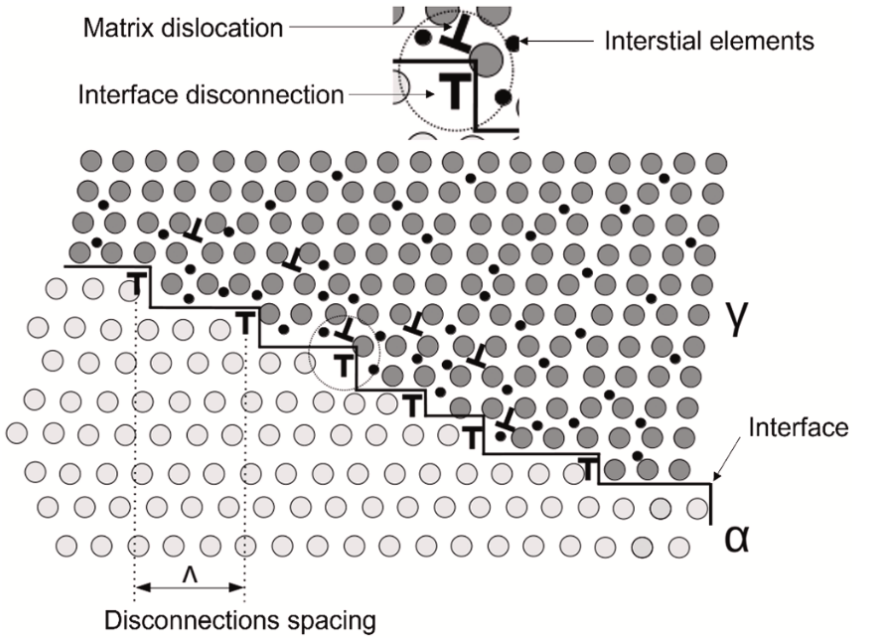

Figure 9: Schematic illustration of interactions between interface disconnections and defects present in the austenite matrix [28].

carbon supersaturation in bainitic ferrite. However, the use of modern characterization techniques, such as atom probe tomography (APT) or synchrotron X-ray diffraction (XRD), confirmed the presence of elevated carbon concentrations in bainitic ferrite, which increases as the transformation temperature decreases [13]. The original assumption of local equilibrium carbon concentration at the migrating interface might be realistic for phase transformations at elevated temperatures. However, as the transformation temperature is lowered carbon diffusivity is decreased, which makes the validity of the local equilibrium assumption for carbon less realistic. The diffusional phase transformation mechanism can be described by a two-step process. At first, carbon diffuses across the interface from bainitic ferrite to austenite, followed by subsequent carbon diffusion inside the remaining austenite away from the interface. The first process is negligible at higher transformation temperatures, since carbon diffusivity is relatively high. Therefore, the rate of the phase transformation is mainly governed by carbon diffusion in the remaining austenite. At lower transformation temperatures, however, carbon diffusivity decreases significantly, which results in the carbon transfer across the interface becoming the rate-limiting process and thus, leading to deviation from local equilibrium at the phase boundary. Based on these assumptions Benrabah et al. [13] suggested to modify the Zener-Hillert model, by relaxing the assumption of local equilibrium carbon concentration at the migrating interface. This allows for the existence of a difference in carbon activity that makes it possible to predict a carbon supersaturation in bainitic ferrite, which increases with decreasing transformation temperatures.

Benrabah et al. [13] used their modified model for calculating the carbon content of the product phase at transformation temperatures below the M_s temperature and found two solutions. One

solution predicts the growth of bainitic ferrite with partial supersaturation, while the other solution predicts the growth of a phase containing a carbon concentration approaching the nominal bulk content. The second solution is only present at transformation temperatures below the M_s temperature. The authors interpret the two solutions to imply the presence of two different transformation products, one being bainitic ferrite and the other one being martensite. This is consistent with experimental observations of phase transformations proceeding below the M_s temperature, where both bainite and martensite are present in the forming microstructure [10].

Based on the fundamentals explained in this chapter, the following part will explain the effect of the isothermal holding temperature, as well as the prior austenite grain boundaries, on the bainite formation kinetics. To ensure an in-depth understanding of the following chapter, the main findings of this chapter are summarized. Bainite consists of a fine plate-like structure of bainitic ferrite and carbides. Carbide precipitation is retarded by alloying with elements, such as Al and Si, which results in the formation of carbide-free bainite. In carbide-free bainite, less carbon escapes from solid solution of the remaining austenite by carbide precipitation and hence the remaining austenite becomes enriched in carbon. This results in a decreasing driving force for bainite formation and hence can cause the phase transformation to terminate prematurely. This is known as the incomplete transformation phenomenon. In the past, two theories about the mechanism of bainite formation have been developed: the diffusional and diffusionless theory. Today, both theories agree that bainitic ferrite forms by a displacive phase transformation mechanism. However, whether carbon partitions during or after the formation of bainitic ferrite is still a subject of discussion. Each theory has defined its own criterion for stasis of the transformation process, with the T_0 and T'_0 temperature being the criteria defined by the diffusionless theory and the WB_s temperature being the criterion defined by the diffusional theory. Experimental observations have shown that bainitic ferrite starts to form at the boundaries of prior austenite grains. Nowadays, many scientists agree on the fact that bainitic ferrite sheaves are assembled of individual sub-units, which nucleate at the tip of previously formed ones. A process known as autocatalysis.

2.3 Phase transformation kinetics of bainite

Bainite formation kinetics are often studied at constant transformation temperatures, which is known as an isothermal phase transformation. The phase transformation starts with an incubation time [6, 19], followed by a rapid increase in the transformation rate. After reaching its maximum, the transformation rate gradually slows down until it stops. Plotting the bainitic ferrite fraction formed as a function of time results in a sigmoidal curve [10, 14]. The following chapter is designated to explain the influence of different factors on the bainitic phase transformation kinetics. While the first section focuses on the effect of the isothermal holding temperature on the phase transformation kinetics and the carbon partitioning process, the second part is designated to discuss the influence of the microstructure present prior to the start of the bainitic phase transformation. The following

part aims to explain the findings on the effect of the prior austenite grain size on the phase transformation kinetics of bainite.

2.3.1 Influence of isothermal transformation temperature and prior microstructure on the phase transformation kinetics of bainite

One of the most important factors influencing the phase transformation kinetics of bainite is the isothermal transformation temperature. The lower C-curve in Figure 2 schematically represents the effect of the transformation temperature on the bainite formation kinetics. When decreasing the transformation temperature from B_s temperature towards the center of the C-curve, the bainitic phase transformation kinetics accelerate [4, 10, 31]. The enhanced transformation kinetics observed at decreasing transformation temperatures are a result of the higher driving force for bainitic ferrite nucleation at higher undercoolings [9, 32]. In the middle of the C-curve, the so-called nose, the phase transformation kinetics of bainite forming above M_s temperature are the fastest. Further decreasing the transformation temperature towards the lower end of the C-curve, the temperature range in which lower bainite forms, results in a deceleration of the phase transformation kinetics [19, 33].

Several studies have shown that the fraction of bainitic ferrite formed increases as the isothermal holding temperature approaches the M_s temperature [6, 10, 33]. At lower transformation temperatures, the critical carbon concentration at T_0' is increased, which results in a larger fraction of bainitic ferrite to be formed before the remaining austenite is sufficiently enriched in carbon to reach stasis [14].

Furthermore, the carbon partitioning process in bainite is affected by the isothermal transformation temperature [10, 19]. Rampelberg et al. [10] observed that bainitic ferrite in carbide-free bainite exhibits a higher carbon concentration at the end of the phase transformation when it has formed at lower transformation temperatures. This has been explained by the lower carbon diffusivity at decreasing transformation temperatures, which results in a higher carbon content remaining trapped in the bainitic ferrite at the end of the phase transformation. Furthermore, the researchers found that in carbide-free bainitic steels the carbon concentration in the remaining austenite at the end of the phase transformation increases, as the transformation temperature decreases. Even though carbon diffusivity is higher at increasing transformation temperatures, the amount of carbon to partition from bainitic ferrite is smaller due to the smaller fraction of bainitic ferrite forming in comparison to the larger fraction of remaining austenite being present at higher transformation temperatures. Thus, a lower carbon concentration in the remaining austenite at higher transformation temperatures can be observed [10, 22].

Lower transformation temperatures have been found to result in a higher dislocation density being present in the remaining austenite and bainitic ferrite [6, 19]. Foster et al. [19] explained the

increased dislocation density to result from the increased strength of the phases at lower transformation temperatures. Furthermore, the researchers reported that higher transformation temperatures can result in the annihilation of dislocations during the progress of the phase transformation. Lin et al. [6] investigated the influence of the Si concentration in steels on the bainitic phase transformation kinetics and reported decreasing phase transformation kinetics, as well as a smaller fraction of bainitic ferrite formed, as the Si concentration is increased. Part of the deceleration of the kinetics with increasing Si concentrations has been explained by the retardation of carbide precipitation due to alloying with Si, which causes the remaining austenite to become increasingly enriched in carbon as a result of carbon partitioning from bainitic ferrite. The increased carbon concentration in the remaining austenite causes a decrease in the driving force for bainite formation. Secondly, an increase in dislocation density in the remaining austenite with increasing Si concentrations has been observed. It was explained that the increase in dislocation density results from the increased strength of the phases due to solid solution hardening by Si. Solid solution hardening and the increased dislocation density in the remaining austenite pose additional resistance to the migration of the bainitic ferrite interface and hence can have a further decelerating effect on the kinetics of the bainitic phase transformation.

Rees and Bhadeshia [21] explained that a heterogeneous carbon distribution also effects the transformation kinetics of carbide-free bainite. As explained in section 2.1.2, the presence of different remaining austenite morphologies leads to the development of carbon-rich and carbon-poor regions. There is experimental evidence that the film-like remaining austenite present between bainitic ferrite plates can be significantly enriched in carbon. The researchers assume film-like remaining austenite to reach carbon concentrations higher than given by the T_0' criterion. Similar to the principle of carbide precipitation, the trapping of carbon inside austenite films that are isolated from the blocky austenite by bainitic ferrite plates removes carbon from the austenite matrix. Therefore, the remaining austenite that is present in blocks will be less enriched in carbon, which in turn leads to a larger maximum volume fraction of bainitic ferrite formed.

The previously existing microstructure can have a significant effect on the bainite formation kinetics. One of these influencing factors is the prior austenite grain size, which will be discussed in more detail in section 2.3.2. Furthermore, the presence of different phases prior to the formation of bainite can have an influence on its formation kinetics. Several studies have found that the formation of bainite at isothermal transformation temperatures below the steel's M_s temperature is accelerated because of the formation of athermal martensite prior to the onset of the bainitic phase transformation [31, 34, 35, 36]. Navarro-López et al. [31] investigated the effect of prior martensite on the bainitic phase transformation kinetics and plotted the bainitic ferrite fraction formed as a function of time for isothermal transformations with a similar fraction of bainite formed above and below the steel's M_s temperature, at 330 °C and 310 °C respectively. Instead of finding a sigmoidal curve, which is typical for bainite transformation kinetics above the M_s temperature, at isothermal transformation temperatures below the M_s temperature the maximum transform-

ation rate was already observed at the start of the phase transformation, as it is demonstrated in Figure 10. The transformation rate was 2 to 3 orders of magnitude higher in the presence of small fractions of prior martensite in comparison to the transformation rate of treatments above M_s temperature. However, this accelerating effect has only been observed at the beginning of the phase transformation and the initial maximum nucleation rate is followed by a gradual decrease in the transformation kinetics. Therefore, the accelerating effect has been attributed to the presence of a higher number of potential nucleation sites resulting from the formation of newly formed austenite-martensite interfaces. The researchers emphasized that instead of the martensite volume fraction formed, it is the area of austenite-martensite interfaces that increases the number of potential nucleation sites for bainite nucleation.

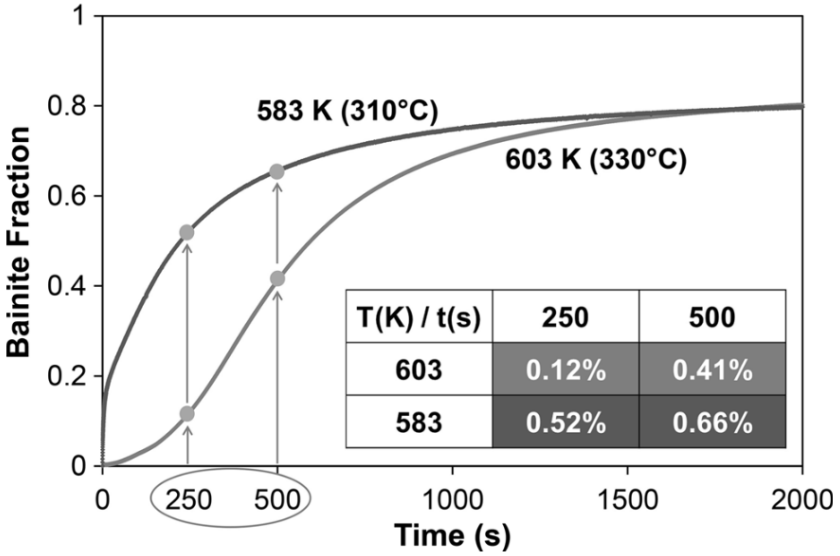

Figure 10: Bainite fraction as a function of time at 330 °C (above M_s temperature) and 310 °C (below M_s temperature) to demonstrate the initial accelerating effect of prior martensite [31].

Furthermore, Ravi et al. [37] found that the presence of less than 5 % ferrite, formed during an intermediate annealing treatment prior to bainite formation, accelerates the transformation kinetics. Similar to the formation of martensite, the formation of ferrite results in an increase in potential nucleation sites, due to the presence of newly created ferrite-austenite interfaces. However, as the ferrite fraction formed prior to the onset of bainite formation increases to higher fractions, the carbon concentration in the austenite available for bainite formation increases as well. This stabilizes the austenite and hence increases the activation energy for subsequent bainitic ferrite nucleation. Therefore, only small fractions of ferrite formed prior to bainite formation have an accelerating effect on its phase transformation kinetics. Furthermore, the researchers observed that preceding isothermal treatments without any detectable ferrite formation can lead to the acceleration of subsequent bainite transformations. Their investigations revealed the formation of carbon-rich and carbon-poor regions as a result of carbon segregation to austenite grain boundaries. Regions of low carbon concentration can assist the nucleation of bainitic ferrite since the driving force for bainite formation increases as the carbon concentration in the austenite matrix decreases.

Thus, carbon segregation resulting from preceding heat treatments also plays an important role in the kinetics of bainite formation.

2.3.2 Influence of prior austenite grain size on the phase transformation kinetics of bainite

In steels, many product phases start to form at the grain boundaries of the parent austenite, which is the reason why their phase transformation kinetics are often influenced by the austenite's morphology and grain size. Usually, the refinement of prior austenite grains results in an acceleration of the phase transformation kinetics in diffusional transformations, such as pearlite formation. In contrast, displacive phase transformations, like the formation of martensite, do not show a strong dependence on the grain size of the parent phase [38]. In the case of bainite, experimental results concerning the influence of the prior austenite grain size on the transformation kinetics are contradictory. Several studies have shown that the refinement of prior austenite grains results in an acceleration of the bainite formation kinetics [39, 40]. Barford and Owen [39] based their explanation for the accelerating effect of smaller PAGs on the fact that the bainitic phase transformation starts from the grain boundaries. Thus, decreasing the size of the prior austenite grains results in a larger grain boundary area and hence in a higher number of potential nucleation sites for bainitic ferrite. However, the opposite behavior has been reported as well. Hasan et al. [38] found accelerated transformation kinetics, as well as an increasing fraction of bainitic ferrite formed when the steel's microstructure consisted of larger prior austenite grains. The researchers found that the nucleation rate at the beginning of the phase transformation is higher for smaller prior austenite grain sizes, which is related to the higher number of potential nucleation sites as a result of the larger grain boundary area available at smaller PAG sizes. However, the maximum nucleation rate reached during the process of the phase transformation increases and the time needed to reach this maximum nucleation rate decreases consistently with an increase in the PAG size. This has been explained by the fact that sheaves cannot grow beyond prior austenite grain boundaries. Thus, smaller prior austenite grains restrict the growth of sheaves, which results in the deceleration of the phase transformation process, if the overall transformation kinetics are dominated by autocatalysis. In contrast to the previously mentioned studies, Davenport et al. [41] reported that the bainitic phase transformation kinetics are not affected by the size of the prior austenite grains.

Matsuzaki and Bhadeshia [42] found that the effect of the PAG size on the bainite formation kinetics depends on the steel composition. The investigated steels showed an opposite relationship between the PAG size and the kinetics of bainite formation. While steel A (Fe-0.12C-2.03Si-2.96Mn) showed an acceleration of the bainite formation kinetics with an increase in PAG size, steel B (Fe-0.96C-0.21Si-0.38Mn-1,26Cr) showed an acceleration with a decrease in PAG size. Their microstructure observations at the early stages of the phase transformation, presented in Figure 11, revealed that steel A exhibited relatively large bainitic ferrite sheaves. This implies that the rate

of autocatalytic nucleation is relatively high in comparison with the rate of sub-unit nucleation at the PAG boundaries. In contrast, the microstructure of steel B showed that the majority of bainitic ferrite sub-units have formed at the PAG boundaries. Therefore, they concluded that if the overall transformation kinetics are limited by a slow sheaf growth rate, a smaller PAG size leads to an acceleration of the transformation kinetics. In contrast, if the growth rate of sheaves is relatively high, prior austenite grain refinement reduces the total volume transformed per nucleus formed at the prior austenite grain boundaries and hence retards the bainite formation kinetics.

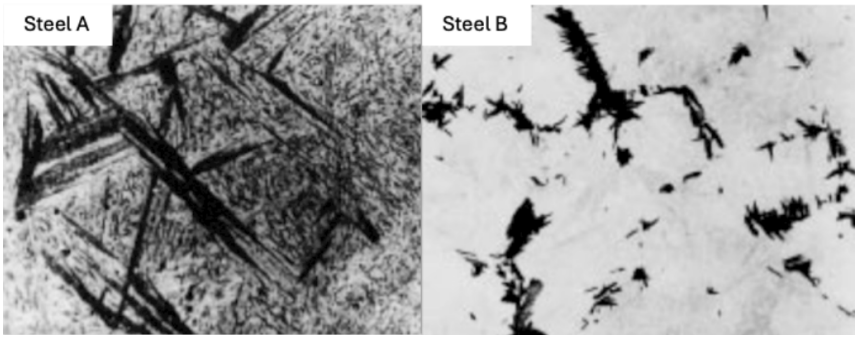

Figure 11: Microscopy images of the sheaf morphology formed at the early stages of the phase transformation [42].

Ravi et al. [15] developed a physically based model considering the difference in Q_{GB}, the activation energy for grain boundary nucleation, and Q_A, the activation for autocatalytic nucleation, to enable the prediction of the kinetics of bainite formation. Whether sub-unit nucleation occurs preferentially at prior austenite grain boundaries or at the tip of previously existing sub-units depends on the activation energy for nucleation at the specific nucleation site. The difference in activation energy for grain boundary and autocatalytic nucleation is denoted as ΔQ and is defined as follows:

$$\Delta Q = Q_{GB} - Q_A \tag{6}$$

Calculations of Ravi et al. [15] showed that the activation energy at both types of nucleation sites decreases linearly with increasing undercooling, which is the reason why the researchers assume bainite nucleation to occur by thermally activated migration of partial dislocations creating a stacking fault. While grain boundary nucleation occurs at γ/γ interfaces and results in the creation of α/γ interfaces, autocatalytic nucleation occurs at α/γ interfaces and results in the creation of new α/γ, as well as α/α interfaces. The researchers explained that the activation energy for autocatalytic nucleation may be lower in comparison to the activation energy for grain boundary nucleation, due to the formation of coherent α/α interfaces, which are energetically more favorable than α/γ interfaces. Additionally, their calculations showed that the activation energy for nucleation at the different types of nucleation sites also depends on the chemical composition of the steel and hence is influenced by the concentration of carbon and other alloying elements.

Dos Santos Avila et al. [24] modified the model developed by Ravi et al. [15] to account for the effect of the prior austenite grain size and the bainitic ferrite sub-unit size on the bainite formation kinetics. From simulations with their developed model, the researchers concluded that the larger ΔQ, the more autocatalytic nucleation is preferred over grain boundary nucleation and thus a larger PAG size results in the acceleration of the bainite formation kinetics. Furthermore, they observed that ΔQ increases with low carbon concentrations, as well as low undercoolings. Thus, the effect of PAG size on the bainite formation kinetics depends on the steel's composition and the transformation temperature. ΔQ can be affected by the segregation of alloying elements to interfaces and the build-up of carbon at the tip of bainitic ferrite sub-units as a result of carbon partitioning, which can cause the driving force for bainitic ferrite nucleation at a specific nucleation site to decrease [24, 32]. Besides ΔQ, the sub-unit volume has an important influence on the bainite formation kinetics. Larger sub-units accelerate the transformation process since the volume of austenite that is transformed per nucleation event is larger. Using the modified model, dos Santos Avila et al. [24] showed that a variation in sub-unit volume can reverse the previously observed effect of PAG size on the bainite formation kinetics. Among other parameters, the size of sub-units is dependent on the prior austenite grain size. Eres-Castellanos et al. [43] reported that the sub-unit thickness is significantly affected by the yield strength of austenite, which is the reason why it could be expected that a refinement of the PAG size results in a smaller sub-unit size [24]. However, their correlation is not straightforward and the opposite behavior has been reported as well [44]. Thus, understanding the factors influencing the bainitic ferrite sub-unit size, as well as the value of ΔQ, is of high importance for explaining and simulating the effect of prior austenite grain size on the bainite formation kinetics.

In summary, it can be said that the transformation temperature, as well as the previously existing microstructure, have a significant effect on the bainite formation kinetics. In carbide-free bainite, a decreasing isothermal transformation temperature results in a higher fraction of bainitic ferrite formed. The dependence of the bainitic phase transformation kinetics on the transformation temperature can be represented by a C-curve in a TTT-diagram. Therefore, in the higher transformation temperature range a decrease in isothermal holding temperature results in an increase in the bainite transformation kinetics until the nose of the curve is reached. Below the nose, further reducing the isothermal holding temperature leads to decreasing phase transformation kinetics of the bainite. The lower end of the C-curve is often superimposed by the formation of prior martensite, which has an accelerating effect on the phase transformation kinetics of bainite. Furthermore, the isothermal transformation temperature affects the process of carbon partitioning. The higher the transformation temperature, the higher the carbon diffusivity, which results in faster partitioning of carbon into the remaining austenite. The contradictory results on the influence of prior austenite grain size on the bainite formation kinetics can be explained by the presence of two types of nucleation sites, namely the PAG boundaries and the tip of previously existing sub-units. The difference in activation energy for bainitic ferrite nucleation at the two types of nucleation sites is

denoted as ΔQ and determines the preferred site for bainitic ferrite sub-unit nucleation. In the case of a high ΔQ, autocatalytic nucleation is preferred over grain boundary nucleation. Thus, the bainite formation kinetics are accelerated by prior austenite grain coarsening, since bainitic ferrite sheaves can grow larger. A low value of ΔQ implies preferred grain boundary nucleation. In that case, the bainite formation kinetics are accelerated by prior austenite grain refinement since it increases the grain boundary area at which sub-units can nucleate. Besides ΔQ, the size of bainitic ferrite sub-units affects the bainite formation kinetics.

2.4 Conclusion and research gaps

The objective of this literature review was to gain a fundamental understanding of the bainitic phase transformation mechanism, as well as the effects of the isothermal transformation temperature and microstructural features, such as the prior austenite grain size, on the bainite formation kinetics. This chapter is designated to present the main findings, as well as the research gaps that have been identified in the process of the review. The main findings on the phase transformation mechanism and microstructure of bainite are:

1. Bainite consists of a fine plate-like structure of bainitic ferrite and carbides. Alloying bainitic steels with Si or Al retards carbide precipitation, which may result in the formation of carbide-free bainite. Instead of carbide precipitation, the remaining austenite becomes enriched in carbon, which decreases the driving force for bainite formation and causes the phase transformation to terminate prematurely. This is known as the incomplete transformation phenomenon. Those areas of austenite that are sufficiently enriched in carbon are retained after final cooling to room temperature.

2. In the past, two theories about the mechanism of bainite formation have been developed: the diffusional and diffusionless theory. Nowadays, both theories agree on the fact that bainite forms by a displacive phase transformation mechanism. However, whether carbon partitions during or after bainite formation is still a subject of discussion. Each theory has defined its own criterion for stasis of the transformation process, with the T_0 and T'_0 temperature being the criteria defined by the diffusionless theory and the WB_s temperature being the criterion defined by the diffusional theory.

3. Experimental evidence confirmed that bainitic ferrite is supersaturated in carbon after its formation. Some researchers argue that the supersaturation leads to the distortion of the body-centered cubic unit cell, so that bainitic ferrite takes a body-centered tetragonal or body-centered orthorhombic structure.

4. Bainitic ferrite starts to form at the boundaries of prior austenite grains. Sheaves grow by the subsequent nucleation of bainitic ferrite sub-units at the tip of previously formed ones. A process known as autocatalysis.

The main findings on the effect of the isothermal transformation temperature and prior microstructure on the bainite formation kinetics are:

1. Investigations have shown that the isothermal transformation temperature influences the bainite formation kinetics, which can be described by the shape of a C-curve in a TTT-diagram.

2. The isothermal transformation temperature affects the process of carbon partitioning. The higher the transformation temperature, the higher the carbon diffusivity, which results in faster partitioning of carbon from bainitic ferrite into the remaining austenite.

3. The formation of small fractions of martensite or ferrite has been observed to accelerate the bainite formation kinetics. This has been explained by an increase in the number of potential nucleation sites.

4. Additionally, the thermal history seems to play an important role in the kinetics of bainite formation. It has been observed that the formation of carbon-rich and carbon-poor regions during a heat treatment prior to bainite formation can result in the acceleration of the kinetics. This may be explained by an increased driving force for bainite formation in carbon-poor austenite areas.

The main findings on the effect of prior austenite grain size on the bainite formation kinetics are:

1. Contradictory results on the influence of prior austenite grain refinement on the bainite formation kinetics have been found in the literature. Many studies explain their observations based on the presence of two types of nucleation sites, namely the prior austenite grain boundaries and the tip of previously existing sub-units.

2. The difference in activation energy for nucleation at the two types of nucleation sites is denoted as ΔQ and determines the preferred site for bainitic ferrite sub-unit nucleation. In the case of a high ΔQ, autocatalytic nucleation is preferred and hence the bainite formation kinetics are accelerated by prior austenite grain coarsening since bainitic ferrite sheaves can grow larger. A low value of ΔQ implies preferred grain boundary nucleation. In that case, the bainite formation kinetics are accelerated by prior austenite grain refinement since it increases the grain boundary area at which sub-units can nucleate. Studies have shown that the value of ΔQ can be affected by the transformation temperature and the carbon concentration in austenite.

3. Simulations have shown that the effect of the prior austenite grain size on the bainite formation kinetics can be reversed by changing the size of the bainitic ferrite sub-units. However, it has not been fully understood yet, how the sub-unit size is affected by different factors.

Based on the work summarized in the literature review, the following research gaps were identified:

1. Extensive research has been conducted to gain a profound understanding of the transformation mechanism of bainite. However, no consensus yet exists on whether bainite formation occurs by a diffusional or diffusionless transformation mechanism. While the majority of researchers agree on the fact that the bainitic phase transformation proceeds by a displacive phase transformation mechanism, whether carbon partitioning occurs during or after bainite formation is still a subject of debate.

2. Therefore, it has not yet been possible to determine the actual criterion for the incomplete transformation phenomenon during bainite formation. Several studies compare their findings on transformation stasis to the T_0 and T_0' temperature defined by the diffusionless theory and / or to the WB_s temperature defined by the diffusional theory. However, the supporters of the two theories have not found an overall agreement on these criteria yet.

3. There is experimental evidence that bainitic ferrite is supersaturated in carbon after its formation. However, it is still uncertain whether this supersaturation leads to the distortion of the body-centered cubic unit cell to a body-centered tetragonal or a body-centered orthorhombic structure.

4. The contradictory results regarding the effect of prior austenite grain refinement on bainite formation kinetics cannot be fully explained yet. Researchers have found that one of the factors influencing the effect of the prior austenite grain size on the bainite formation kinetics is the difference in activation energy for autocatalytic and grain boundary nucleation, which in turn seems to be influenced by the transformation temperature and the steel composition. Furthermore, the observed effect of the prior austenite grain size is dependent on the size of bainitic ferrite sub-units.

5. To understand the correlation between the prior austenite grain size and the phase transformation kinetics of bainite, a profound understanding of the underlying mechanisms influencing the bainitic ferrite sub-unit size and the difference in activation energy for autocatalytic and grain boundary nucleation is required.

2.5 Research approach

The contradictory results reported regarding the effect of the prior austenite grain size on the bainite formation kinetics are often explained based on the presence of two different types of nucleation sites. Their difference in activation energy for nucleation, ΔQ, determines the preferred site for bainitic ferrite sub-unit nucleation. Researchers have shown that the steel composition, as well as a change in the bainitic ferrite sub-unit size, can reverse the effect of the prior austenite grain size on the kinetics of bainite formation. Many studies performed their experiments with varying

prior austenite grain sizes at a fixed transformation temperature. However, the transformation temperature is known to affect the activation energy for nucleation at both types of nucleation sites. Furthermore, it can affect the steel composition locally due to the effect of temperature on processes, such as carbon partitioning. Therefore, experiments with varying prior austenite grain sizes at different transformation temperatures would support understanding the effect of the prior austenite grain size on the phase transformation kinetics of bainite.

The high brilliance of synchrotron XRD makes it possible to conduct in-situ experiments to investigate phase transformations [45, 46]. Its application enables to investigate the evolution of the phase fractions of bainitic ferrite and austenite, the redistribution of carbon and the development of a heterogeneous microstructure, the evolution of the dislocation density and potential recovery and in some cases the formation of carbides. Therefore, in-situ synchrotron XRD is a suitable characterization technique to investigate the effect of the prior austenite grain size on the phase transformation kinetics of bainite.

This leads to the definition of the following research approach, which is related to research gaps 4 and 5 defined in section 2.4. The research approach of the master thesis is divided into three parts. The first part focuses on analyzing in-situ synchrotron XRD experiments performed during bainite formation in a low-carbon high-silicon steel. The experiments were divided into two experiment groups based on the prior austenite grain size, with one group consisting of specimens with finer prior austenite grains and one group consisting of specimens with coarser prior austenite grains. One specimen per experiment group was transformed to bainite at three different isothermal transformation temperatures (440 °C, 410 °C, and 380 °C), resulting in a total of six different combinations of prior austenite grain sizes and isothermal transformation temperatures. The analysis of the in-situ synchrotron XRD data allows to obtain information on the evolution of the phase fractions, lattice parameters and microstrains during the phase transformation. Furthermore, microstructure investigations using optical microscopy and scanning electron microscopy were performed on the specimens transformed during the in-situ synchrotron XRD experiments. Secondly, microstructure investigations on interrupted quenching experiments were conducted. Finally, simulations to determine the activation energy for grain boundary and autocatalytic nucleation, ΔQ, were performed using the model developed by dos Santos Avila [24]. The objective of the defined research approach is to understand the effect of the prior austenite grain size and the isothermal transformation temperature on the following aspects:

1. The microstructure formed during bainite formation.
2. The phase transformation kinetics.
3. The difference in activation energy for grain boundary and autocatalytic nucleation ΔQ.
4. The carbon partitioning process and its influence on ΔQ.

3 Material and experimental procedure

3.1 Material and pretreatment

The composition of the low-carbon high-silicon steel investigated in the experiments is given in Table 1. Alloying the steel with carbon and manganese decreases the driving force for ferrite formation during initial quenching from the austenitization temperature to the isothermal transformation temperature [2, 31] and decelerates the phase transformation kinetics of bainite. The fraction of carbides in the final microstructure of bainite increases with carbon concentration [14]. Furthermore, manganese is known to segregate to prior austenite grain boundaries, which results in further deceleration of the bainite formation kinetics [2].

Element	C	Mn	Si	Fe
Concentration in wt.%	0.24	2.3	1.5	bal.

Table 1: Chemical composition of the bainitic steel investigated.

Alloying with silicon retards or even suppresses carbide precipitation entirely, which results in the formation of carbide-free bainite. Therefore, most or all of the carbon that partitions into the remaining austenite is kept in solid solution, leading to the stabilization of the remaining austenite and hence to the deceleration of the phase transformation kinetics of bainite [6]. The relevant transformation temperatures of the steel investigated are given in Table 2.

	A_{c1}	A_{c3}	B_s	M_s
Temperature	745 °C	860 °C	558 °C	359 °C

Table 2: Transformation temperatures of the bainitic steel investigated.

The temperatures at which the steel's transformation to austenite starts and finishes during heating at a rate of 20 °C/s, A_{c1} and A_{c3}, and the martensite start temperature, M_s, were determined using dilatometry. The bainite start temperature, B_s, was calculated using the equation 7, which determines B_s with an accuracy of ± 25 °C [14].

$$B_s = 830 - 270x_c - 90x_{Mn} - 70x_{Cr} - 83x_{Mo} - 37x_{Ni} \tag{7}$$

The specimens used for the in-situ synchrotron XRD and the interrupted quenching experiments were manufactured from cold rolled steel sheets. The sheets were cut into plate-shaped 10 x 5 x 1 mm^3 dilatometry specimens with the long direction of the specimen being parallel to the rolling direction of the sheet. To ensure a homogeneous distribution of elements across the microstructure of all specimens, homogenization was performed at 1250 °C for 48 hours in a sealed quarz tube inside a furnace with a protective atmosphere, to avoid oxidation or decarburization. After the homogenization process, the prior austenite grains are expected to be relatively large. Therefore,

thermal cycling, as illustrated in Figure 12, was used to reduce the prior austenite grain size of the specimens at the start of the experiments. During the thermal cycling heat treatment, the steel was rapidly heated from room temperature to 900 °C, which is above its A_{c3} temperature, at a rate of 20 °C/s. After being held at 900 °C for 120 seconds, the specimens were quenched to 30 °C at a rate of 50 °C/s. The procedure was repeated four times. Such a rapid austenitization process starting from a fine initial microstructure, such as martensite, leads to the refinement of the prior austenite grain structure [47]. The resulting microstructure makes it possible to adjust the PAG size during the initial austenitization step of the following experiments by varying the maximum austenitization temperature

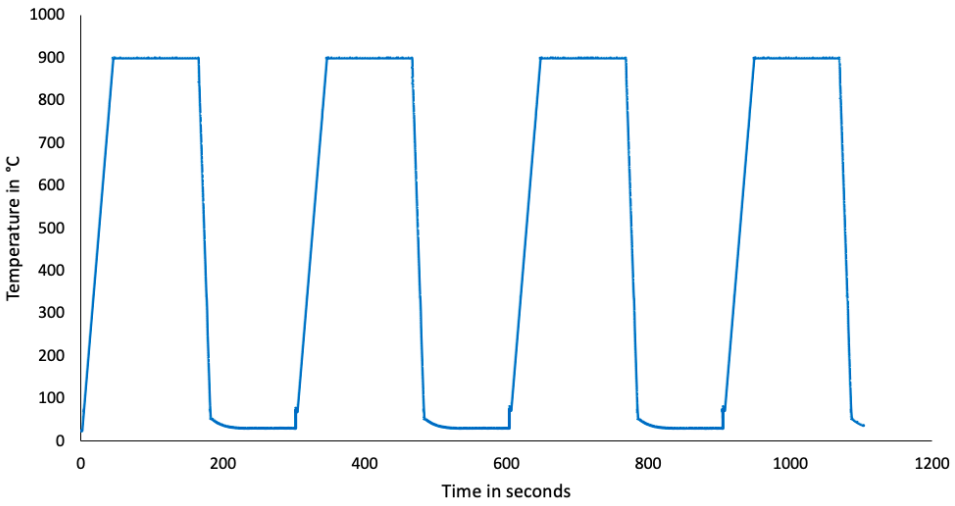

Figure 12: Thermal cycling heat treatment for PAG size reduction after homogenization.

3.2 In-situ synchrotron XRD at DESY

3.2.1 Experimental setup and heat treatment

In-situ synchrotron XRD experiments were performed at the P07 High Energy Materials Science Beamline at PETRA III synchrotron facility, Deutsches Elektronen-Synchrotron (DESY) in Hamburg, Germany. A Bähr DIL 805 A/D dilatometer, integrated in the beamline, was used for the heat treatment of the specimens. A thermocouple was spot-welded in the middle of the specimen to enable temperature measurement and control. The specimens were irradiated by a monochromatic beam of energy $E = 103.2$ keV (corresponding to a wavelength of $\lambda = 0.11994$ Å) and beam size of 1 x 1 mm^2. The PerkinElmer XRD 1621 flat panel detector was placed approximately 1651 mm behind the specimen to collect two-dimensional diffraction patterns during the experiments. A schematic of the experimental setup is presented in Figure 13. A measurement of a National Institute of Standards and Technology (NIST) standard LaB_6 powder (SRM 660b) was used to calibrate the experimental setup, to obtain the specimen-to-detector distance, the position of the center of the beam and the tilt angle of the detector.

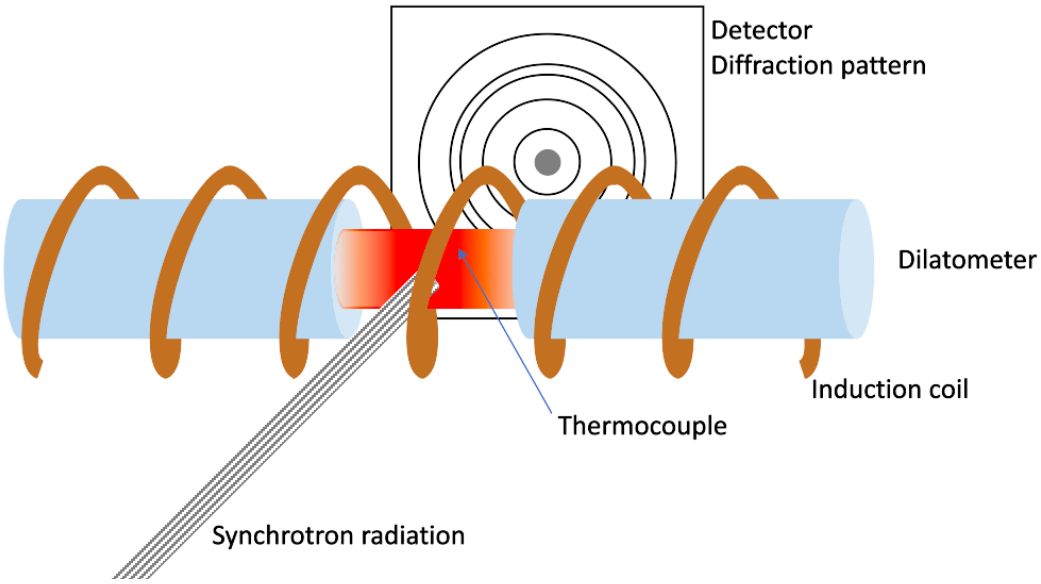

Figure 13: Schematic representation of the experimental setup at DESY PETRA III P07 beamline.

All specimens were homogenized and thermally cycled as explained in section 3.1 before performing the in-situ synchrotron XRD experiments. The experiments were divided into two groups, with one group consisting of specimens with finer prior austenite grains and one with coarser prior austenite grains. The prior austenite grain size was adjusted by varying the maximum austenitization temperature for the coarser and finer grain sizes. Figure 14 represents the heat treatment of specimens with finer prior austenite grains. The heat treatment started with heating the specimens at a rate of 20 °C/s to 900 °C, where they were held for 120 seconds. Austenitization was followed by quenching the specimens at a rate of 50 °C/s to the isothermal holding temperature, where they were held for 600 seconds for bainite formation. Isothermal phase transformations were performed at 440 °C, 410 °C and 380 °C. Finally, the specimens were quenched to room temperature. Helium gas was used for all quenching processes in the experiments.

Figure 15 shows the heat treatment of specimens with coarser prior austenite grains. The heat treatment of these specimens was similar to the heat treatment applied to specimens with finer prior austenite grains, with the only difference in the process step of austenitization. To obtain a larger PAG size, the specimens were initially heated to 1100 °C, where they were held for 120 seconds. Subsequently, the specimens were quenched at a rate of 20 °C/s to 900 °C, where they were held for another 120 seconds until they were quenched to their isothermal holding temperatures. This procedure eliminates sub-microscopic differences arising from varying austenitization temperatures and thus makes it possible to study the effect of the prior austenite grain size, while excluding the effect of the austenitization temperature on the phase transformation kinetics [39, 42]. Post-processing of the data revealed that the cooling rates during the final quenching to room temperature were different for some of the experiments. While experiments with isothermal transformation temperatures at 440 °C and 380 °C experienced a cooling rate of 9 °C/s, the experiments

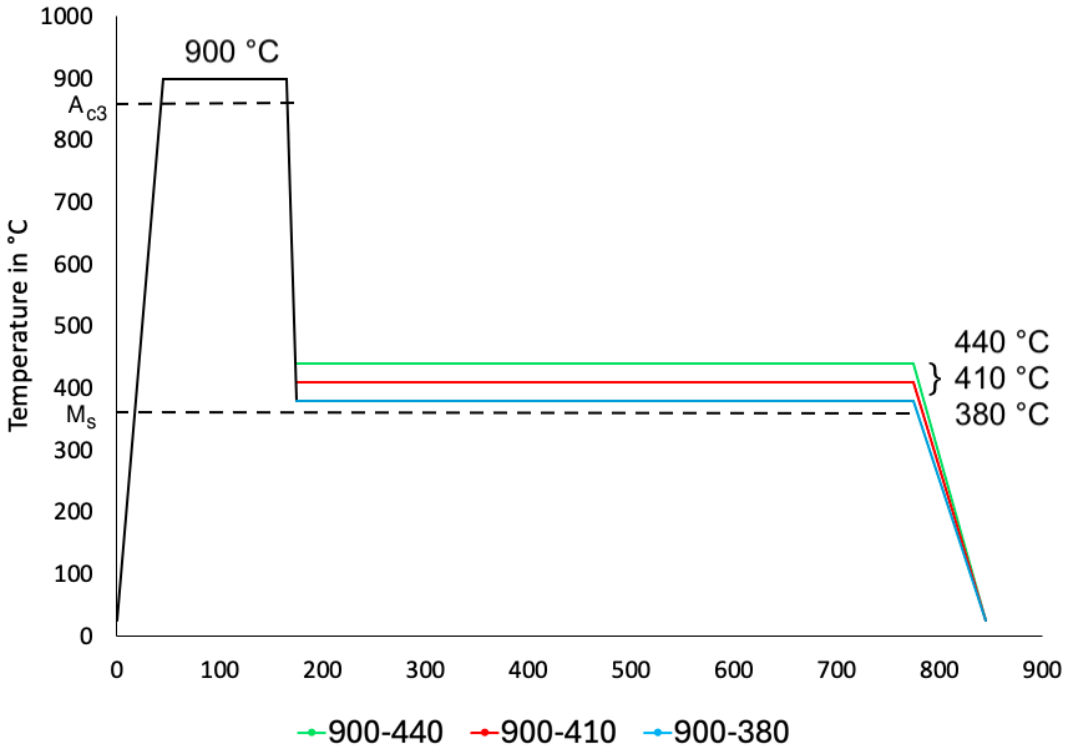

Figure 14: Heat treatments to obtain fine PAGs in experiments performed at DESY.

with transformation temperatures at 410 °C experienced a cooling rate of 35 °C/s. The different cooling rates may have minor effects on the fraction of fresh martensite formed during the final quenching process.

Two different data acquisition rates were used to monitor the phase transformation processes, namely the "fast mode" and the "slow mode", which record XRD patterns every 0.1 and every 5 seconds, respectively. The slow mode records XRD patterns with the best resolution, but at a relatively slow rate. Therefore, rapid proceeding changes during processes, such as quenching or the beginning of the bainitic phase transformation, were recorded with the fast mode. To reduce the total amount of data recorded during the experiments, the slow mode was used in between. In the experiments the first 150 seconds, which include heating to the austenitization temperature and a part of the austenitization process, were recorded using the slow mode. The following 150 seconds of the experiment were recorded using the fast mode, which include the remaining time of the austenitization process, cooling to the isothermal holding temperature and the first 130 seconds of holding at the isothermal transformation temperature. The remaining part of the experiment was monitored using the slow mode again, which includes the rest of the holding time at the isothermal transformation temperature, as well as the final quenching to room temperature. The seconds given for the respective intervals are approximate numbers, since the time needed for heating or cooling to the austenitization or isothermal holding temperatures may differ.

To calculate the phase transformation time, a start time needed to be defined. Setting the start time of the isothermal holding is not straightforward, since the temperature does not always

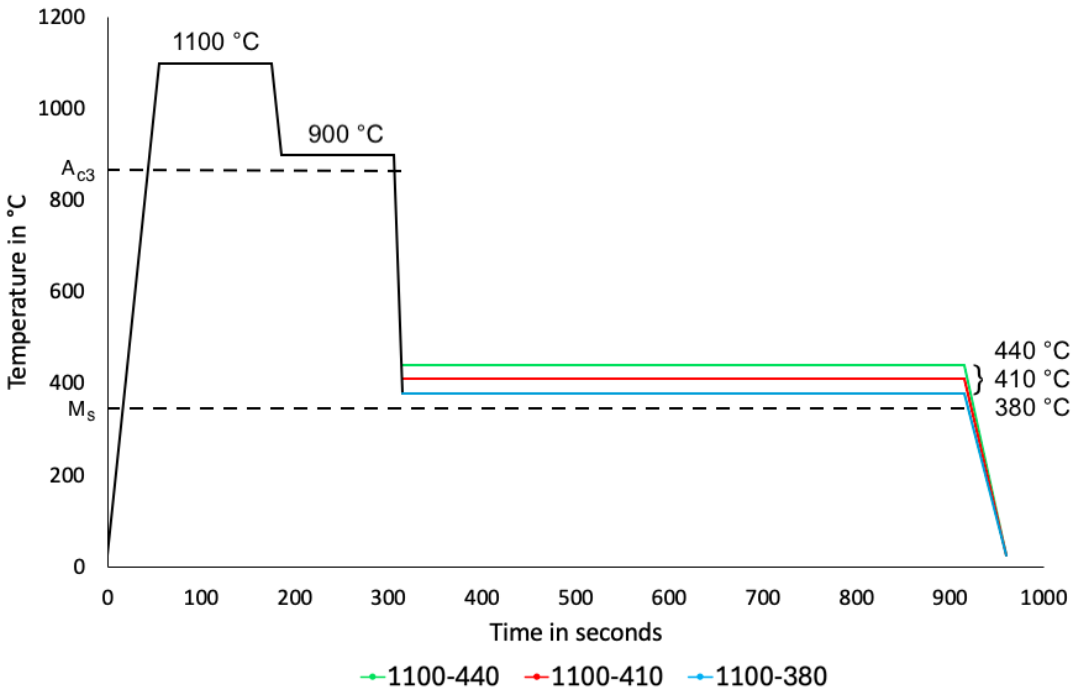

Figure 15: Heat treatments to obtain coarse PAGs in experiments performed at DESY.

reach the defined isothermal holding temperature immediately after quenching. In this study, the temperature fluctuated by up to ± 5 °C around the defined holding temperature. The fluctuations continued for up to 13 seconds until the isothermal holding temperature stabilized. However, during the time of the fluctuations, the phase transformation is expected to start already. Therefore, the starting time of the phase transformation was defined by the first temperature minimum that occurred in a range of ± 5 °C of the intended isothermal transformation temperature during the quenching process. Appendix A provides examples to clarify the definition of the starting time of the phase transformation.

As the number of specimens was limited, each specimen was used for two experiments. Between the heat treatments of the two experiments, the specimens were heated at a rate of 20 °C/s to 900 °C and were austenitized for 120 seconds. Subsequently, they were quenched at a rate of 50 °C/s to room temperature. After restoring the initial microstructure, the second experiment was conducted. The specimens used for experiments 1100-380 and 900-380 were used for a second experiment run with bainite formation at 360 °C, named 1100-360 and 900-360. These experiments were excluded from the interpretations regarding the effect of the prior austenite grain size and the isothermal transformation temperature on the phase transformation kinetics as martensite is expected to form during cooling to the isothermal transformation temperature. A schematic of a full heat treatment experienced by each specimen is presented in Figure 16.

The four specimens were named according to the following structure: X-Y-Z with X being the maximum austenitization temperature, Y being the isothermal transformation temperature of the first experiment and Z being the isothermal transformation temperature of the second experiment.

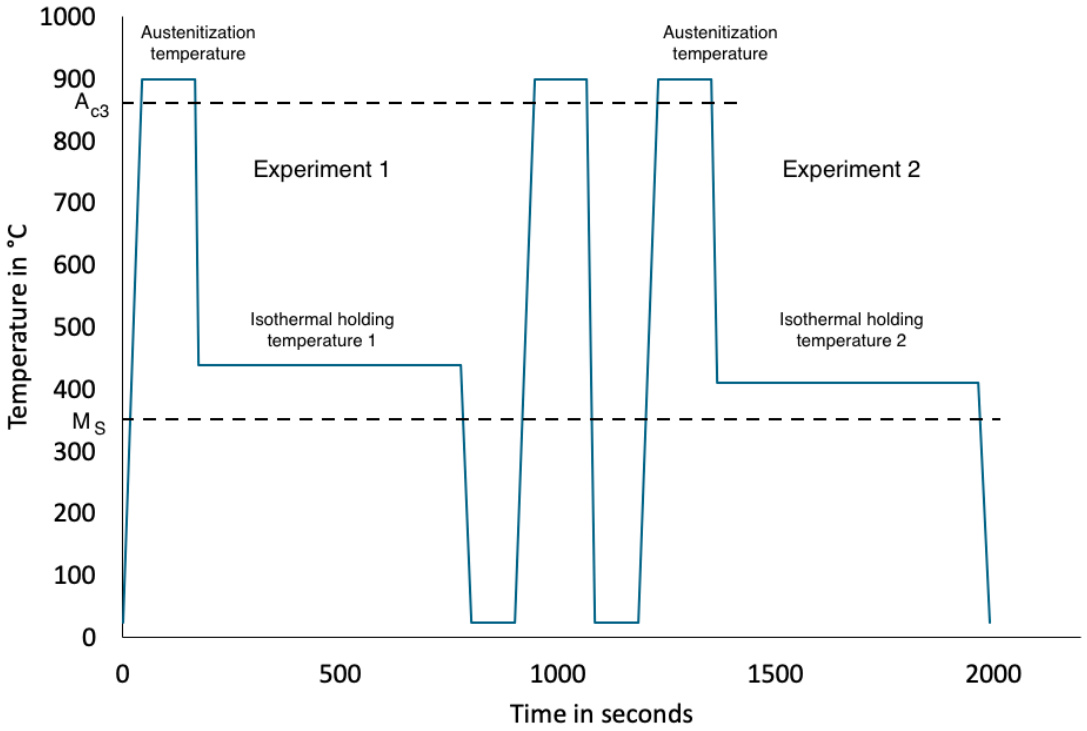

Figure 16: Heat treatment experienced by one specimen during in-situ synchrotron XRD experiments.

The individual experiments are referred to as X-Y with X being the maximum austenitization temperature and Y being the isothermal transformation temperature. All information about heat treatments experienced by the specimens and the individual experiments is given in Table 3. Performing two experiment runs per specimen implies that microstructure investigations after the formation of bainite cannot be performed for experiments 1100-440, 900-440, 1100-380 and 900-380. Therefore, the only experiments with bainite formation above M_s available for microstructure investigations are 1100-410 and 900-410. In order to obtain information on the effect of the transformation temperature on the final microstructure in specimens with different prior austenite grain sizes, the specimens transformed at 360 °C will be shown in the sections presenting and discussing the microstructure.

Specimen name	First experiment run	Second experiment run
1100-440-410	1100-440	1100-410
1100-380-360	1100-380	1100-360
900-440-410	900-440	900-410
900-380-360	900-380	900-360

Table 3: Information about specimens and experiments conducted at DESY. The second experiment run defines the final microstructure of the sample available for microstructure investigations.

3.2.2 Data processing with MAUD

After performing the in-situ synchrotron XRD experiments, 2D diffraction patterns recording the evolution in the microstructure are available. The 2D diffraction patterns need to be further processed to obtain information on the fractions, lattice parameters and microstrains of the phases. For each experiment, 15 to 20 2D diffraction patterns have been selected for further analysis with the software MAUD (version 2.999) [48]. The selection of the patterns to be analyzed was conducted using the dilatometry curves recorded simultaneously with in-situ XRD experiments. The dilatometry curves enable the estimation of the fraction of bainitic ferrite that has formed at a certain point in time in the phase transformation. In addition to the patterns recorded during the phase transformation of bainite, patterns at room temperature before the start of the heat treatment, at the end of the austenitization process and after quenching to room temperature were analyzed for each experiment.

Step 1: Integration of 2D diffraction patterns

The 2D diffraction patterns recorded during the heat treatment were integrated using the program ImageJ with an additional plug-in of the software MAUD. After calibration, all 2D diffraction patterns were integrated over the azimuthal angle range of 360°. As a result, 1D diffraction patterns with the intensity (I) as a function of the diffraction angle (2θ) were obtained for further analysis using Rietveld refinement.

Step 2: Rietveld refinement

The Rietveld analyses was performed using the software MAUD, which enables the refinement of the phase fractions, lattice parameters and microstrains for each 1D XRD pattern. The resulting phase fractions are determined from the relative intensities of bainitic ferrite (BCC, α) and austenite (FCC, γ) during the Rietveld refinement. Diffraction patterns from the later stages of the phase transformation exhibited minor fractions of carbides. However, the carbide peaks were too small to refine the carbide fraction by Rietveld analysis. The bainitic ferrite and austenite lattice parameters were determined based on their peak positions. Patterns exhibiting asymmetric austenite peaks arising from a heterogeneous carbon distribution were refined using a second austenite phase for carbon-rich austenite, which was denoted as γ^+. An example of peak asymmetry observed in the diffraction patterns is depicted in Appendix B. The microstrain present in bainitic ferrite and austenite was a direct output parameter of the Rietveld refinement. The software MAUD is capable of separating the simultaneous effects of crystallite size and microstrain on peak profiles, using the method described in the publication of Lutterotti and Scardi [49], which enables to determine the microstrain present in a phase from the recorded XRD patterns.

The quality of the individual refinements was evaluated using three different indicators: the standard deviation of the profile function, weighted profile R-factor and the visual fit of the refined function. The range of the refinement was reduced to $2.0 \leq 2\theta \leq 6.9$, since no peaks were vis-

ible at 2θ angles smaller than 2.0 and all Debye-Scherrer rings at 2θ angles larger than 6.9 were incomplete as a result of the limited detector size. The remaining 2θ range includes the following peaks: $\{111\}_\gamma$, $\{200\}_\gamma$, $\{220\}_\gamma$, $\{311\}_\gamma$, $\{222\}_\gamma$, $\{110\}_\alpha$, $\{200\}_\alpha$, $\{211\}_\alpha$ and $\{220\}_\alpha$. At the beginning of the phase transformation to bainite, only austenite grains were expected to be present. Especially for experiments with the maximum austenitization temperature at 1100 °C, prior austenite grains can be relatively large, which can result in discontinuous Debye-Scherrer rings that exhibit relatively large individual spots. This affects the shape of FCC peaks in the 1D diffraction patterns and hence the accuracy of the refinement. An example of the effect of large PAGs on the Debye-Scherrer rings and the peak shape in the 1D diffraction patterns is presented in Appendix C . Therefore, the values of the phase fraction, lattice parameter and microstrain of austenite during austenitization and at the beginning of the phase transformation may be less accurate for experiments with a maximum austenitization temperature of 1100 °C. Bainitic ferrite sheaves divide large austenite grains into smaller areas, which is the reason why the perviously mentioned inaccuracies become insignificant after a fraction of approximately 10 wt.% of bainitic ferrite has formed. Information about the individual refinements is provided in Appendix D.

Step 3: Error estimation

After calibrating the experimental set-up, the lattice parameter obtained from the refinement of the XRD patterns compared to the NIST standard value is expected to be $\pm\ 1.7 \times 10^{-4}$ Å [6]. However, differences in the specimen-to-detector distance or inaccuracies in temperature measurements may increase the error when it comes to the comparison between different experiments. Therefore, the expected relative error of the lattice parameter was determined by refining XRD patterns at the end of austenitization, right before quenching to the isothermal transformation temperature. At this point in the heat treatment, the lattice parameter of austenite should be the same for all specimens. Therefore, the average of the standard deviation, calculated from the variation of the austenite lattice parameter among the experiments, was used to estimate the relative error. The error determined for the lattice parameter is 0.035 %. Due to the effect of large PAGs on the accuracy of values refined from patterns recorded during austenitization, only patterns of experiments with no or little effect of discontinuous or spotty Debye-Scherrer rings on the peak shapes have been selected for the error determination.

To estimate the relative error of the microstrain, the refined XRD patterns from the end of austenitization could not be used. The effect of large PAGs on the peak shapes significantly affects the value of the microstrain. Therefore, the same procedure as described for the determination of the relative error of the lattice parameter was performed using XRD patterns recorded before the heat treatment of the first experiment run started. At this point, the initial microstructure should be equivalent for all specimens and hence the microstrain of BCC should be similar. However, the relative error calculated from these patterns only includes differences in the specimen-to-detector distance and not potential inaccuracies in temperature measurements. The error determined for

the microstrain is 3.932 %.

The estimated error of the phase fractions was given as a direct output parameter of the Rietveld refinement of the in-situ synchrotron XRD data. Therefore, an individual error was determined for each phase fraction refined and is listed in Appendix D. The errors are indicated by error bars in the plots presented in the following chapters.

The temperature fluctuations and the effect of large prior austenite grains on the peak shapes in the 1D XRD patterns affect the values of the phase fractions, lattice parameters and microstrains determined at the beginning of the phase transformation. Furthermore, the visual fit of the refined function at bainitic ferrite peaks was less accurate when the fraction of bainitic ferrite was very low. The temperature in the center of the specimen stabilized after approximately 13 seconds. The effect of large PAGs on the peak shapes is expected to be reduced significantly after approximately 10 wt.% of bainitic ferrite has formed, which can take up to 20 seconds. Also the visual fit of the refined function at bainitic ferrite peaks can be expected to be appropriate after 10 wt.% of bainitic ferrite has formed. All three phenomena affect the values determined from the refinement of XRD patterns recorded at the beginning of the phase transformation. To raise the reader's awareness for these effects, all plots are provided with a transparent gray box positioned in front of the first 20 seconds of the phase transformation.

3.3 Interrupted quenching experiments

Interrupted quenching experiments were performed in order to investigate the microstructure formed in the early stages of the phase transformation. Specimens used for the interrupted quenching experiments were prepared and heat treated as described in section 3.1. The interrupted quenching heat treatments were performed using a Bähr 805 A/D dilatometer, equipped with two quartz rods to place the specimens in the dilatometer. The specimens were heated by an induction coil. Quenching was performed by spraying helium gas on the specimen. To measure and control the temperature, a thermocouple was spot-welded in the middle of the specimen.

The interrupted quenching heat treatments were similar to the heat treatments performed at DESY. The only difference was the interruption of the heat treatment in the early stages of the phase transformation to bainite by quenching to room temperature. The holding times at the isothermal transformation temperature were between 15 to 40 seconds, depending on the combination of the PAG size and transformation temperature. The selection of the holding times for each prior austenite grain size and isothermal transformation temperature combination was conducted using the dilatometry curves recorded during the experiments at DESY.

The interrupted quenching specimens were named according to the following structure: IQ-X-Y-Z with IQ referring to "interrupted quenching", X being the maximum austenitization temperature, Y being the isothermal transformation temperature and Z being the holding time before quenching

to room temperature. All specimens that were part of the interrupted quenching experiments are listed in Table 4. The interrupted quenching experiments also include specimens that were transformed at 360 °C, since the potential formation of martensite during quenching to 360 °C was detected during the analysis of the in-situ synchrotron XRD data. At that time the interrupted quenching experiments were already performed, which is the reason why the samples transformed at 360 °C will be shown in the sections presenting and discussing the microstructure of the interrupted quenching experiments. After the interrupted quenching heat treatment, the samples were prepared for OM and SEM investigations.

specimen name	Austenitization temperature	Isothermal transformation temperature	Holding time
IQ-1100-440-40	1100 °C	440 °C	40 s
IQ-1100-440-15	1100 °C	440 °C	15 s
IQ-900-440-15	900 °C	440 °C	15 s
IQ-1100-380-30	1100 °C	380 °C	30 s
IQ-1100-380-15	1100 °C	380 °C	15 s
IQ-900-380-15	900 °C	380 °C	15 s
IQ-1100-360-25	1100 °C	360 °C	25 s
IQ-1100-360-15	1100 °C	360 °C	15 s
IQ-900-360-15	900 °C	360 °C	15 s

Table 4: Austenitization temperature, isothermal transformation temperature and holding time of interrupted quenching experiments.

3.4 Microstructure investigations with OM, SEM and EBSD

3.4.1 Specimen preparation

For metallographic specimen preparation, 4 to 5 specimens were clamped in a metallic specimen holder, as shown in Figure 17. This enables to prepare and characterize the sides of several specimens at the same time. Grinding of the specimens was performed in six steps, with the finest emery paper in the final step being a P2000 EU SiC grit. After grinding, the specimens were cleaned for five minutes using ultrasonic cleaning in isopropanol. Then polishing was performed at 3 µm, followed by polishing at 1 µm. Each step was performed for 5 minutes using diamond polishing paste and isopropanol. Ultrasonic cleaning in isopropanol was conducted between the polishing steps, as well as after the last polishing step, for 5 minutes.

3.4.2 Optical microscopy and scanning electron microscopy

Specimens that were prepared for OM and SEM were etched using a 2 % Nital solution for 1 to 2 seconds, to highlight the differences between bainitic ferrite, martensite and austenite in the microstructure under the microscope. Finally, the specimens were cleaned using ultrasonic cleaning in isopropanol for five minutes. Between all cleaning steps, the specimens were dried thoroughly

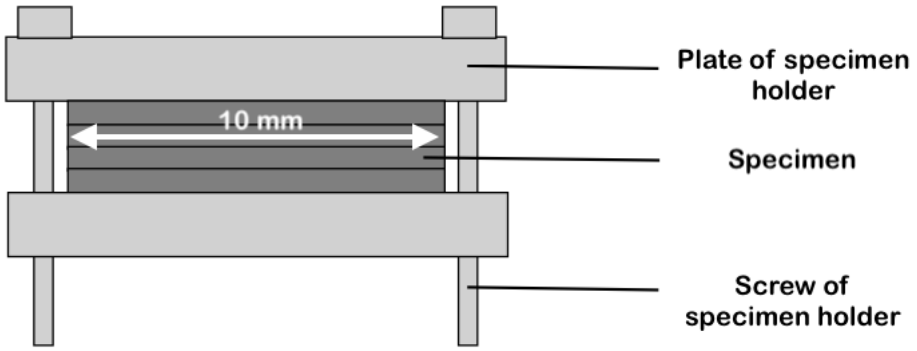

Figure 17: Schematic of specimens clamped in specimen holder.

to avoid corrosion due to water remaining inside the gaps between the specimens in the specimen holder.

For optical microscopy, a Keyence VHX-7000 digital microscope was used. During characterization with the optical microscope, the specimens were kept inside the specimen holder. Before OM, the specimen holder was leveled to ensure that the surface of the specimens is not tilted. Images were taken at different magnifications. Lower magnifications were chosen to gain a general overview of the microstructure formed at different PAG size and isothermal transformation temperature combinations, while higher magnifications were chosen to analyze details in the microstructure.

Scanning electron microscopy was conducted with a JEOL JSM-IT800 scanning electron microscope using a 10 kV electron beam and a working distance of 10 mm. Before SEM, the specimens were removed from the specimen holder and cleaned with acetone. After the specimens were cleaned and dried, they were clamped into a specimen holder for SEM individually. The contrast and brightness settings were adjusted to obtain images with differences between bainitic ferrite, austenite, martensite and carbides.

3.4.3 Electron backscatter diffraction

Electron backscatter diffraction (EBSD) was used for prior austenite grain reconstruction and grain size analysis of the four specimens that are listed in Table 3. The specimens were initially prepared as explained in section 3.4.1 followed by polishing with a diamond paste of 1 µm and a Struers MD-Nap polishing cloth for 10 minutes. Subsequently, the specimens were cleaned with ethanol and final polishing step was conducted for 10 minutes using OPU (0.05 µm) and a MD-Chem polishing cloth. Both polishing steps were performed manually. After the specimens were cleaned for 5 minutes using ultrasonic cleaning and dried using compressed air, the specimens were mounted in a 70° pre-tilted specimen holder for EBSD experiments.

The EBSD measurements were performed using a Zeiss Sigma 560 SEM system, equipped with an Oxford Instrument Symmetry 3 CMOS detector with a maximum acquisition rate of approximately

5000 frames per second. The data were collected with the software AZtec HKL. The specimen working distance was set to 16 mm. An acceleration voltage of 20 kV and the probe current was approximately 100 nA was used. After converting the signal from binary signal to text signal, the data was post-processed using MTEX Matlab toolbox for PAG reconstruction and grain size analysis.

4 Results

4.1 Experiments with coarse prior austenite grains

4.1.1 Austenitic state and microstructure

Prior austenite grain reconstruction using EBSD measurements was used to estimate the prior austenite grain size after austenitization at 1100 °C. The prior austenite grain size determined for 1100-440-410 and 1100-380-360 was 68.1 µm and 64.5 µm, respectively. The PAG size distribution of the specimens is provided in Appendix E.

The austenitization process was controlled by analyzing XRD patterns recorded at the end of the austenitization for each experiment. Visual analyses of these XRD patterns revealed that the specimens were not fully austenitic at the end of the austenitization treatment. Very small peaks located at 2θ angles of ferrite peaks were detected when analyzing the patterns on the logarithmic scale. However, the peaks were too small to quantify the ferrite fraction using Rietveld refinement. Visual comparison of the XRD patterns exhibited that the ferrite peaks are similarly pronounced in the XRD patterns of all three specimens. The XRD patterns used for visual comparison are provided in Appendix F. Figure 18 exhibits an SEM image with ferrite detected during microstructure investigations of specimens that are part of the interrupted quenching experiments. These specimens experienced the same austenitization heat treatment as the specimens investigated at DESY, which is the reason why the presence of ferrite after austenitization can also be expected in the specimens that are part of the interrupted quenching experiments. However, it cannot be confirmed whether the ferrite detected in Figure 18 was left after the austenitization treatment or formed during quenching to the isothermal transformation temperature.

Figure 18: Ferrite detected in IQ-1100-360-15. F: ferrite.

The microstructures formed after isothermal bainite formation at 410 °C and 360 °C are available for microstructure investigations. Figure 19 presents optical microscopy images of 1100-410 and 1100-360. Bainitic ferrite sheaves appear in darker color and can be recognized by their plate-shaped pattern. The bright islands distributed in the microstructure are expected to be blocky retained austenite. In some places film-like retained austenite that separates individual laths in bainitic ferrite sheaves can be identified, recognizable by their bright color. Examples of the microstructural features identified in the images are indicated by arrows in Figure 19. When comparing the microstructures developed in the two experiments, it is noticeable that there are fewer and smaller blocks of retained austenite in the microstructure of 1100-360.

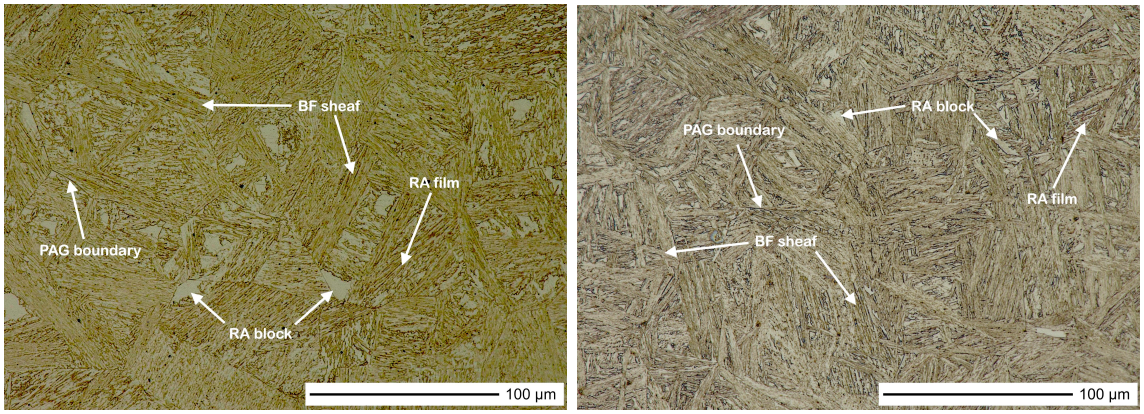

(a) 1100-410 (b) 1100-360

Figure 19: OM images of microstructure formed in experiments 1100-410 and 1100-360. RA: retained austenite, BF: bainitic ferrite and PAG: prior austenite grain.

Furthermore, visual analyses of XRD patterns recorded during the progress of the phase transformation revealed carbide precipitation. The carbide fractions are expected to be relatively small, since carbide peaks could only be detected when XRD patterns were analyzed on the logarithmic scale. Therefore, the carbide fractions could not be quantified using Rietveld refinement. XRD patterns recorded right before quenching to room temperature were visually analyzed for all experiments to determine the effect of the transformation temperature on the carbide fraction. From these patterns, it could be derived that the carbide fraction formed increases with decreasing transformation temperatures. The carbide peak positions indicate that the carbides found in the microstructure may be ϵ carbides. XRD patterns used to analyze the effect of the transformation temperature on the carbide fraction are provided in Appendix F. During microstructure investigations of interrupted quenching experiments, carbides that precipitated from bainitic ferrite in experiment IQ-1100-360-15 could be detected and are presented in Figure 20a. Figure 20b exhibits that carbide precipitation from bainitic ferrite in IQ-1100-440-40 is much less pronounced or may be even absent. This indicates that there may be a transition from upper to lower bainite in the investigated temperature range.

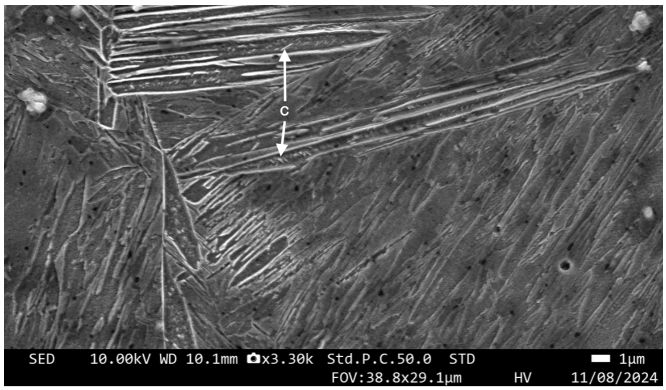

(a) Carbides precipitated from bainitic ferrite in IQ-1100-360-15

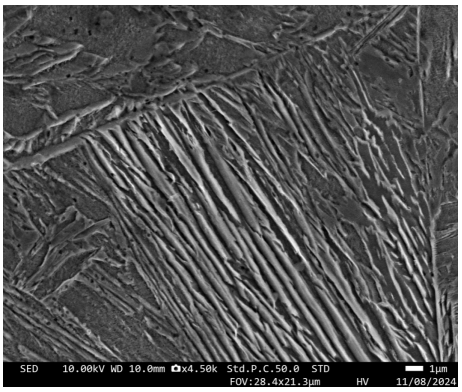

(b) Absence of carbide precipitation from bainitic ferrite in IQ-1100-440-40

Figure 20: Carbides precipitated from bainitic ferrite in IQ-1100-360-15. C: carbides.

4.1.2 Evolution of phase fractions

Figure 21 presents the fraction of bainitic ferrite formed as a function of time during isothermal holding in experiments with coarse prior austenite grains. The fraction of bainitic ferrite plotted in Figure 21 does not include potential changes in the BCC fraction due to the formation of fresh martensite during quenching to room temperature. The first 20 seconds of the phase transformation are displayed in gray to indicate the existence of potential inaccuracies in the refined values arising from the effect of large prior austenite grains on the FCC peak shapes as well as the relatively small fraction of bainitic ferrite present in that time frame.

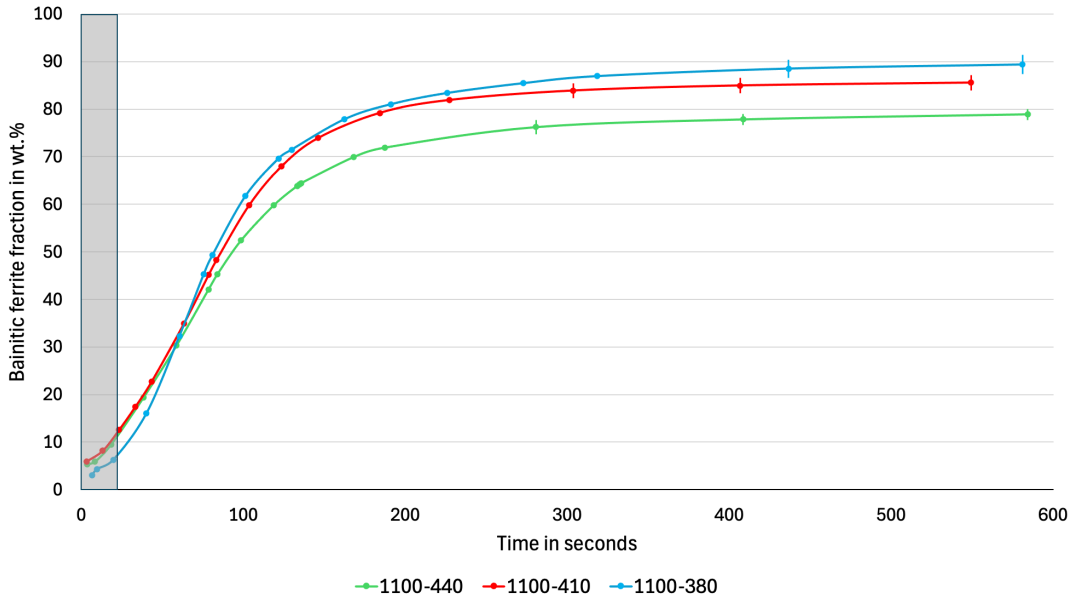

Figure 21: Bainitic ferrite fraction in wt.% vs. time (experiments with coarse PAGs)

Figure 21 shows that after 600 seconds of holding at the isothermal transformation temperature, all curves still exhibit a slight inclination, indicating that transformation stasis has not been reached at the end of the experiment. As the isothermal transformation temperature is decreased, the fraction

of bainitic ferrite formed at the end of the holding increases, which can be explained by the higher carbon concentration at the thermodynamic limit, T_0', at lower transformation temperatures [14]. Focusing on the first 100 seconds of isothermal holding, it becomes recognizable that 1100-440 and 1100-410 appear to initially transform faster than 1100-380. However, the steepness of the curve's slopes indicates that the maximum transformation rate increases with decreasing transformation temperatures and thus the transformation of 1100-380 becomes the fastest after approximately 60 seconds of holding. The effect of the transformation temperature on the transformation rate is related to the increase in driving force for bainite formation with decreasing transformation temperatures, which results in an acceleration of the phase transformation kinetics [9, 32].

The fractions of bainitic ferrite, retained austenite and fresh martensite, present after quenching to room temperature, are presented in Table 5. The fraction of fresh martensite was calculated by subtracting the fraction of bainitic ferrite, obtained from the last XRD pattern refined before quenching to room temperature, from the fraction of BCC phases, refined from a pattern recorded after quenching to room temperature. The fraction of retained austenite increases with increasing transformation temperatures, which may be explained by the smaller fraction of bainitic ferrite formed at higher transformation temperatures and hence the higher fraction of remaining austenite being present before quenching to room temperature. 1100-440 exhibits the highest fraction of fresh martensite formed during quenching to room temperature. This can be related to the smaller fraction of bainitic ferrite formed, which results in a smaller amount of carbon to partition into a higher fraction of remaining austenite. This leads to a lower carbon concentration in the austenite and thus to a lower austenite stability [7, 50]. Furthermore, the smaller fraction of bainitic ferrite formed at higher transformation temperatures causes the presence of larger austenite blocks, resulting in longer diffusion distances for carbon, which may extend the homogenization process, despite the higher carbon diffusivity at higher transformation temperatures.

Experiment	Bainitic ferrite	Retained austenite	Fresh martensite
1100-440	79 ± 1	17 ± 1	4 ± 1
1100-410	85 ± 2	13 ± 1	2 ± 1
1100-380	89 ± 2	9 ± 2	2 ± 2

Table 5: Fractions of bainitic ferrite, retained austenite and fresh martensite in wt.% present after quenching to room temperature (experiments with coarse PAGs).

4.1.3 Evolution of bainitic ferrite and austenite lattice parameters

The lattice parameters of bainitic ferrite and austenite were obtained from the Rietveld refinement of the in-situ synchrotron XRD data. Changes in the lattice parameters can be induced by three different processes. One of them is the partitioning of carbon from bainitic ferrite into the remaining austenite, which causes the lattice parameter of bainitic ferrite to decrease and the one of austenite to increase [19, 22]. Secondly, there is the precipitation of carbides, which removes carbon from

the bainitic ferrite or the austenite matrix and hence results in a decrease in the respective lattice parameter. Finally, there are transformation stresses resulting from the volume expansion during the phase transformation from FCC to BCC, leading to the presence of isostatic compressive stresses and hence a decrease in the lattice parameter. These transformation stresses increase with decreasing transformation temperatures and increasing holding times [19].

The starting values of the lattice parameters presented in the following plots differ because of the different isothermal holding temperatures in the experiments, which leads to an increase in the lattice parameter with increasing transformation temperatures as a result of thermal expansion. The first 20 seconds of the phase transformation are displayed in gray to indicate the influence of the temperature fluctuations, as well as the effect of large prior austenite grains on the FCC peak shapes, on the values refined from patterns recorded in the beginning of the phase transformation. In figures that plot a value as a function of the bainitic ferrite fraction, the values recorded before a fraction of approximately 10 wt.% of bainitic ferrite was formed are displayed in gray.

Figure 22a presents the evolution of the lattice parameter of bainitic ferrite as a function of time. Neglecting the fluctuations at the beginning of the holding, the evolution of the bainitic ferrite lattice parameter may be divided into two stages. The first stage exhibits a rapid increase in the value of the lattice parameter. Depending on the isothermal transformation temperature, the increase takes between 60 and 90 seconds. During the second stage, the lattice parameter of bainitic ferrite gradually decreases. The initial increase may be explained by the process of carbon partitioning. As the phase transformation progresses, the partitioning process leads to an increasing carbon concentration in the remaining austenite. According to the diffusionless theory, bainitic ferrite forms inheriting the carbon concentration of the parent austenite [14], resulting in a larger lattice parameter as new bainitic ferrite sub-units form from austenite containing an increased carbon concentration. Figure 22b exhibits that the increase in the lattice parameter of bainitic ferrite gradually slows down as the fraction of bainitic ferrite formed increases. The transition between stage 1 and stage 2 may be explained by the fact that the values recorded by in-situ synchrotron XRD are always an average over the whole area illuminated by the beam. While new bainitic ferrite sub-units form with a higher carbon concentration and hence with a larger lattice parameter, the carbon concentration in already existing sub-units decreases, due to carbon partitioning into the remaining austenite. Depending on the transformation temperature, a decrease in the lattice parameter becomes apparent after 60 wt.% to 70 wt.% of bainitic ferrite has formed. At this point in time, the loss of carbon by partitioning becomes visible in the graph due to the decreasing value of the bainitic ferrite lattice parameter.

Figure 23 shows the evolution of the average lattice parameter of austenite during the phase transformation. To plot the lattice parameter of austenite, the average between the lattice parameters of γ and $\gamma+$, considering the respective phase fractions, has been calculated. The increase in the average austenite lattice parameter with time, visible in Figure 23a, can be related to the car-

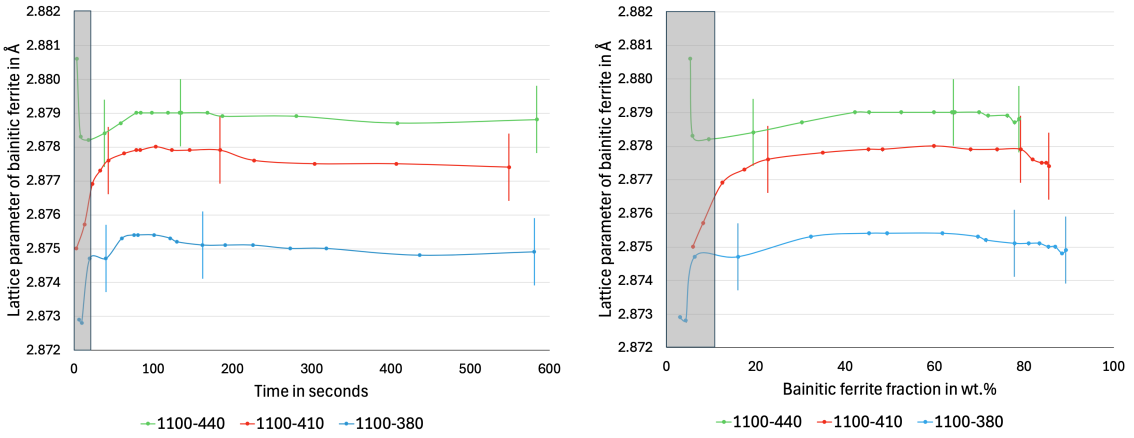

(a) Lattice parameter vs. time.

(b) Lattice parameter vs. bainitic ferrite fraction.

Figure 22: Evolution of the lattice parameter of the bainitic ferrite during the phase transformation (experiments with coarse PAGs).

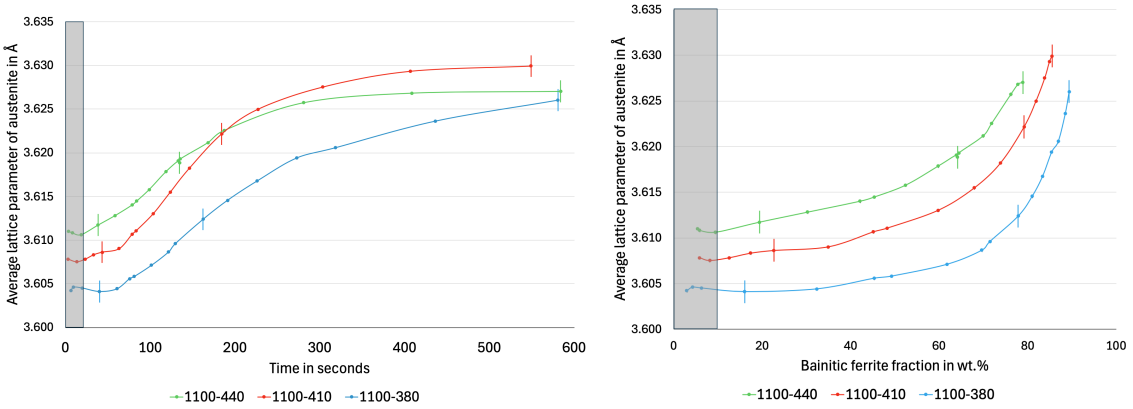

(a) Lattice parameter vs. time.

(b) Lattice parameter vs. bainitic ferrite fraction.

Figure 23: Evolution of the average lattice parameter of the remaining austenite during the phase transformation (experiments with coarse PAGs).

bon enrichment of austenite due to partitioning from bainitic ferrite. The curves of 1100-440 and 1100-410 exhibit a rapid initial increase in the austenite lattice parameter, followed by a gradual decrease of the slope until the curves are almost flat at the end of the isothermal holding. In contrast, the average austenite lattice parameter of 1100-380 increases at a relatively slow rate. However, the slope of its curve remains significant until the end of the isothermal holding. These differences may be explained by the slower carbon diffusion at lower temperatures, resulting in a slower carbon partitioning process at decreasing transformation temperatures. Therefore, the austenite lattice parameter increases at a slower rate but continues to increase for a prolonged time. The steady increase of the average austenite lattice parameter of 1100-380 at the end of the experiment indicates that the partitioning process may not be completed after 600 seconds of holding.

4.1.4 Evolution of microstrain in bainitic ferrite

The microstrain present in bainitic ferrite was a direct output parameter of the Rietveld refinement of the in-situ synchrotron XRD data. Figure 24 plots the microstrain as a function of time. When comparing the different curves, it can be observed that the microstrain is higher for lower transformation temperatures. Neglecting the first 20 seconds of the phase transformation, a steady decrease in microstrain can be observed in the curves of 1100-440 and 1100-410. The microstrain in the bainitic ferrite in 1100-380 exhibits an initial increase, followed by a short stagnation until it starts gradually decreasing after approximately 100 seconds of holding.

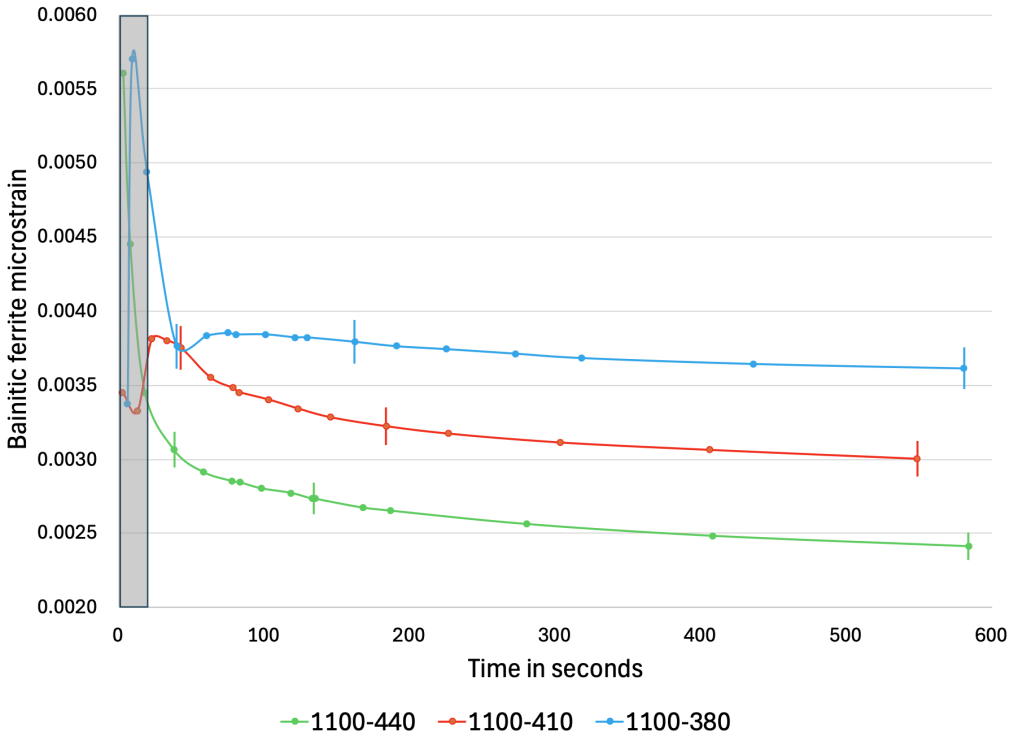

Figure 24: Microstrain in bainitic ferrite vs. time (experiments with coarse PAGs).

The observed evolution of the microstrain may be explained by the dislocation density in the bainitic ferrite. The accommodation of dislocations in an atomic lattice is accompanied by local stress fields and hence causes the presence of non-uniform strains in their vicinity [51]. These non-uniform strains result in X-ray diffraction line broadening, which can be analyzed in XRD patterns to gain information on the dislocation density [52]. Therefore, the higher microstrain observed for lower transformation temperatures can be related to a higher dislocation density present in the bainitic ferrite.

The displacive phase transformation mechanism causes plastic deformation of the austenite in the vicinity of the interface with the growing bainitic ferrite. As the austenite deforms plastically, dislocations accumulate, which later are inherited by the bainitic ferrite [6, 53]. Hence, the higher strength of the phases at lower transformation temperatures causes the formation of a higher number of dislocations during the phase transformation from FCC to BCC. The steady decline in

the value of the microstrain may be related to the recovery of the defect structure [6, 19]. Recovery is a thermally activated process resulting in a decrease in the dislocation density [54]. Therefore, the decrease in microstrain at higher transformation temperatures is more pronounced than at lower transformation temperatures.

4.1.5 Interrupted quenching experiments

Figure 25 presents optical microscopy images of interrupted quenching experiments. Three specimens with a course prior austenite grain structure isothermally transformed at 440 °C, 380 °C and 360 °C for 40, 30 and 25 seconds respectively, were selected to be presented. Interrupting the phase transformation in the early stages makes it possible to investigate the effect of the transformation temperature on the prevalent nucleation site. Bainitic ferrite that primarily formed along grain boundaries is indicated by the letters "GB". Longer bainitic ferrite sheaves that consist of many successive autocatalytic nucleation events are indicated by the letter "A".

Figure 25a and Figure 25b show images of experiment IQ-1100-440-40. It is recognizable that a relatively small fraction of bainitic ferrite has formed after 40 seconds of holding. Its microstructure shows thin, as well as relatively broad sheaves that have gown through the grains. Furthermore, there are grains clearly showing bainitic ferrite nucleation that is concentrated at the prior austenite grain boundaries. Figure 25c and Figure 25d show images of experiment IQ-1100-380-30. Figure 25c, which was taken at a site, located close to a pushrod during the heat treatment in the dilatometer, shows a significantly higher transformation degree than Figure 25d. Both figures show many sheaves that have grown through prior austenite grains. There are some areas that could indicate bainitic ferrite formation that is concentrated at the prior austenite grain boundaries, however, it is difficult to make a clear distinction from broad sheaves. Figure 25e and Figure 25f show images of experiment IQ-1100-360-25. Thin, as well as relatively broad sheaves are visible in both images. Figure 25f shows bainitic ferrite nucleation that is concentrated at the prior austenite grain boundaries.

The SEM images presented in Figure 26 show details of the bainitic ferrite sheaf morphology formed in the early stages of the phase transformation of selected specimens that are part of interrupted quenching experiments. All four figures show sheaves that have grown relatively large by successive events of autocatalytic nucleation. Figure 26a presents both morphologies, long sheaves, as well as bainitic ferrite that grows along the grain boundary.

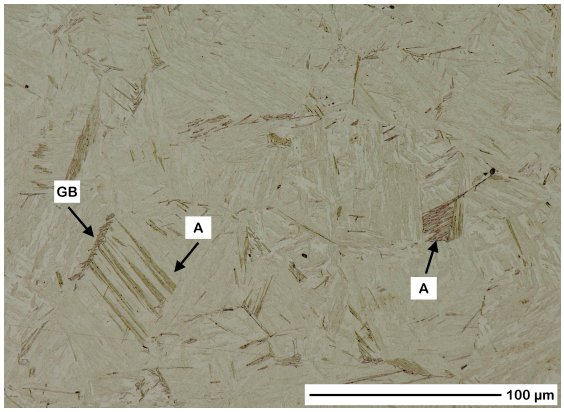

(a) IQ-1100-440-40

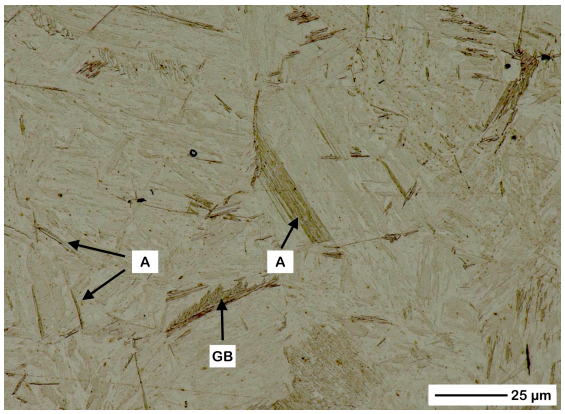

(b) IQ-1100-440-40

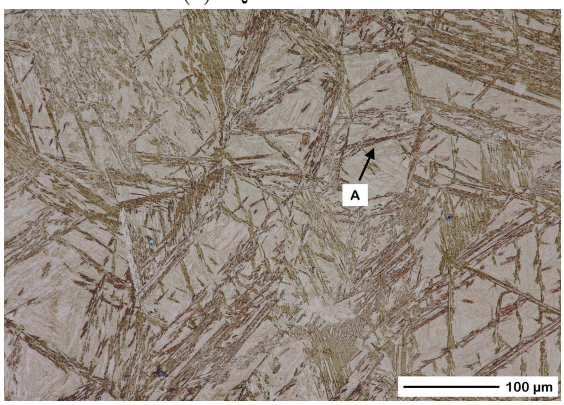

(c) IQ-1100-380-30

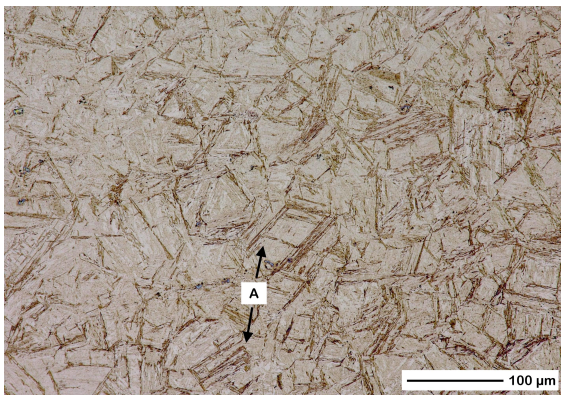

(d) IQ-1100-380-30

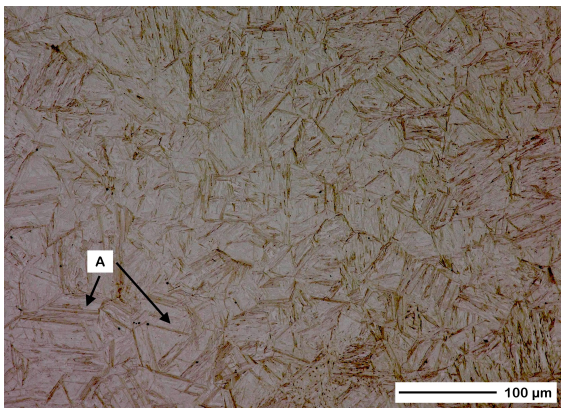

(e) IQ-1100-360-25

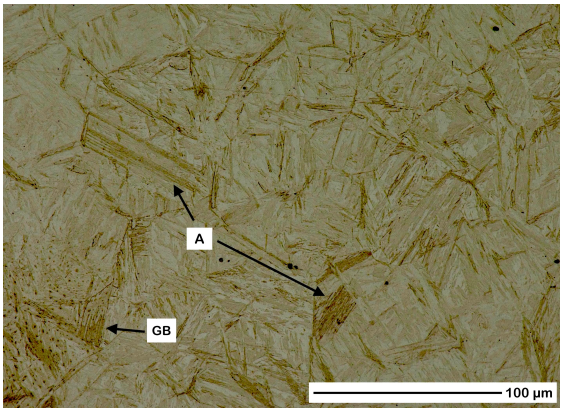

(f) IQ-1100-360-25

Figure 25: Optical microscopy images of interrupted quenching tests. GB: bainitic ferrite that primarily formed at grain boundaries. A: longer bainitic ferrite sheaves that consist of many successive autocatalytic nucleation events.

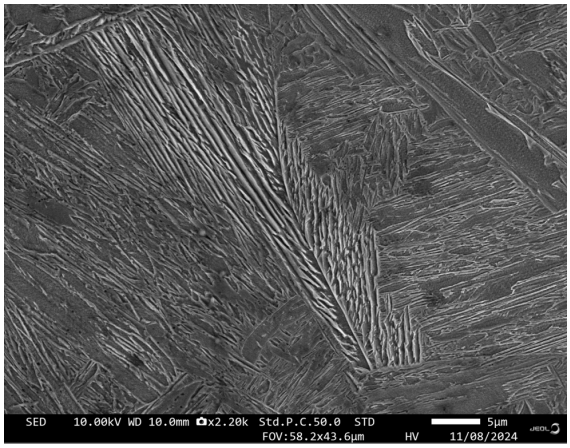

(a) IQ-1100-440-40

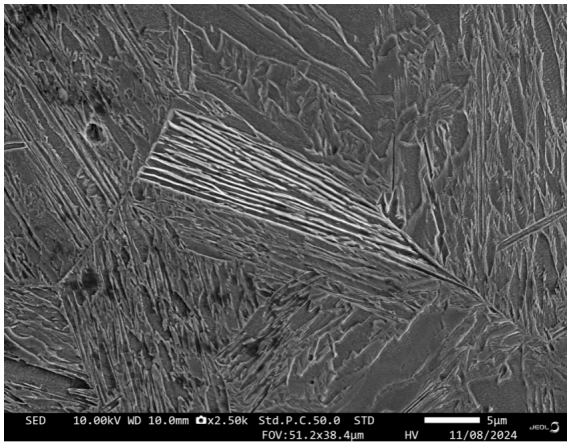

(b) IQ-1100-440-40

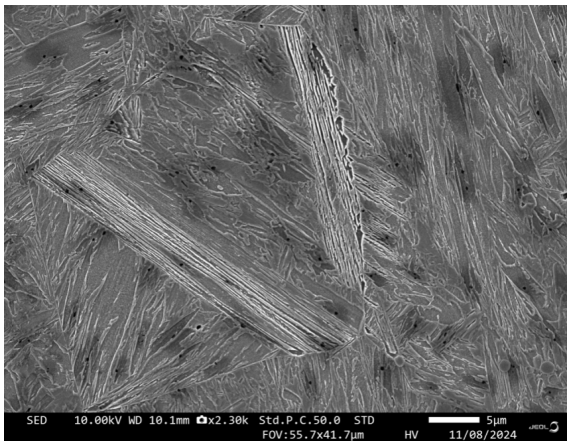

(c) IQ-1100-360-15

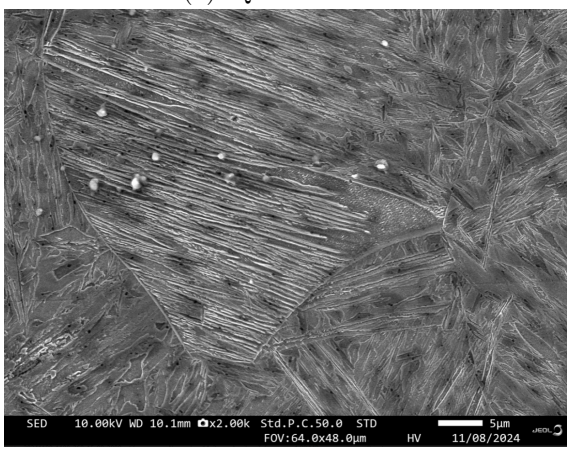

(d) IQ-1100-360-15

Figure 26: SEM images of details of the bainitic ferrite morphology observed in specimens of interrupted quenching experiments.

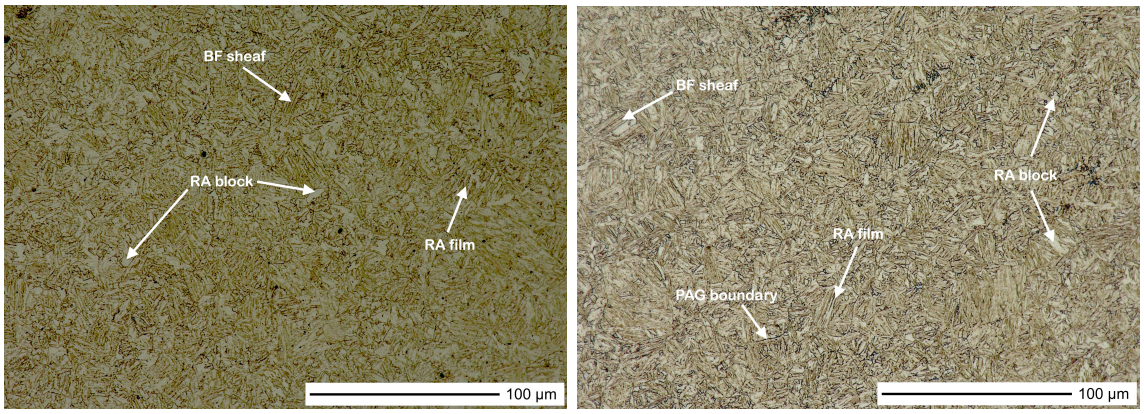

(a) 900-410 (b) 900-360

Figure 27: OM images of microstructures formed in experiments 900-410 and 900-360. RA: retained austenite, BF: bainitic ferrite and PAG: prior austenite grain.

4.2 Experiments with fine prior austenite grains

4.2.1 Austenitic state and microstructure

The prior austenite grain sizes determined by the use of EBSD measurements where 14.6 µm and 13.9 µm for 900-440-410 and 900-380-360, respectively. Appendix E provides the PAG size distribution of the two specimens.

Visual diffractogram analysis was used to control the effectiveness of the austenitization heat treatment. The XRD patterns analyzed are provided in Appendix F. It was observed, that ferrite peaks were also present at the end of the austenitization treatment in some of the experiments with fine prior austenite grains. 900-410 and 900-380 exhibited a relatively similar fraction of ferrite remaining at the end of the austenitization treatment. However, no ferrite or a significantly smaller fraction of ferrite was detected in 900-440.

Figure 27 presents optical microscopy images of the microstructures formed in experiments 900-410 and 900-360. A relatively fine microstructre consisting of bainitic ferrite sheaves and retained austenite blocks and films is visible. Arrows indicate examples of the microstructural features detected in Figure 27.

Figure 28 presents SEM images of details detected in the microstructure of experiment 900-410. The arrows in Figure 28a indicate film-like and blocky retained austenite, prior austenite grain boundaries and individual bainitic ferrite laths. Figure 28b presents a relatively large block consisting of retained austenite at the interfaces with bainitic ferrite and fresh martensite located in the middle of the block. The fresh martensite is recognizable by its darker color and textured structure. The gradual transformation from white on the outside of the block to dark gray in the middle of the block indicates the presence of a carbon concentration gradient. Therefore, it may be expected that 600 seconds of isothermal holding at 410 °C are not sufficient to reach a

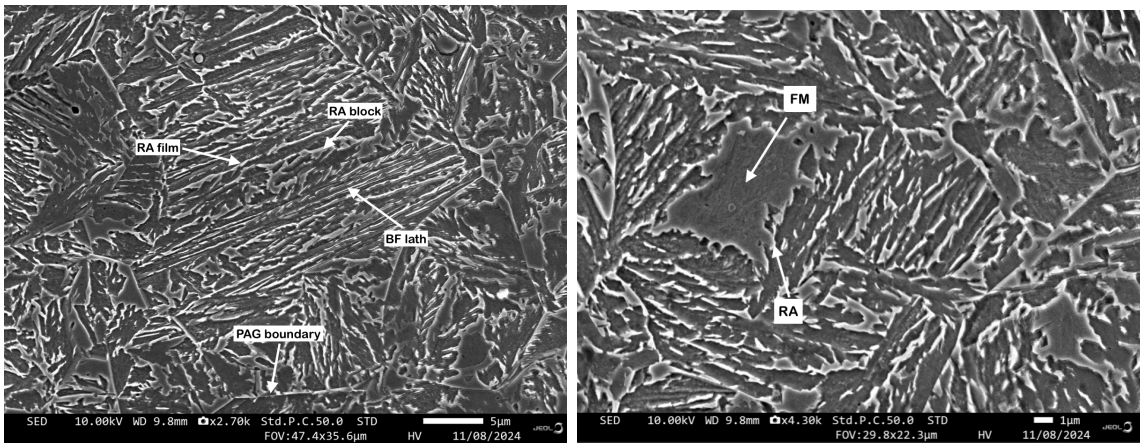

(a) Bainitic ferrite and retained austenite.

(b) Retained austenite and fresh martensite.

Figure 28: SEM images showing the microstructure formed in experiment 900-410. RA: retained austenite, BF: bainitic ferrite and FM: fresh martensite.

homogeneous carbon distribution in remaining austenite blocks. Thus, areas of austenite that were not sufficiently enriched in carbon transformed to fresh martensite during quenching to room temperature.

Furthermore, carbide peaks were detected during visual diffractogram analysis of patterns recorded during the phase transformation. When comparing the patterns recorded before quenching to room temperature, it can be recognized that the carbide peaks are more pronounced in experiments at lower transformation temperatures. The XRD patterns analyzed to compare the carbide fractions are provided in Appendix F.

4.2.2 Evolution of phase fractions

Figure 29 presents the fraction of bainitic ferrite formed as a function of time for experiments with fine prior austenite grains. All curves exhibit a slight inclination at the end of the holding at the isothermal transformation temperature, indicating that transformation stasis was not yet reached in all experiments. The fraction of bainitic ferrite formed after 600 seconds of holing increases as the transformation temperature decreases. When focusing on the first 100 seconds of the phase transformation, it can be observed that 900-440 transforms the fastest. 900-410 exhibits the second fastest transformation kinetics, closely followed by 900-380. 900-440 appears to reach the highest transformation rate and hence exhibits the fastest phase transformation kinetics of the experiments with fine PAGs until its curve has significantly flattened after approximately 72 wt.% of bainitic ferrite was formed.

Table 6 shows the fractions of bainitic ferrite, retained austenite and fresh martensite in wt.% present in the microstructure after quenching to room temperature. The fraction of retained austenite increases as the transformation temperature increases, which may be explained by the smaller fraction of bainitic ferrite formed at higher transformation temperatures and hence the

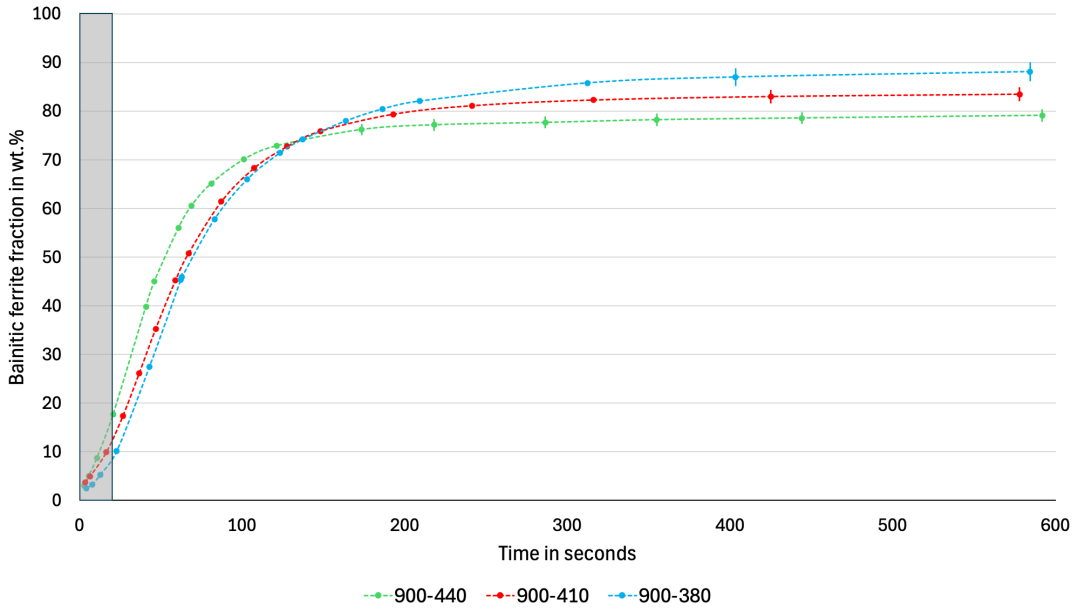

Figure 29: Bainitic ferrite fraction in wt.% vs. time (experiments with fine PAGs).

higher fraction of remaining austenite present before quenching to room temperature. The fraction of fresh martensite formed during quenching to room temperature appears to be similar in all three experiments.

Experiment	Bainitic ferrite	Retained austenite	Fresh martensite
900-440	79 ± 1	20 ± 1	1 ± 1
900-410	83 ± 1	16 ± 1	1 ± 1
900-380	88 ± 2	11 ± 2	1 ± 1

Table 6: Fractions of bainitic ferrite, retained austenite and fresh martensite in wt.% present after quenching to room temperature (experiments with fine PAGs).

4.2.3 Evolution of bainitic ferrite and austenite lattice parameters

Figure 30 presents the evolution of the lattice parameter of bainitic ferrite during the phase transformation in experiments with fine prior austenite grains. Two distinct evolution stages of the bainitic ferrite lattice parameter can be detected when the fluctuations at the beginning of the phase transformation are neglected. During the first stage, the lattice parameter of bainitic ferrite increases. Depending on the isothermal holding temperature, the initial increase lasts approximately 60 to 90 seconds. After reaching its maximum, the bainitic ferrite lattice parameter gradually decreases until the end of the experiment. The explanation for the development of the two distinct evolution stages provided for the experiments with coarse PAGs also applies to the experiments with fine PAGs.

Figure 31 presents the evolution of the average lattice parameter of austenite during the phase transformation. Figure 31a exhibits the average austenite lattice parameter as a function of time.

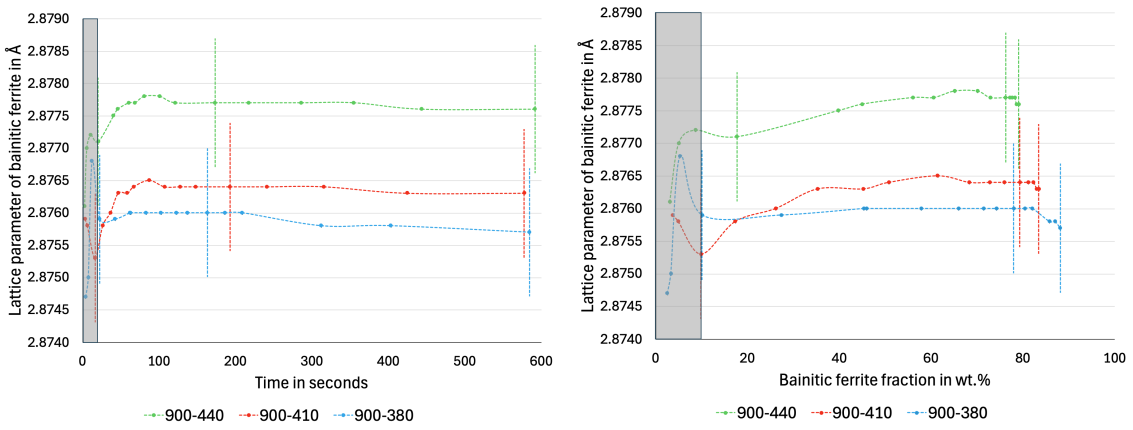

(a) Lattice parameter vs. time.

(b) Lattice parameter vs. bainitic ferrite fraction.

Figure 30: Evolution of the lattice parameter of the bainitic ferrite during the phase transformation (experiments with fine PAGs).

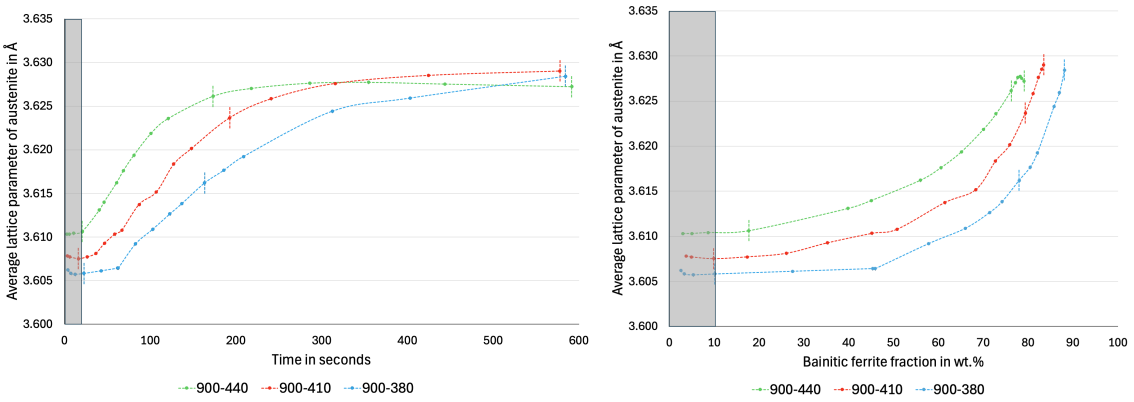

(a) Lattice parameter vs. time.

(b) Lattice parameter vs. bainitic ferrite fraction.

Figure 31: Evolution of the average lattice parameter of the remaining austenite during the phase transformation (experiments with fine PAGs).

The curves show that the higher the transformation temperature, the faster the initial increase in the average austenite lattice parameter. However, the slope of higher transformation temperatures flattens faster. The observed trend may be a results of the effect of the transformation temperature on the carbon partitioning process, as it is explained for the experiments with coarse PAGs.

4.2.4 Evolution of microstrain in bainitic ferrite

Figure 32 plots the microstrain present in bainitic ferrite as a function of time. The microstrain is higher at lower transformation temperatures, indicating the presence of a higher number of dislocations. Furthermore, it can be observed that the decrease in the microstrain with time is more pronounced at higher transformation temperatures, which may be related to an enhanced recovery of dislocations at higher transformation temperatures.

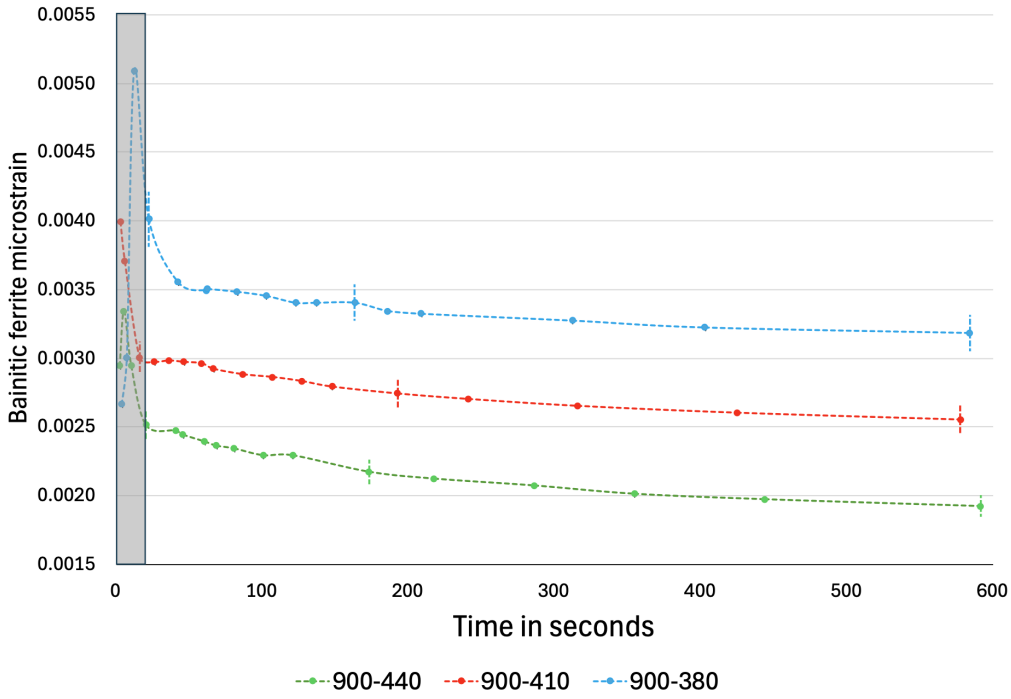

Figure 32: Microstrain in bainitic ferrite vs. time (experiments with fine PAGs).

4.2.5 Interrupted quenching experiments

Figure 33 presents optical microscopy images of interrupted quenching experiments performed on specimens with a fine PAG structure. Two specimens that were isothermally transformed at 440 °C and 360 °C for 15 seconds were selected to be presented. Figure 33a and Figure 33b show images of experiment IQ-900-440-15. Broad and thin sheaves, as well as concentrated grain boundary nucleation can be observed. Figure 33c and Figure 33d show optical microscopy images of experiment IQ-900-360-15. Thin and relatively broad sheaves are visible in both images. The nature of the microstructure makes it difficult to detect areas of concentrated grain boundary nucleation.

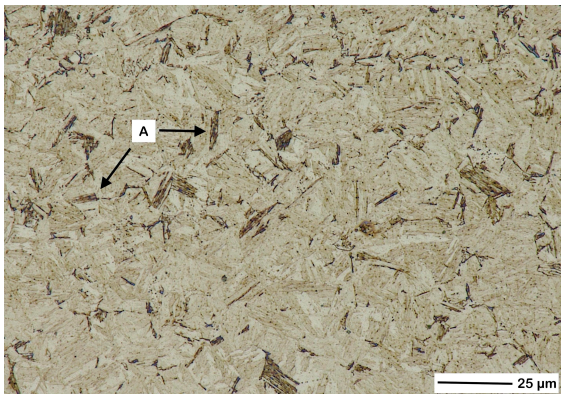

(a) IQ-900-440-15

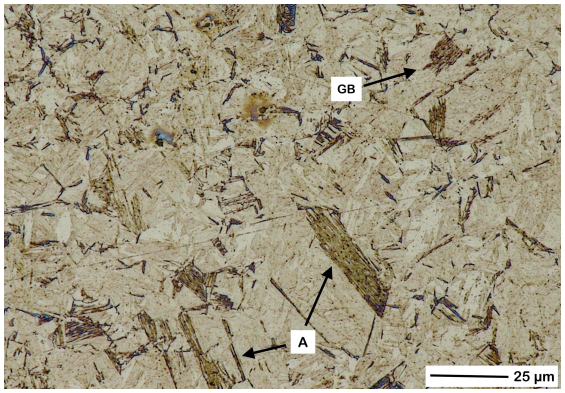

(b) IQ-900-440-15

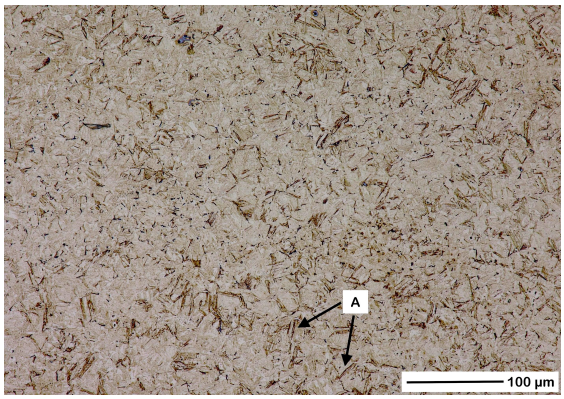

(c) IQ-900-360-15

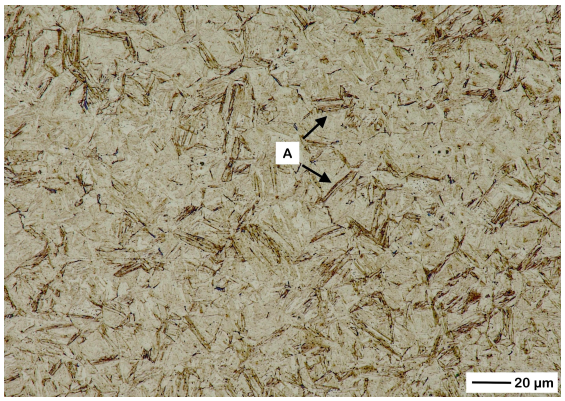

(d) IQ-900-360-15

Figure 33: Optical microscopy images of interrupted quenching tests. GB: bainitic ferrite that primarily formed at grain boundaries. A: longer bainitic ferrite sheaves that consist of many successive autocatalytic nucleation events.

5 Discussion

5.1 Comparison of experiments with different prior austenite grain sizes

5.1.1 Microstructure and interrupted quenching experiments

The optical microscopy images of the experiments with coarse and fine prior austenite grains, presented in Figure 19 and Figure 27, show that the latter forms a finer microstructure. The smaller PAG size restricts bainitic ferrite sheaf growth and hence sheaves are smaller in the second experiment group. Furthermore, the retained austenite blocks in the microstructure with fine prior austenite grains are smaller in size.

Figure 25 and Figure 33, presenting the morphology of bainitic ferrite formed in the interrupted quenching experiments, show that IQ-1100-440-40, IQ-1100-360-25 and IQ-900-440-15 consist of both types of morphologies, large sheaves and bainitic ferrite primarily grown along the grain boundary. The microstructure of IQ-1100-380-30 and IQ-900-360-15 exhibits many thin sheaves, as well as some broader sheaves. It was difficult to distinguish between concentrated grain boundary nucleation and broader sheaves in the microstructures formed at 380 °C and 360 °C. In the interrupted quenching experiments, the length of a sheaf always depends on the point in time at which the sheaf has nucleated relative to time of the quench. Broader sheaves, as indicated in Figure 25b, Figure 25f or in Figure 33b, may have started to grow primarily along grain boundaries and continued to grow longer by autocatalytic nucleation after some time. Furthermore, the sheaf morphology observed also depends on its orientation relative to the plane investigated by microscopy. Bainitic ferrite detected to have grown along a grain boundary may have have grown larger already, but could have an orientation other than parallel to the plane investigated by optical microscopy. Therefore, it is not possible to make a conclusive statement on the effect of the transformation temperature on the prevalent nucleation site, based on the observations made in the interrupted quenching experiments.

5.1.2 Evolution of phase fractions

Figure 34 plots the bainitic ferrite fraction formed as a function of time for both experiment groups. The solid curves refer to the experiments with a coarse prior austenite grain structure and the dashed curves refer to the experiments with a fine prior austenite grain structure. The experiments with isothermal holding at 440 °C exhibit a similar fraction of bainitic ferrite formed at the end of the phase transformation. For experiments with isothermal transformation temperatures at 410 °C and 380 °C, the experiments with a coarser prior austenite grain structure appear to have formed a slightly higher fraction of bainitic ferrite. However, the observed differences are in the experimental error range, indicating that the PAG size may have no significant effect on

the bainitic ferrite fraction formed after 600 seconds of holding at the isothermal transformation temperature in the experiments performed at DESY.

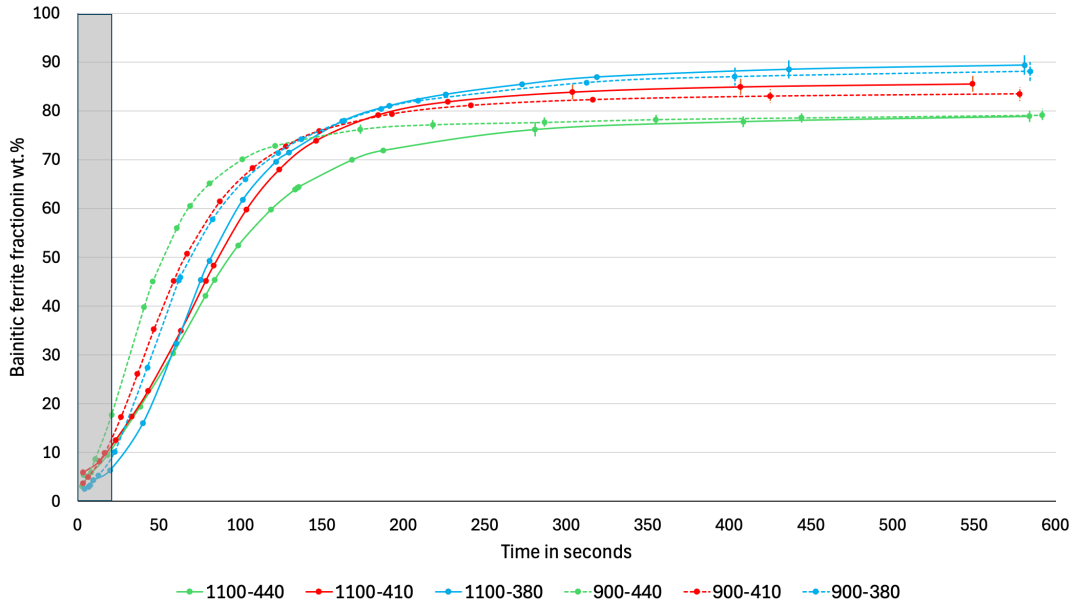

Figure 34: Bainitic ferrite fraction in wt.% vs. time (experiments with different PAG sizes).

Before discussing the effect of the isothermal transformation temperature and prior austenite grain size on the phase transformation kinetics of bainite, the presence of ferrite detected in 5 of the 6 experiments has to be considered. Visual diffractogram analysis of XRD patterns recorded at the end of the austenitization treatments showed that 900-440 was the only experiment without ferrite or, if present, with a significantly smaller fraction of ferrite remaining after the austenitization treatment. Studies have shown that the presence of a small fraction of ferrite prior to the onset of bainite formation can accelerate the phase transformation kinetics of bainite by the increased number of potential nucleation sites due to additional interfaces between ferrite and austenite [37, 55]. Zhu et al. [56] found that 51 wt.% of ferrite formed prior to bainite formation has a decelerating effect on the phase transformation kinetics. Different mechanism have been observed to cause the deceleration. On the one hand, the formation of such a high fraction of ferrite causes the carbon concentration in austenite to increase, which results in a decrease of the driving force for bainite formation. Furthermore, elevated concentrations of carbon and manganese were detected in the vicinity of ferrite-austenite interfaces resulting from partitioning during ferrite formation, which again decreases the driving force for bainite formation at the newly formed interfaces. Ravi et al. [37], states that ferrite fractions below 5 wt.% do not significantly affect the global carbon concentration in the austenite and hence the driving force for bainitic ferrite formation.

Considering that 900-440 transforms the fastest of all experiments, an acceleration of the phase transformation kinetics of bainite by the ferrite detected in the other experiments may not be significant. This may be explained by the relatively small fraction of ferrite remaining after the austenitization treatment. Figure 35 compares an XRD pattern recorded at the end of the aus-

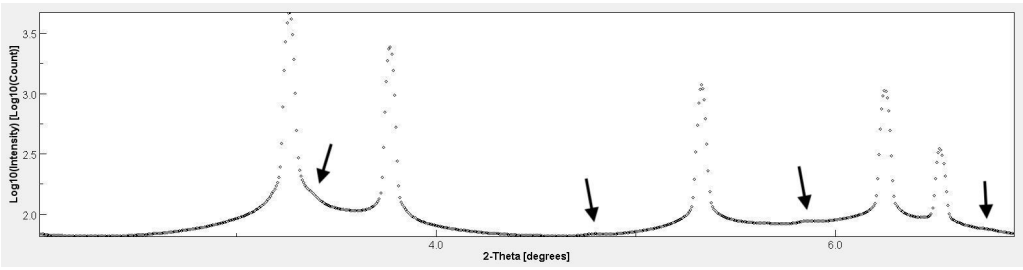

(a) Arrows point on ferrite peaks detected at the end of the austenitization treatment in 900-410.

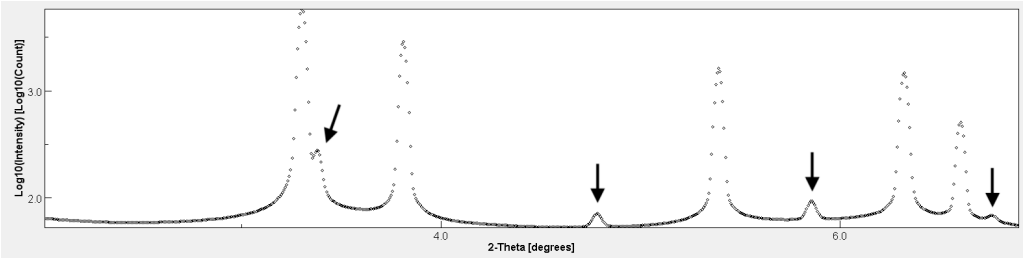

(b) Arrows point on bainitic ferrite peaks corresponding to a fraction of 2.5 wt.% in 900-380.

Figure 35: Comparison of peak dimensions of ferrite present after austenitization and bainitic ferrite formed at the beginning of the phase transformation.

tenitization treatment of 900-410 with an XRD pattern recorded at the beginning of the bainitc phase transformation in 900-380. It can be observed that the ferrite peaks at the end of the austenitization are significantly smaller than the peaks presented in Figure 35b, which correspond to approximately 2.5 wt.% of bainitic ferrite. Therefore, it can be assumed that the ferrite fraction remaining after austenitization is significantly smaller than 2.5 wt.%. A decelerating effect caused by the presence of ferrite, as it was detected by Zhu et al. [56], is rather unlikely, due to the significantly lower fraction of ferrite detected in the present study. Therefore, the ferrite remaining at the end of the austenitization treatment in 5 of the 6 experiments is assumed to have no significant effect on the phase transformation kinetics of bainite in this study and thus will be neglected in the following interpretations of the results. However, it should be noted that the studies discussed investigated the effect of ferrite formed in a heat treatment prior to bainite formation, while the ferrite present in this study remained after austenitization. Thus, they may have different effects on the phase transformation kinetics of bainite.

When focusing on the beginning of the phase transformation, the simultaneous effect of the isothermal transformation temperature and prior austenite grain size on the phase transformation kinetics becomes apparent. In general, the experiments with a fine PAG structure transform faster than the experiments with a coarse PAG structure. However, it can be observed that the effect of the isothermal transformation temperature on the transformation kinetics is reversed for the two experiment groups. While for the experiments with fine prior austenite grains, 900-440 transforms the fastest, for experiments with coarse prior austenite grains, 1100-440 transforms the slowest. The reversed effect of the transformation temperature on the phase transformation kinetics of the two experiment groups causes the difference in the phase transformation kinetics of coarse and fine

PAGs at the same transformation temperature to decrease. To make this difference quantifiable, the time required to form 45 wt.% of bainitic ferrite was determined for each experimental condition. The parameter is denoted as $t_{45wt.\%}$ and is provided in Table 7. It can be used to calculate the difference in time required to form 45 wt.% of bainitic ferrite in experiments with fine and coarse PAGs at the same isothermal transformation temperature. The difference is denoted as Δt in Table 7 and can be used as a parameter to compare the difference in the phase transformation kinetics of fine and coarse PAGs at the three different transformation temperatures. Table 7 shows that Δt decreases with decreasing transformation temperatures. This indicates that the difference in the phase transformation kinetics in the experiments with coarse and fine PAG sizes at the same transformation temperature decreases, as the transformation temperature decreases.

Transformation temperature	$t_{45wt.\%}$ fine PAG size	$t_{45wt.\%}$ coarse PAG size	Δt
440 °C	46 s	84 s	38 s
410 °C	59 s	78.5 s	19.5 s
380 °C	62 s	75.5 s	13.5 s

Table 7: Time required to form 45 wt.% of bainitic ferrite, $t_{45wt.\%}$, in experiments with coarse and fine prior austenite grains and the difference in $t_{45wt.\%}$ for coarse and fine prior austenite grains at the same transformation temperature, Δt.

The observations may be explained by the effect of the transformation temperature on the difference in activation energy for grain boundary and autocatalytic nucleation, ΔQ. The fraction of potential nucleation sites for grain boundary and autocatalytic nucleation differs significantly for the two experiment groups. While the experiments with fine PAGs provide a higher number of potential nucleation sites at grain boundaries, the experiments with coarse PAGs provide a larger grain area and hence more space for sheaf growth. Therefore, the experiments with coarse PAGs provide a higher number of potential nucleation sites for autocatalytic nucleation throughout the phase transformation process. Figure 34 and Table 7 show that at 440 °C, the difference in the phase transformation kinetics between the two PAG sizes is the highest. 900-440 transforms significantly faster than 1100-440, which indicates that grain boundary nucleation may be faster than sheaf growth. Therefore, the value of ΔQ can be expected to be low at 440 °C. In contrast, the difference in the phase transformation kinetics between 900-380 and 1100-380 is much smaller, which indicates that sheaf growth is accelerated by decreasing the transformation temperature and thus a higher ΔQ is present at 380 °C. Therefore, it may be deduced that ΔQ increases with decreasing transformation temperatures causing autocatalysis to become more prevalent and hence to accelerate the phase transformation kinetics for the experiments with a coarse PAG structure and to decelerate the phase transformation kinetics for experiments with a fine PAG structure. The effect of the transformation temperature on ΔQ will be further discussed in section 5.2.

When comparing the phase fractions of the two experiment groups, presented in Figure 36, it can be observed that the fraction of retained austenite present after isothermal holding for 600 seconds at 440 °C and 410 °C is higher in experiments with fine prior austenite grains. The difference

observed for the experiments performed at 380 °C appears to be insignificant. The fraction of fresh martensite formed during quenching to room temperature after isothermal bainite formation at 440 °C is higher in the experiment with coarse PAGs. In contrast, the experiments with coarse and fine prior austenite grains performed at 410 °C and 380 °C do not show significant differences in their fresh martensite fractions. The observations can be explained by the homogenization process of carbon. Research on the effect of the PAG size on the carbon partitioning and homogenization process in martensitic Q&P steels has shown that a fine PAG structure promotes a more efficient partitioning process. Celada-Casero et al. [57] demonstrated that a fine PAG structure results in the development of smaller and more homogeneously distributed martensite and austenite blocks during the first quench. Austenite blocks of smaller sizes are homogenized faster, due to smaller diffusion distances. A similar effect may be expected in the present study. The comparison of optical microscopy images showed the presence of a finer microstructure with smaller austenite blocks in the experiments with fine PAGs. Larger austenite blocks result in longer distances carbon has to diffuse to reach a homogeneous carbon concentration and hence the homogenization process of experiments with coarse PAGs may be prolonged. This explains the higher fraction of fresh martensite observed in 1100-440 compared to 900-440. Figure 19 shows that the size and number of austenite blocks decreases as the transformation temperature decreases, which is a result of the higher fraction of bainitic ferrite formed at lower transformation temperatures. Therefore, diffusion distances for carbon are reduced as the transformation temperature is decreased, which may result in a faster homogenization process, despite the lower diffusivity at lower transformation temperature. This could explain why the fraction of fresh martensite is similar for both PAG sizes in the experiments with bainite formation at 410 °C and 380 °C degrees.

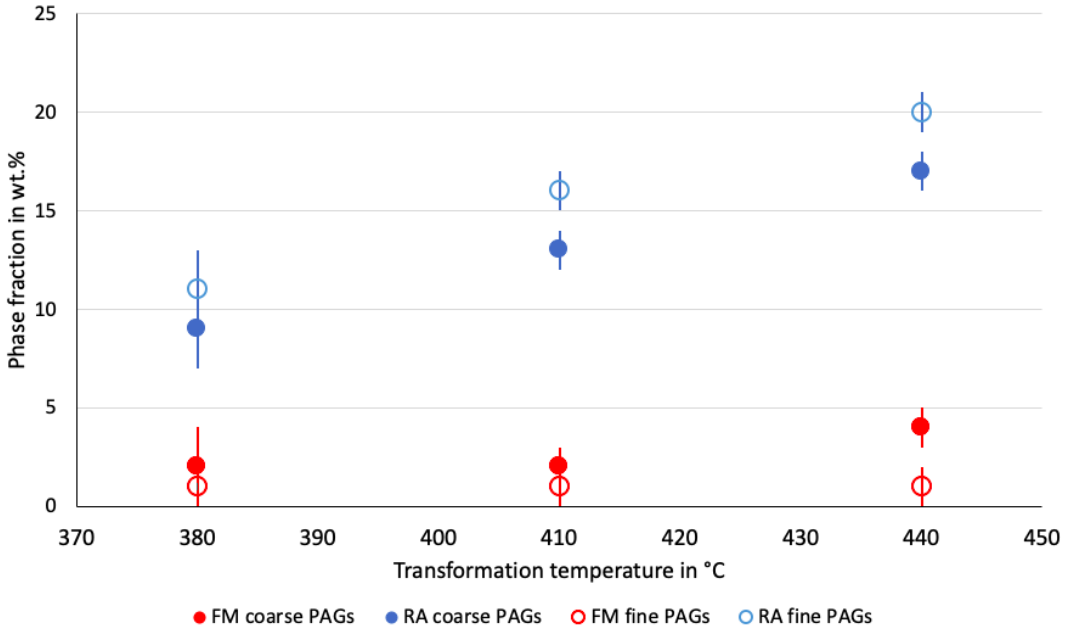

Figure 36: Fractions of retained austenite and fresh martensite in wt.% present after quenching to room temperature. FM: fresh martensite and RA: retained austenite.

5.1.3 Evolution of bainitic ferrite and austenite lattice parameters

Figure 37 presents the evolution of the lattice parameter of bainitic ferrite as a function of time for experiments with fine and coarse prior austenite grains. The error bars indicate that the differences in the lattice parameters between the two experiment groups are relatively small and thus are in the experimental error range. Comparing the experiments with isothermal holdings at 440 °C and 410 °C, the lattice parameters of the experiments with a finer PAG structure are supposed to be smaller, while the opposite is found for experiments with isothermal holding at 380 °C. This inconsistency is another indicator that the observed differences may arise from the experimental error.

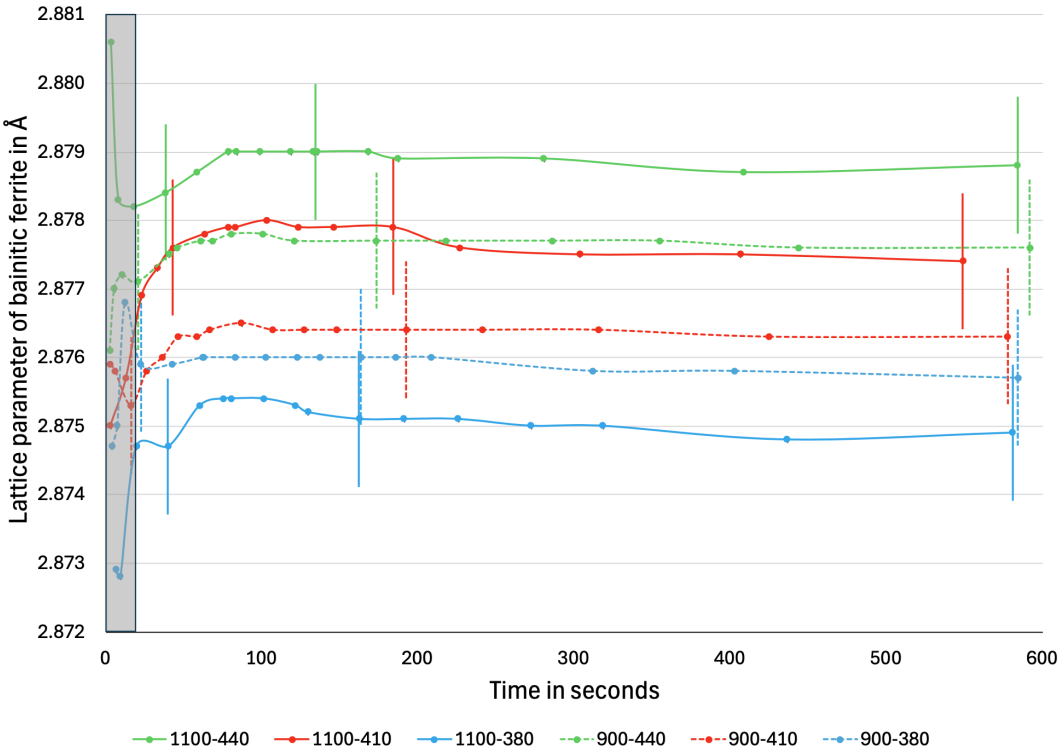

Figure 37: Bainitic ferrite lattice parameter vs. time (experiments with different PAG sizes).

Figure 38 presents the average austenite lattice parameter as a function of time for experiments with fine and coarse prior austenite grains. The error bars show that the differences observed for the two experiment groups are significant. During isothermal holding at 440 °C and 380 °C the lattice parameter of austenite appears to be larger in experiments with fine PAGs. Experiments 1100-410 and 900-410 exhibit differences within the experimental error range. However, the differences observed in the experiments with isothermal holding at 440 °C and 380 °C could result from different phase fractions rather than from a difference in the carbon enrichment process. Therefore, the average austenite lattice parameter was plotted as a function of the bainitic ferrite fraction and is presented in Figure 39a. To eliminate the initial difference in the average austenite lattice parameters, the change of the austenite lattice parameter relative to its starting value is plotted as a function of bainitic ferrite fraction in Figure 39b. The relative change exhibits how much

the average austenite lattice parameter increases during the process of the phase transformation and makes it possible to compare all six experimental conditions. The estimated error is $\pm$ 1.7 $\times$ 10^{-4} Å, which is the experimental error remaining after instrument calibration. The error bars are approximately as large as the data points, which is the reason why they are not visible in plot Figure 39b. However, it should be noted that there may be an additional error in the starting value of the average austenite lattice parameter resulting from the effect of large prior austenite grains on the FCC peak shapes in 1D XRD patterns.

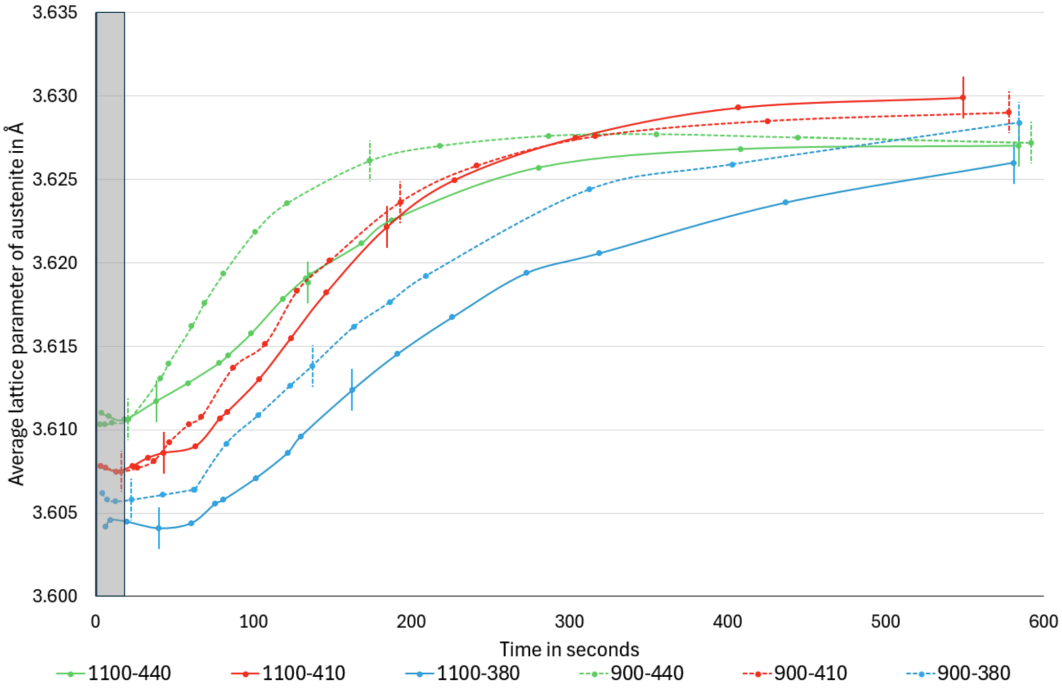

Figure 38: Average austenite lattice parameter vs. time (experiments with different PAG sizes).

Figure 39b shows that the relative change of the average austenite lattice parameter at the same fraction of bainitic ferrite formed is higher at higher transformation temperatures. The observation can be explained by the higher carbon diffusivity at higher transformation temperatures, which causes a faster carbon enrichment process of the austenite [22, 50]. Furthermore, a potential transition from upper to lower bainite was observed in the transformation temperature range investigated, which further slows down the carbon partitioning process and even decreases the amount of carbon that partitions into austenite as the transformation temperature is decreased. The relative change of the average austenite lattice parameter at the same phase fraction of bainitic ferrite formed appears to be higher for the experiment group with a fine prior austenite grain size. The difference is relatively small and depends on the starting value relative to which the change is calculated. However, the observation is consistent across all transformation temperatures and seems to be significant considering the experimental error range. A possible explanation for this observation will be discussed in the following section.

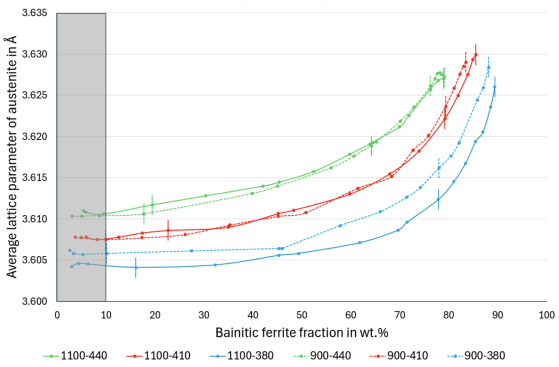

(a) Average austenite lattice parameter vs. bainitic ferrite fraction.

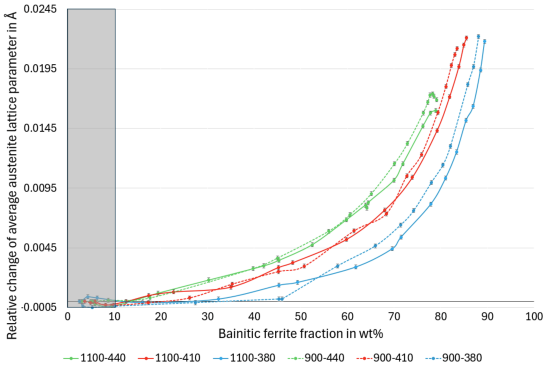

(b) Relative change of average austenite lattice parameter vs. bainitic ferrite fraction.

Figure 39: Evolution of the average lattice parameter of remaining austenite vs. bainitic ferrite fraction (experiments with different PAG sizes).

5.1.4 Evolution of microstrain in bainitic ferrite

Figure 40 plots the microstrain present in bainitic ferrite as a function of time for both experiment groups. After approximately 80 seconds of holding the curves of the same transformation temperature follow a similar trend, which is a steady decrease of the microstrain until the end of the holding. Furthermore, the plot shows that the experiments with finer prior austenite grains develop a lower microstain in the bainitic ferrite, which can be related to a lower dislocation density.

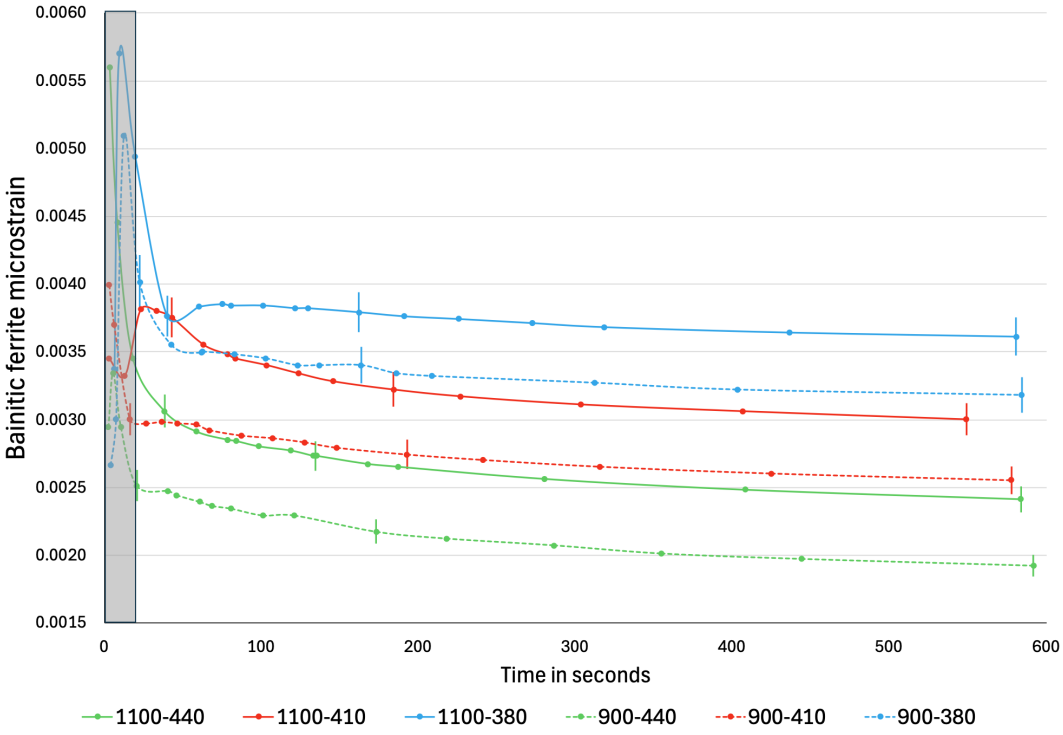

Figure 40: Microstrain in bainitic ferrite vs. time (experiments with different PAG sizes).

As explained in the previous section, the dislocation density in bainitic ferrite is related to the strength of bainitic ferrite and austenite. Therefore, the dislocation density is expected to increase

with an increase in yield strength of the phases, which is consistent with the decreasing dislocation density observed for increasing transformation temperatures [6, 19, 53]. Lin et al. [6] observed that the dislocation density in bainitic ferrite increased with increasing Si alloy content. The increase in dislocation density was related to the strengthening of austenite by solid solution hardening provided by Si.

He et al. [53] investigated the relation of the dislocation density present in the bainitic ferrite with the bainitic ferrite sub-unit size and observed a decrease in sub-unit thickness with an increase in dislocation density. The observation was explained by the fact that an increase in austenite strength constrains bainitic ferrite growth more effectively and hence results in a smaller sub-unit thickness. According to this relation, the sub-unit thickness of the experiments with coarser PAGs would be smaller. Several models relate the austenite yield strength to the sub-unit thickness and predict a decreasing sub-unit thickness with increasing austenite yield strength [58, 59, 60]. According to the Hall-Patch effect, which is considered in the model developed by van Bohemen [60] for instance, the austenite yield strength is expected to increase with decreasing prior austenite grain size [61]. Thus a smaller sub-unit thickness would be expected for a smaller prior austenite grain size. However, there are studies that found a decreasing sub-unit thickness with increasing prior austenite grain size [44, 62], as it may be the case for the steel in the present study. In general, the relation between the sub-unit thickness and PAG size is complex and depends on more parameters than the austenite yield strength, such as the driving force for bainitic ferrite formation or dynamic recovery [24].

A higher dislocation density in bainitic ferrite observed in the experiments with coarse prior austenite grains could explain the differences observed for the relative change the average austenite lattice parameter. Studies on martensitic Q&P steels have shown that the high number of defects, such as dislocations and interfaces, in martensite significantly slows down the carbon the partitioning process [63, 64]. Therefore, it may be expected that the higher dislocation density, as well as the higher number of interfaces due to a smaller sub-unit size, provide more sites to trap carbon and hence delay the carbon partitioning process in experiments with a coarse prior austenite grain structure in comparison to the experiments with a fine prior austenite grain structure.

5.2 Simulations to determine ΔQ

Simulations using the model developed by dos Santos Avila et al. [24] were used to obtain a detailed understanding of the effect of the combination of prior austenite grain size and isothermal transformation temperature on ΔQ. The model requires the PAG size d_γ, the sub-unit thickness u', the transformation temperature T, the data points of the bainitic ferrite vs. time curve and approximate starting values of the activation energies for grain boundary Q_{GB} and autocatalytic nucleation Q_A, as data input. The initial values of Q_{GB} and Q_A were determined manually using visual fitting of the bainitic ferrite vs. time curves provided by the model.

To run the simulations, the sub-unit thickness needs to be determined. On the basis of the microstrain results, the sub-unit thickness is expected to decrease with increasing PAG size. However, the majority of the models available for sub-unit thickness prediction do not consider the effect of the prior austenite grain size or predict a decreasing sub-unit thickness with PAG refinement [58, 59, 60]. Therefore, Equation 8 developed by Parker [65], which solely considers the effect of transformation temperature on sub-unit thickness, was selected to determine the sub-unit thickness at the three transformation temperatures.

$$u' = 0.2\frac{T - 528}{150} \tag{8}$$

with T as the transformation temperature in K and u' as the sub-unit thickness in µm.

Simulations to determine ΔQ could not be performed individually for all 6 experiments. The presence of ferrite prior to the onset of the phase transformation to bainite caused errors in the fitting of the bainitic ferrite vs. time curves of experiments with coarse PAGs. A detailed explanation of the fitting error is provided in Appendix H. Therefore, the curves of the experiments with coarse and fine PAGs at the same transformation temperature were fitted simultaneously, to understand the general effect of the transformation temperature on ΔQ. The sub-unit thicknesses, the initial and final values of Q_{GB} and Q_A, and the values determined for ΔQ are given in Table 8.

Transformation temperature in °C	u' in nm	Initial Q_{GB} in kJ/mol	Initial Q_A kJ/mol	Final Q_{GB} kJ/mol	Final Q_A kJ/mol	ΔQ kJ/mol
440	247	251.8	247.1	250.7	248	2.7
410	207	241.2	232.7	240.9	233.2	7.7
380	167	229.1	219.5	229.2	219.3	9.9

Table 8: Sub-unit thickness, u', initial and final activation energy for grain boundary nucleation, Q_{GB}, initial and final activation energy for autocatalytic nucleation, Q_A, and difference in activation energies for gain boundary and autocatalytic nucleation, ΔQ.

Figure 41 plots ΔQ determined at the transformation temperatures 440 °C, 410 °C and 380 °C. The error bars are based on the error calculated by the model. According to the calculations of the model, a clear increase of ΔQ with decreasing isothermal transformation temperatures is visible. Simulations of dos Santos Avila et al. [24] showed that an acceleration of the phase transformation kinetics of bainite by PAG refinement can expected when ΔQ is as low as approximately 5 kJ/mol. In contrast, an acceleration of the phase transformation kinetics of bainite by PAG coarsening can be expected when ΔQ takes higher values, such as 15 kJ/mol. This explains the reversed effect of the transformation temperature on the phase transformation kinetics of the experiments with coarse and fine prior austenite grains. At 440 °C, with ΔQ being approximately 2.7 kJ/mol, nucleation at grain boundaries is expected to be prevalent. 900-440 provides more potential nucleation sites at prior grain boundaries, which is the reason why it transforms significantly faster than 1100-440. As the transformation temperature is reduced, ΔQ increases and takes an intermediate value

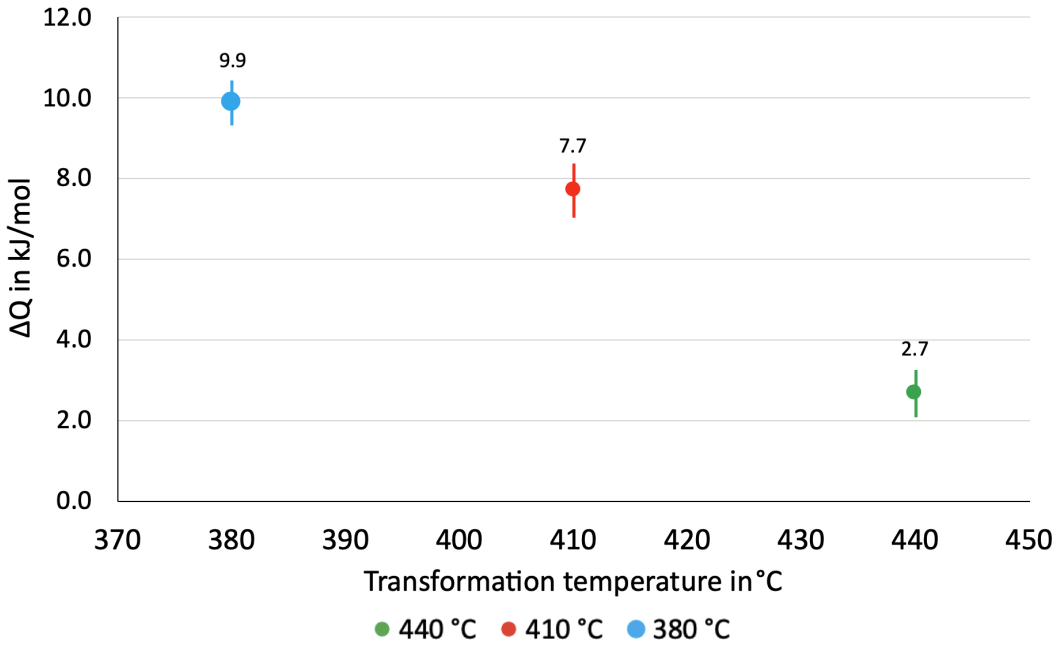

Figure 41: ΔQ at isothermal transformation temperatures of 440 °C, 410 °C and 380 °C determined by simulations using the model developed by dos Santos Avila et al. [24].

of approximately 9.9 kJ/mol at 380 °C. The increase in ΔQ indicates that the transformation by autocatalysis becomes more prevalent as the transformation temperature decreases. The larger the grain size, the more potential nucleation sites for autocatalytic nucleation are available because sheaves can grow larger. Therefore, the phase transformation kinetics of experiments with coarse PAGs are accelerated, while the kinetics of experiments with fine PAGs are decelerated, as the transformation temperature is decreased. However, ΔQ stays well below 15 kJ/mol at 380 °C, which explains why 900-380 still exhibits faster phase transformation kinetics than 1100-380.

The transformation temperature determines the undercooling with respect to T_h, which is the highest temperature at which ferrite can form by a displacive phase transformation mechanism [66]. Ravi et al. [15] observed the activation energy for grain boundary and autocatalytic nucleation to decrease linearly with increasing undercooling. This linear dependence of the activation energy on undercooling indicates that bainite nucleation involves thermally activated migration of dislocations [15, 67]. Based on the isothermal martensite nucleation theory, Bhadeshia [66] suggested that the nucleation of bainite occurs by the dissociation of dislocations that already exist in the matrix of the steel. Differences in the activation energies at the two types of nucleation sites are explained to arise from the different nature of the previously existing and the created interfaces, as well as the different matrices surrounding the nucleus during its formation [15]. However, when comparing the observed effect of the transformation temperature on ΔQ with the results of other studies, it is obvious that the direct influence of the transformation temperature on the activation energies at both types of nucleation sites is not sufficient to generally explain the effect of the PAG size on the phase transformation kinetics.

Hasan et al. [38] observed PAG coarsening to accelerate the phase transformation kinetics of bainite formed at 420 °C, when investigating a 0.25C-1.6Mn-1.25Si-1Cr-0.3Mo steel with prior austenite grain sizes varying between 16 µm and 157 µm. Jiang et al. [68] investigated the bainitic phase transformation of a 0.8C-1.5Si-2.0Mn-1.0Cr-0.24Mo-1.0Al-1.6Co steel at 250 °C and observed an acceleration of the phase transformation kinetics by PAG refinement from 53 µm to 3 µm. Furthermore, Barford and Owen [39] performed isothermal transformations with a 1.4C-1Mn steel at 280 °C and 370 °C and found an acceleration by PAG refinement in both cases. The results of the three studies presented do not confirm a potential increase of ΔQ with decreasing transformation temperatures. This observation may be explained by the different steel compositions, significant differences in the PAG size ranges investigated or varying austenitization procedure, for instance. The effect of the steel composition on ΔQ was investigated by Matsuzaki and Bhadeshia [42], when studying the effect of the PAG size on the phase transformation kinetics of a 0.12C-2.96Mn-2.03Si steel transformed at 450 °C and a 0.96C-0.38Mn-0.21Si-1.26Cr transformed at 435 °C. Whereas the high-carbon steel showed an acceleration of the phase transformation kinetics by PAG refinement, the low-carbon steel showed an acceleration of the phase transformation kinetics by PAG coarsening. The researchers concluded that the steel composition affects the preference for a specific nucleation site, causing the phase transformation kinetics of the high-carbon steel to be determined by grain boundary nucleation, while the phase transformation kinetics of the low-carbon steel are determined by sheaf growth. However, by influencing processes, such as carbon partitioning or element segregation to interfaces, varying transformation temperatures can affect the steel composition locally, resulting in a local change in the driving force for bainite formation and hence a change in ΔQ.

One of the processes that affect the steel composition locally is carbon partitioning from bainitic ferrite into the remaining austenite. The difference in carbon diffusivity in BCC lattices compared to FCC lattices causes a temporary accumulation of carbon in austenite in the vicinity of sub-units [6, 69]. The build-up of carbon at the α/γ interface results in a temporary decrease in driving force for bainitic ferrite formation at the tip of the sub-unit and may event inhibit the nucleation of new sub-units by autocatalysis at this nucleation site. This effect is supposed to be more pronounced in steels with a higher carbon content [21]. However, the accumulation of carbon at and in the vicinity of α/γ interfaces is also affected by the transformation temperature. Higher transformation temperatures facilitate a faster carbon partitioning process, as well as a faster carbon redistribution within the steel. At lower transformation temperatures, the process of carbon partitioning is slower and the redistribution of carbon is sluggish. This may cause the accumulation of carbon in the vicinity of α/γ interfaces to be more severe, as well as to be present for longer times. Therefore, a decrease in driving force for autocatalytic nucleation and hence a smaller value of ΔQ could be expected at lower transformation temperatures. However, the transformation temperature does not only affect carbon diffusivity but also the dislocation density in bainitic ferrite, as well as carbide precipitation. As observed in the previous section, the increase

in dislocations further slows down the carbon partitioning process. Furthermore, decreasing the transformation temperature can lead to the transition from upper to lower bainite, as it is the case for the transformation temperature range investigated in the present study. In lower bainite carbides precipitate within the bainitic ferrite and thus the total carbon content available for carbon partitioning into the remaining austenite decreases. This may cause the accumulation of carbon at the α/γ interface to be less severe than at higher transformation temperatures, which would explain an increase in ΔQ with decreasing transformation temperatures, as it has been observed in this study. However, this indirect effect of the transformation temperature on ΔQ is dependent on the steel composition, which influences processes such as the transition from upper to lower bainite. Therefore, the effect of the transformation temperature on ΔQ is complex, which may be one of the reasons why the results of different studies appear to be contradicting.

Another example of local composition changes that are affected by temperature is the segregation of Mn to PAG boundaries. Lui and Zhang [70] detected Mn segregation to occur during the isothermal bainite formation of a Fe-0.37C-2.23Si-2.29Mn steel at 475 °C. Furthermore, they observed that Mn segregation decelerates the bainite formation kinetics by restraining the nucleation of bainitic ferrite. The segregation of Mn to PAGs causes a local decrease in driving force for bainite formation, which would lead to an increase in ΔQ and hence sheaf growth would determine the phase transformation kinetics. Furthermore, they observed that Mn segregation resulting from the austenitization treatment is decreased by decreasing the austenitization temperature. Lower austenitization temperatures result in smaller prior austenite grains, indicating that the local decrease in driving force resulting from Mn segregation during austenitization may be less pronounced in fine-grained PAG structures. Mn segregation was observed to increase with increasing Mn concentrations, as well as in the presence of Si. However, the segregation of substitutional alloying elements is often not investigated in studies on the effect of the PAG size on the phase transformation kinetics of bainite. To avoid Mn segregation to prior austenite grain boundaries, many studies performed a homogenization treatment before conducting the experiments [22, 37, 38, 42]. In their study on the effect of ferrite formation on the phase transformation kinetics of bainite, Ravi et al. [37] used APT to investigate local composition changes at the prior austenite grain boundaries. The researchers did not find signs of Mn segregation resulting from austenitization or previous isothermal treatments for ferrite formation.

Finally, there is the effect of the isothermal transformation temperature, as well as the effect of prior austenite grain size on sub-unit volume. Simulations of dos Santos Avila et al. [24] have shown that a change in sub-unit thickness can reverse the observed effect of the PAG size on the phase transformation kinetics of bainite at a constant ΔQ. The sub-unit volume determines the amount of austenite transformed to bainitic ferrite per nucleation even and hence its increase would accelerate the process of the phase transformation. However, the relationship between PAG size and sub-unit thickness is not fully understood, making it even more complex to understand the effect of the prior austenite grain size on the bainite formation kinetics.

6 Limitations

While working on the master's thesis, the following challenges that limited the research arose:

1. The relatively low fraction of ferrite detected at the end of the austenitization, as well as comparisons with other studies, have led to the assumption that the ferrite did not effect the results of the study. However, a potential effect of the ferrite on the phase transformation kinetics of bainite cannot be completely ruled out.

2. The presence of ferrite at the beginning of the phase transformation to bainite limited the simulations to simultaneous fitting of the bainitic ferrite fraction vs. time curves of experiments with fine and coarse prior austenite grains at the same transformation temperature. Therefore, only the effect of the isothermal transformation temperature on ΔQ, and not the potential influence of the PAG size itself, could be determined by the use of the simulations.

3. The temperature fluctuations, as well as the effect of the spotty diffraction rings on the austenite peak shapes at the beginning of the phase transformation, affect the values of phase fractions, lattice parameters and microstrains determined from XRD patterns recorded during that time frame. These effects also influence the accuracy of calculations based on these data, such as the relative change of the average austenite lattice parameter.

4. The ferrite and carbide fractions could not be determined by Rietveld refinement, due to their relatively small diffraction peaks. Comparison of their peak dimensions with other diffraction patterns made it possible to get an idea of the order of magnitude of their phase fractions. Other methods, such as the direct comparison method, have to be applied to determine the exact carbide and ferrite fractions.

7 Conclusion and Recommendations

The aim of the master thesis was to investigate the effect of the prior austenite grain size and the isothermal transformation temperature on the phase transformation kinetics of bainite in a low-carbon high-silicon steel. In-situ synchrotron XRD was used to analyze the phase fractions, lattice parameters and microstrains of bainitic ferrite and austenite at the isothermal transformation temperatures 440 °C, 410 °C and 380 °C in two experiment groups with different prior austenite grain sizes. Microstructure investigations were used to explore the effects of the prior austenite grain size and the isothermal transformation temperature on the microstructure formed in the six experiments and on the bainitic ferrite sheaf morphology formed in the early stages of the phase transformation. The main findings on the effect of the PAG size and the isothermal transformation temperature on the microstructure are:

1. The experiments with fine prior austenite grains were observed to form a finer microstructure in comparison to the experiments with coarser prior austenite grains. Prior austenite grain boundaries restrict sheaf growth and thus smaller sheaves form in the experiments with fine PAGs. Furthermore, austenite blocks were observed to be smaller in the experiments with a fine PAG structure.

2. The ferrite detected at the end of the austenitization treatment in 5 of the 6 experiments was observed to have no significant effect on the phase transformation kinetics of bainite. This was explained by its relatively small fraction, which was estimated to be well below 2.5 wt.%.

3. The microstructures developed during the interrupted quenching experiments exhibited two different types of sheaf morphologies. One of them were bainitic ferrite sheaves that have grown relatively large by successive events of autocatalytic nucleation. Secondly, there was bainitic ferrite that has grown primarily along grain boundaries. At the lower transformation temperatures, it was oftentimes not possible to distinguish between broader sheaves and bainitic ferrite that grew along the grain boundaries. Furthermore, the observed sheaf morphology depends on its orientation to the plane investigated by microscopy and on the point in time at which the sheaf has nucleated relative to the time of quenching. Therefore, it was not possible to make a conclusive statement on the effect of the transformation temperature on the prevalent nucleation site, based on the observations made in the interrupted quenching experiments.

The main findings on the effect of the PAG size and the isothermal transformation temperature on the microstrain present in bainitic ferrite and the bainitic ferrite sub-unit size are:

1. It was observed that the microstrain developed in bainitic ferrite is higher in the experiments with coarse PAGs. The higher microstrain can be related to a higher dislocation density

present in the bainitic ferrite formed in the experiments with a coarse prior austenite grain structure.

2. The higher dislocation density indicates that the bainitic ferrite sub-units are smaller in the experiments with coarser prior austenite grains.

The main findings on the effect of the PAG size and the isothermal transformation temperature on the lattice parameters and the carbon partitioning process are:

1. At the same fraction of bainitic ferrite formed, the relative change of the average lattice parameter of austenite appears to be larger in experiments with finer prior austenite grains, which may be related to a higher carbon concentration and hence a faster carbon partitioning process in these experiments. The higher dislocation density and the higher number of interfaces due to a smaller sub-unit size provide more sites to trap carbon and hence could delay the carbon partitioning process in the experiments with a coarse prior austenite grain structure in comparison to the experiments with finer prior austenite grains.

The main findings on the effect of the PAG size and the isothermal transformation temperature on the phase transformation kinetics of bainite and ΔQ are:

1. At all transformation temperatures investigated, the experiments with fine PAGs exhibited faster phase transformation kinetics than the experiments with coarse PAGs.

2. The effect of the transformation temperature on the phase transformation kinetics of bainite was reversed for the two experiment groups. While the experiments with fine prior austenite grains showed a deceleration of the phase transformation kinetics with decreasing transformation temperatures, the experiments with coarse prior austenite grains were accelerated by decreasing the transformation temperature. The reverse dependence of the phase transformation kinetic on the isothermal transformation temperature causes the difference in the phase transformation kinetics between coarse and fine prior austenite grains at the same transformation temperature to decrease as the isothermal transformation temperature is decreased.

3. Simulations using the model developed by dos Santos Avila et al. [24] showed that ΔQ increases as the isothermal transformation temperature decreases. The increase in ΔQ indicates that transformation by autocatalysis becomes more prevalent as the transformation temperature decreases. While the experiments with a coarse PAG structure provide more potential nucleation sites for autocatalytic nucleation, the experiments with a fine PAG structure provide more nucleation sites for grain boundary nucleation, which explains the reverse effect of the transformation temperature on the phase transformation kinetics of the two experiment groups.

4. Comparisons of the results with other studies have shown that the direct effect of the transformation temperature on ΔQ is not sufficient to explain the effect of the prior austenite

grain size at a specific transformation temperature on the phase transformation kinetics of bainite. Indirect effects of the transformation temperature on processes, such as carbide precipitation, carbon partitioning or Mn segregation to interfaces, can cause local composition changes and hence can affect the difference in the activation energy for grain boundary and autocatalytic nucleation, ΔQ. These processes also depend on other factors, such as on the steel composition. Therefore, the effect of the transformation temperature on ΔQ is complex, which may be one of the reasons why the results of different studies appear to be contradicting.

5. The observed increase in ΔQ with decreasing isothermal transformation temperatures was explained by the transition from upper to lower bainite in the transformation temperature range investigated. Carbide precipitation from bainitic ferrite in lower bainite slows down the partitioning process and reduces the amount of carbon to partition into austenite. This may result in less carbon to accumulate at the α/γ interface in comparison to higher transformation temperatures at which the formation of upper bainite is expected. This could explain the increase of ΔQ with decreasing transformation temperatures.

Based on the work of the master thesis, recommendations for future research were defined. The following recommendations include further steps to extend the work of the master thesis, as well as research questions for new studies:

1. Investigating the correlation between the dislocation density in bainitic ferrite and the prior austenite grain size at different transformation temperatures using EBSD to verify the findings regarding the microstrain in the present work. Once the correlation is understood, the effect of the PAG size on the carbon partitioning process by its effect on the dislocation density can be studied.

2. Performing microstructure investigations to understand the dependence of sub-unit thickness on the prior austenite grain size and the isothermal transformation temperature. The determination of the precise sub-unit thickness at a specific PAG size and transformation temperature combination would make the output of the simulations to determine ΔQ more accurate.

3. Repeating the research with a 100 % austenitic microstructure at the end of the austenitization treatment to obtain insights on the effect of the detected ferrite on the phase transformation kinetics of bainite in the present study. Furthermore, this would allow to run simulations to determine ΔQ for every PAG size and transformation temperature combination individually in order to understand whether the PAG size itself has an effect on ΔQ by mechanisms such as its effect on the dislocation density in bainitic ferrite and hence the carbon partitioning process.

4. Investigating the effect of the prior austenite grain size and the transformation temperature on the phase transformation kinetics of bainite using a steel with a lower M_s temperature. This would enable investigations over a larger transformation temperature range to observe whether both effects, acceleration and deceleration by PAG refinement, can be observed in one steel at different transformation temperatures.

References

[1] Schmitt, J.-H., & Iung, T. (2018). New developments of advanced high-strength steels for automotive applications. *Comptes Rendus Physique*, *19*(8), 641–656. https://doi.org/10.1016/j.crhy.2018.11.004

[2] Fonstein, N. (2015a). Evolution of Strength of Automotive Steels to Meet Customer Challenges. In N. Fonstein (Ed.), *Advanced High Strength Sheet Steels: Physical Metallurgy, Design, Processing, and Properties* (pp. 1–16). Springer International Publishing. https://doi.org/10.1007/978-3-319-19165-2_1

[3] Verleysen, P. (2024, January). 10 - Dynamic behavior of high-strength steels for automotive applications. In M. Hokka (Ed.), *Dynamic Behavior of Materials* (pp. 295–337). Elsevier. https://doi.org/10.1016/B978-0-323-99153-7.00004-9

[4] Fonstein, N. (2015b). Candidates to AHSS of Third Generation: Steels with Carbide-Free Bainite. In N. Fonstein (Ed.), *Advanced High Strength Sheet Steels: Physical Metallurgy, Design, Processing, and Properties* (pp. 275–295). Springer International Publishing. https://doi.org/10.1007/978-3-319-19165-2_8

[5] De Cooman, B. C. (2004). Structure–properties relationship in TRIP steels containing carbide-free bainite. *Current Opinion in Solid State and Materials Science*, *8*(3), 285–303. https://doi.org/10.1016/j.cossms.2004.10.002

[6] Lin, S., Borgenstam, A., Stark, A., & Hedström, P. (2022). Effect of Si on bainitic transformation kinetics in steels explained by carbon partitioning, carbide formation, dislocation densities, and thermodynamic conditions. *Materials Characterization*, *185*, 111774. https://doi.org/10.1016/j.matchar.2022.111774

[7] Lu, J., Yu, H., Duan, X., & Song, C. (2020). Investigation of microstructural evolution and bainite transformation kinetics of multi-phase steel. *Materials Science and Engineering: A*, *774*, 138868. https://doi.org/10.1016/j.msea.2019.138868

[8] Li, K., Qian, L., Wei, C., Yu, W., Ren, L., Chen, Z., Zhang, F., & Meng, J. (2023). Effects of above- or below-$AC3$ austenitization on bainite transformation behavior, microstructure and mechanical properties of carbide-free bainitic steel. *Materials Science and Engineering: A*, *888*, 145814. https://doi.org/10.1016/j.msea.2023.145814

[9] Singh, S. B. (2012, January). 10 - Mechanisms of bainite transformation in steels. In E. Pereloma & D. V. Edmonds (Eds.), *Phase Transformations in Steels* (pp. 385–416, Vol. 1). Woodhead Publishing. https://doi.org/10.1533/9780857096104.3.385

[10] Rampelberg, C., Allain, S. Y. P., Geandier, G., Teixeira, J., Lebel, F., & Sourmail, T. (2021). Carbide-Free Bainite Transformations Above and Below Martensite Start Temperature Investigated by In-Situ High-Energy X-Ray Diffraction. *JOM*, *73*(11), 3181–3194. https://doi.org/10.1007/s11837-021-04903-8

[11] Bhadeshia, H., & Honeycombe, R. (2017a, January). Chapter 1 - Iron and Its Interstitial Solutions. In H. Bhadeshia & R. Honeycombe (Eds.), *Steels: Microstructure and Properties*

(Fourth Edition) (pp. 1–22). Butterworth-Heinemann. https://doi.org/10.1016/B978-0-08-100270-4.00001-9

[12] Porter, D. A., Easterling, K. E., & Easterling, K. E. (2009, February). *Phase Transformations in Metals and Alloys (Revised Reprint)* (0th ed.). CRC Press. https://doi.org/10.1201/9781439883570

[13] Benrabah, I.-E., Brechet, Y., Hutchinson, C., & Zurob, H. (2024). On the origin of carbon supersaturation in bainitic ferrite. *Scripta Materialia*, *250*, 116182. https://doi.org/10.1016/j.scriptamat.2024.116182

[14] Bhadeshia, H., & Honeycombe, R. (2017b). Bainite. In *Steels: Microstructure and Properties* (pp. 179–202). Elsevier. https://doi.org/10.1016/B978-0-08-100270-4.00006-8

[15] Ravi, A. M., Sietsma, J., & Santofimia, M. J. (2016). Exploring bainite formation kinetics distinguishing grain-boundary and autocatalytic nucleation in high and low-Si steels. *Acta Materialia*, *105*, 155–164. https://doi.org/10.1016/j.actamat.2015.11.044

[16] Fielding, L. C. D. (2013). The Bainite Controversy [Publisher: Taylor & Francis _eprint: https://doi.org/10.1179/1743284712Y.0000000157]. *Materials Science and Technology*, *29*(4), 383–399. https://doi.org/10.1179/1743284712Y.0000000157

[17] Bhadeshia, H. K. D. H., & Edmonds, D. V. (1980). The mechanism of bainite formation in steels. *Acta Metallurgica*, *28*(9), 1265–1273. https://doi.org/10.1016/0001-6160(80)90082-6

[18] Hulme-Smith, C. N., Lonardelli, I., Dippel, A. C., & Bhadeshia, H. K. D. H. (2013). Experimental evidence for non-cubic bainitic ferrite. *Scripta Materialia*, *69*(5), 409–412. https://doi.org/10.1016/j.scriptamat.2013.05.035

[19] Foster, D., Paladugu, M., Hughes, J., Kapousidou, M., Islam, U., Stark, A., Schell, N., & Jimenez-Melero, E. (2022). Formation of lower bainite in a high carbon steel – an in-situ synchrotron XRD study. *Journal of Materials Research and Technology*, *18*, 5380–5393. https://doi.org/10.1016/j.jmrt.2022.05.025

[20] Bhadeshia, H., & Honeycombe, R. (2017c, January). Chapter 5 - Formation of Martensite. In *Steels: Microstructure and Properties (Fourth Edition)* (pp. 135–177). Butterworth-Heinemann. https://doi.org/10.1016/B978-0-08-100270-4.00005-6

[21] Rees, G. I., & Bhadeshia, H. (1992a). Bainite transformation kinetics Part 2 Non-uniform distribution of carbon [Publisher: Taylor & Francis _eprint: https://doi.org/10.1179/mst.1992.8.11.994]. *Materials Science and Technology*, *8*(11), 994–1003. https://doi.org/10.1179/mst.1992.8.11.994

[22] Navarro Lopez, A. (2020). *Isothermal Phase Transformations Below the Martensite Start Temperature in a Low-Carbon Steel* [Doctoral dissertation, Delft University of Technology]. https://doi.org/10.4233/UUID:C51A53DF-60CD-41CA-9418-364DF17EBA56

[23] Bhadeshia, H., & Honeycombe, R. (2017d, January). Chapter 3 - Iron-Carbon Equilibrium and Plain Carbon Steels. In H. Bhadeshia & R. Honeycombe (Eds.), *Steels: Microstructure and Properties (Fourth Edition)* (pp. 59–100). Butterworth-Heinemann. https://doi.org/10.1016/B978-0-08-100270-4.00003-2

[24] dos Santos Avila, D., Offerman, S. E., & Santofimia, M. J. (2024). Modeling the effect of prior austenite grain size on bainite formation kinetics. *Acta Materialia*, *266*, 119656. https://doi.org/10.1016/j.actamat.2024.119656

[25] Yin, J., Leach, L., Hillert, M., & Borgenstam, A. (2017). C-Curves for Lengthening of Widmanstätten and Bainitic Ferrite. *Metallurgical and Materials Transactions A*, *48*(9), 3997–4005. https://doi.org/10.1007/s11661-017-4196-5

[26] Hillert, M., Höglund, L., & Ågren, J. (2004). Role of carbon and alloying elements in the formation of bainitic ferrite. *Metallurgical and Materials Transactions A*, *35*(12), 3693–3700. https://doi.org/10.1007/s11661-004-0275-5

[27] Hillert, M. (1994). Diffusion in growth of bainite. *Metallurgical and Materials Transactions A*, *25*(9), 1957–1966. https://doi.org/10.1007/BF02649044

[28] Benrabah, I.-E., Brechet, Y., Purdy, G., Hutchinson, C., & Zurob, H. (2023). On the origin of the barrier in the bainite phase transformation. *Scripta Materialia*, *223*, 115076. https://doi.org/10.1016/j.scriptamat.2022.115076

[29] Leach, L., Hillert, M., & Borgenstam, A. (2015). Modeling C-Curves for the Growth Rate of Widmanstätten and Bainitic Ferrite in Fe-C Alloys. *Metallurgical and Materials Transactions A*, *47*. https://doi.org/10.1007/s11661-015-3241-5

[30] Kaufman, L., Radcliffe, S., & Cohen, M. (1962, January). Thermodynamics of the Bainite reaction. In *Decomposition of austenite by diffusional processes: Proceedings of a symposium held in Philadelphia, Pennsylvania, October 19, 1960, under the sponsorship of the Ferrous Metallurgy Committee of the Institute of Metals Division, the Metallurgical Society, American Institute of Mining, Metallurgical* (pp. 313–351, Vol. 1). Interscience Publishers.

[31] Navarro-López, A., Sietsma, J., & Santofimia, M. J. (2016). Effect of Prior Athermal Martensite on the Isothermal Transformation Kinetics Below Ms in a Low-C High-Si Steel. *Metallurgical and Materials Transactions A*, *47*(3), 1028–1039. https://doi.org/10.1007/s11661-015-3285-6

[32] Rees, G. I., & Bhadeshia, H. (1992b). Bainite transformation kinetics Part 1 Modified model [Publisher: Taylor & Francis _eprint: https://doi.org/10.1179/mst.1992.8.11.985]. *Materials Science and Technology*, *8*(11), 985–993. https://doi.org/10.1179/mst.1992.8.11.985

[33] Lu, S.-Y., Chung, T.-F., Chen, J.-J., Lai, Y.-W., Hsiao, C.-N., Chen, C.-Y., Wang, S.-H., & Yang, J.-R. (2023). Development of microstructures-properties in Fe-0.4C/0.2C-2Si-3Mn carbide-free bainite steels. *Materials Characterization*, *197*, 112670. https://doi.org/10.1016/j.matchar.2023.112670

[34] Gong, W., Tomota, Y., Harjo, S., Su, Y. H., & Aizawa, K. (2015). Effect of prior martensite on bainite transformation in nanobainite steel. *Acta Materialia*, *85*, 243–249. https://doi.org/10.1016/j.actamat.2014.11.029

[35] Garcia-Mateo, C., Sourmail, T., Philippot, A., Morales-Rivas, L., & Jimenez, J. A. (2024). Effect of prior martensite on bainitic transformation of high Si hypereutectoid steel. *Journal*

of Materials Research and Technology, *30*, 6995–7005. https://doi.org/10.1016/j.jmrt.2024.05.090

[36] Ravi, A. M., Navarro-López, A., Sietsma, J., & Santofimia, M. J. (2020). Influence of martensite/austenite interfaces on bainite formation in low-alloy steels below *Ms*. *Acta Materialia*, *188*, 394–405. https://doi.org/10.1016/j.actamat.2020.02.003

[37] Ravi, A. M., Kumar, A., Herbig, M., Sietsma, J., & Santofimia, M. J. (2020). Impact of austenite grain boundaries and ferrite nucleation on bainite formation in steels. *Acta Materialia*, *188*, 424–434. https://doi.org/10.1016/j.actamat.2020.01.065

[38] Hasan, S. M., Kumar, S., Chakrabarti, D., & Singh, S. B. (2020). Effect of prior austenite grain size on the formation of carbide-free bainite in low-alloy steel [Publisher: Taylor & Francis _eprint: https://doi.org/10.1080/14786435.2020.1764653]. *Philosophical Magazine*, *100*(18), 2320–2334. https://doi.org/10.1080/14786435.2020.1764653

[39] Barford, J., & Owen, W. (1962). The effect of austenite grain size and temperature on the rate of the bainite transformation. *Metal Science and Heat Treatment of Metals*, *4*(7), 359–360. https://doi.org/10.1007/BF00814454

[40] Umemoto, M., HORIUCHI, K., & TAMURA, I. (1982). Transformation Kinetics of Bainite during Isothermal Holding and Continuous Cooling. *Tetsu-to-Hagane*, *68*, 461–470. https://doi.org/10.2355/tetsutohagane1955.68.3_461

[41] Davenport, E. S., Grange, R. A., & Hafsten, R. J. (1941). Influence of austenite grain size upon isothermal transformation behavior of SAE 4140 steel. *Trans. AIME*, (145), 301.

[42] Matsuzaki, A., & Bhadeshia, H. (1999). Effect of austenite grain size and bainite morphology on overall kinetics of bainite transformation in steels [Publisher: Taylor & Francis _eprint: https://doi.org/10.1179/026708399101506210]. *Materials Science and Technology*, *15*(5), 518–522. https://doi.org/10.1179/026708399101506210

[43] Eres-Castellanos, A., Hidalgo, J., Zorgani, M., Jahazi, M., Toda-Caraballo, I., Caballero, F. G., & Garcia-Mateo, C. (2021). Assessing the scale contributing factors of three carbide-free bainitic steels: A complementary theoretical and experimental approach. *Materials & Design*, *197*, 109217. https://doi.org/10.1016/j.matdes.2020.109217

[44] Chhajed, B., Mishra, K., Singh, K., & Singh, A. (2022). Effect of prior austenite grain size on the tensile properties and fracture toughness of nano-structured bainite. *Materials Characterization*, *192*, 112214. https://doi.org/10.1016/j.matchar.2022.112214

[45] Willmott, P. (2019). Synchrotron Physics [Section: 3 _eprint: https://onlinelibrary.wiley.com/doi/pdf/10.1002/978 In *An Introduction to Synchrotron Radiation* (pp. 51–106). John Wiley & Sons, Ltd. https://doi.org/10.1002/9781119280453.ch3

[46] Epp, J. (2016, January). 4 - X-ray diffraction (XRD) techniques for materials characterization. In G. Hübschen, I. Altpeter, R. Tschuncky & H.-G. Herrmann (Eds.), *Materials Characterization Using Nondestructive Evaluation (NDE) Methods* (pp. 81–124). Woodhead Publishing. https://doi.org/10.1016/B978-0-08-100040-3.00004-3

[47] Grange, R. A. (1971). The rapid heat treatment of steel. *Metallurgical Transactions*, *2*(1), 65–78. https://doi.org/10.1007/BF02662639

[48] Lutterotti, L. (n.d.). Maud: A Rietveld Analysis Program Designed for the Internet and Experiment Integration. Retrieved 12th January 2025, from https://luttero.github.io/maud/maud/release/2023/07/03/new-version-2.999.html

[49] Lutterotti, L., & Scardi, P. (1990). Simultaneous structure and size–strain refinement by the Rietveld method [Publisher: International Union of Crystallography]. *Journal of Applied Crystallography*, *23*(4), 246–252. https://doi.org/10.1107/S0021889890002382

[50] Pushkareva, I., Macchi, J., Shalchi-Amirkhiz, B., Fazeli, F., Geandier, G., Danoix, F., Teixeira, J. D. C., Allain, S. Y. P., & Scott, C. (2023). A study of the carbon distribution in bainitic ferrite. *Scripta Materialia*, *224*, 115140. https://doi.org/10.1016/j.scriptamat.2022.115140

[51] Cai, W., & Nix, W. D. (2016, September). Imperfections in Crystalline Solids [ISBN: 9781316389508 Publisher: Cambridge University Press]. https://doi.org/10.1017/CBO9781316389508

[52] Turunen, M. J., De Keijser, T., Delhez, R., & Pers, N. M. V. D. (1983). A method for the interpretation of the Warren–Averbach mean-squared strains and its application to recovery in aluminium. *Journal of Applied Crystallography*, *16*(2), 176–182. https://doi.org/10.1107/S0021889883010225

[53] He, S. H., He, B. B., Zhu, K. Y., & Huang, M. X. (2017). On the correlation among dislocation density, lath thickness and yield stress of bainite. *Acta Materialia*, *135*, 382–389. https://doi.org/10.1016/j.actamat.2017.06.050

[54] Xiao, X., Li, S., & Yu, L. (2022). A general steady-state creep model incorporating dislocation static recovery for pure metallic materials. *International Journal of Plasticity*, *157*, 103394. https://doi.org/10.1016/j.ijplas.2022.103394

[55] Quidort, D., & Brechet, Y. J. M. (2001). Isothermal growth kinetics of bainite in 0.5% C steels. *Acta Materialia*, *49*(20), 4161–4170. https://doi.org/10.1016/S1359-6454(01)00316-0

[56] Zhu, K., Chen, H., Masse, J.-P., Bouaziz, O., & Gachet, G. (2013). The effect of prior ferrite formation on bainite and martensite transformation kinetics in advanced high-strength steels. *Acta Materialia*, *61*(16), 6025–6036. https://doi.org/10.1016/j.actamat.2013.06.043

[57] Celada-Casero, C., Kwakernaak, C., Sietsma, J., & Santofimia, M. J. (2019). The influence of the austenite grain size on the microstructural development during quenching and partitioning processing of a low-carbon steel. *Materials & Design*, *178*, 107847. https://doi.org/10.1016/j.matdes.2019.107847

[58] Singh, S. B., & Bhadeshia, H. K. D. H. (1998). Estimation of bainite plate-thickness in low-alloy steels. *Materials Science and Engineering: A*, *245*(1), 72–79. https://doi.org/10.1016/S0921-5093(97)00701-6

[59] Yang, Z., Chu, C., Jiang, F., Qin, Y., Long, X., Wang, S., Chen, D., & Zhang, F. (2019). Accelerating nano-bainite transformation based on a new constructed microstructural predicting model. *Materials Science and Engineering: A*, *748*, 16–20. https://doi.org/10.1016/j.msea.2019.01.061

[60] van Bohemen, S. M. C. (2018). Exploring the correlation between the austenite yield strength and the bainite lath thickness. *Materials Science and Engineering: A*, *731*, 119–123. https://doi.org/10.1016/j.msea.2018.06.041

[61] Anderson, P., Hirth, J., & Lothe, J. (2017, April). 21 - Dislocation Pileups and Cracks. In *Theory of dislocations* (pp. 587–609, Vol. 3). Cambridge University Press. Retrieved 23rd January 2025, from https://www.cambridge.org/nl/universitypress/subjects/engineering/materials-science/theory-dislocations-3rd-edition?format=HB&isbn=9780521864367

[62] Singh, K., Kumar, A., & Singh, A. (2018). Effect of Prior Austenite Grain Size on the Morphology of Nano-Bainitic Steels. *Metallurgical and Materials Transactions A*, *49*(4), 1348–1354. https://doi.org/10.1007/s11661-018-4492-8

[63] Traka, K., Sietsma, J., & Santofimia Navarro, M. J. (2024). Modeling the interaction of carbon segregation to defects and carbon partitioning in multiphase steels. *Acta Materialia*, *277*, 120204. https://doi.org/10.1016/j.actamat.2024.120204

[64] Dai, Z., Yang, Z., Zhang, C., & Chen, H. (2020). Incomplete carbon partitioning during quenching and partitioning of Fe–C–Mn–Si steels: Modeling and experimental validations. *Acta Materialia*, *200*, 597–607. https://doi.org/10.1016/j.actamat.2020.09.045

[65] Parker, S. V. (1998). Modelling of Phase Transformations in Hot-Rolled Steels. https://doi.org/10.17863/CAM.14220

[66] Bhadeshia, H. K. D. H. (2001). Chapter 6 - Kinetics. In *Bainite in steels: Transformations, microstructure and properties.* (pp. 129–188, Vol. 2). OM Communications. Retrieved 25th January 2025, from https://tudelft.on.worldcat.org/search/detail/840369491?queryString=H.K.D.H.%20Bhadeshia%3A%20Bainite%20in%20Steels%2C%20The%20Institute%20of%20Materials%2C%20London%2C%202001.

[67] Van Bohemen, S. (2010). Modeling Start Curves of Bainite Formation. *Metallurgical and Materials Transactions A*, *41*(2), 285–296. https://doi.org/10.1007/s11661-009-0106-9

[68] Jiang, T., Liu, H., Sun, J., Guo, S., & Liu, Y. (2016). Effect of austenite grain size on transformation of nanobainite and its mechanical properties. *Materials Science and Engineering: A*, *666*, 207–213. https://doi.org/10.1016/j.msea.2016.04.041

[69] Durand-Charre, M. (2004). Appendix 22 - 5 Characteristic diffusion lengths. In *Microstructure of Steels and Cast Iron* (p. 369). Springer. https://tudelft.on.worldcat.org/search/detail/840385092?queryString=Microstructure%20of%20steels%20and%20cast%20iron

[70] Liu, S. K., & Zhang, J. (1990). The influence of the Si and Mn concentrations on the kinetics of the bainite transformation in Fe-C-Si-Mn alloys. *Metallurgical Transactions A*, *21*(6), 1517–1525. https://doi.org/10.1007/BF02672566

Appendix

A Examples of the definition of the starting time of the phase transformation to bainite

Figure A1 presents the definition of the starting time of the phase transformation to bainite in 1100-410. In this case, the first temperature minimum within a range of ± 5°C of the intended isothermal transformation temperature occurs at a temperature below 410°C. In contrast, in 900-440 the first temperature minimum and a following stagnation of the temperature occur above 440°C, as it is presented in Figure A2. It takes more than 10 seconds for the temperature to stabilize at the intended isothermal transformation temperature of 440°C. However, during that time the phase transformation to bainite has already started, which is the reason why this first minimum has been defined as the starting time of the phase transformation.

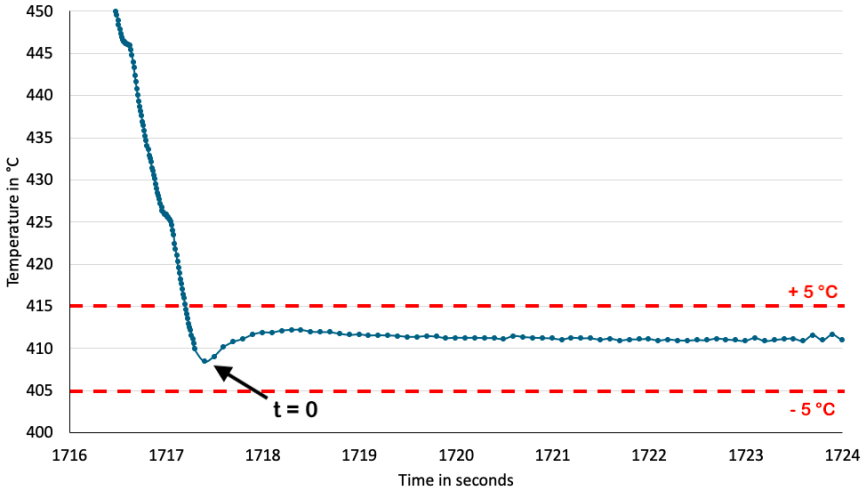

Figure A1: Definition of starting time of the phase transformation to bainite in 1100-410.

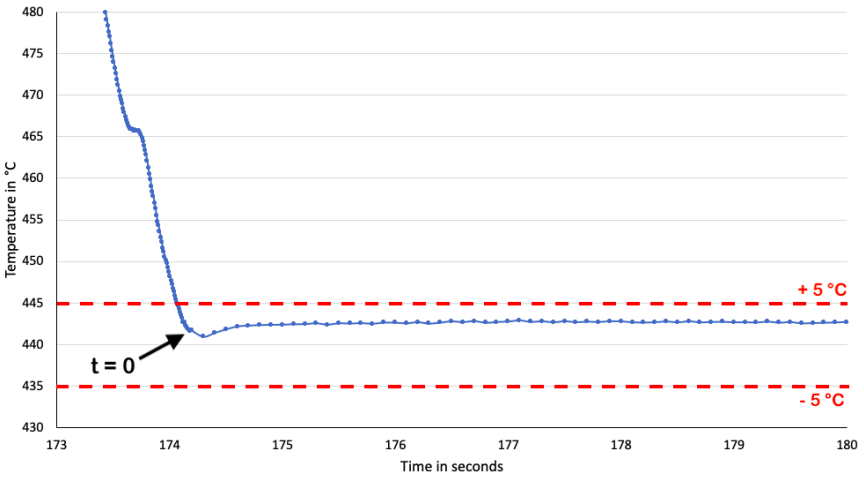

Figure A2: Definition of starting time of the phase transformation to bainite in 900-440.

B Asymmetry in austenite peaks

Figure B1 exhibits asymmetric austenite peaks detected in experiment 1100-380 developed after 190 seconds of holding at the isothermal transformation temperature. The arrows point to the asymmetric FCC peaks.

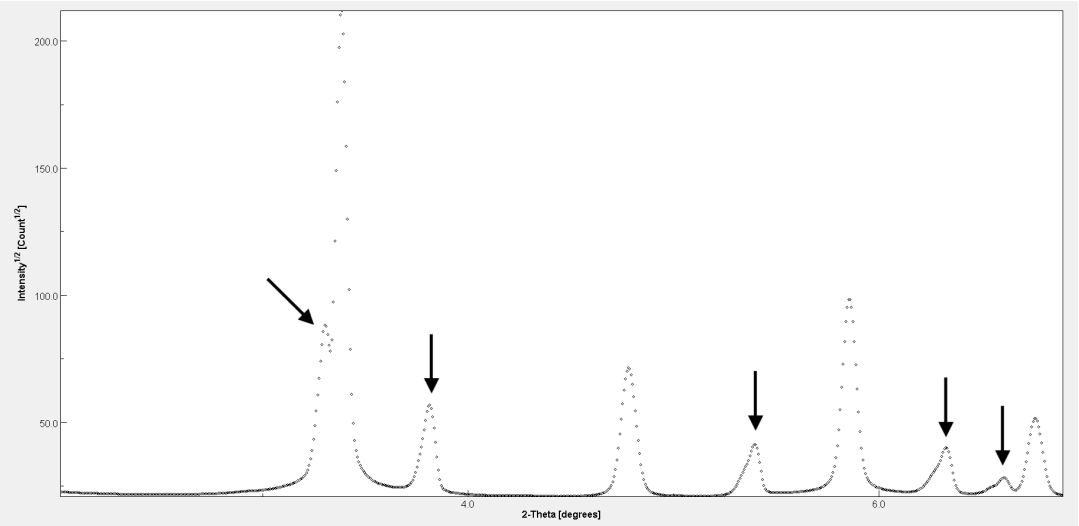

Figure B1: Example of asymmetric austenite peaks.

C Effect of large prior austenite grains on XRD patterns

Figure C1 exhibits an example the evolution of the effect of large PAGs on 1D and 2D XRD patterns in experiment 1100-440. Figure C1b shows large spots in the 2D diffraction pattern recorded after approximately 4 seconds of holding. The large spots cause the first two austenite peaks to be broadened at the bottom in the 1D diffraction pattern presented in Figure C1a. Figure C1d and Figure C1f show that the size of the spots decreases significantly within 38 seconds of holding and, therefore, the broadening resulting from these spots, presented in Figure C1c and Figure C1e, decreases. Figure C1h and Figure C1g show the 2D and 1D patterns recorded after 584 seconds of holding.

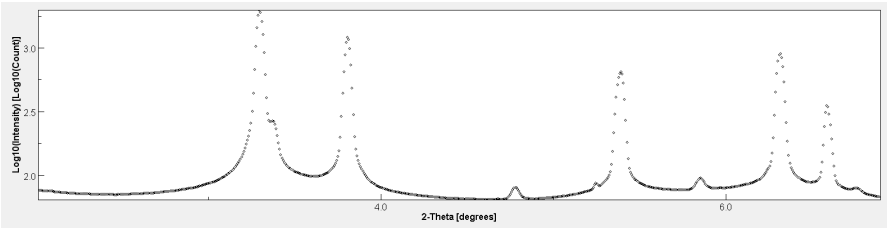

(a) 1D diffraction pattern at 4 seconds of holding.

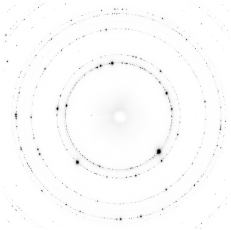

(b) 2D diffraction pattern at 4 seconds of holding.

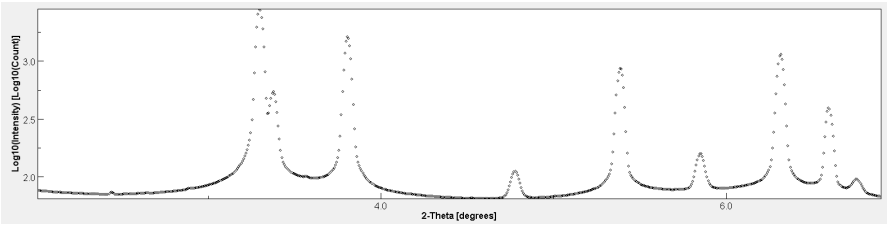

(c) 1D diffraction pattern at 18 seconds of holding.

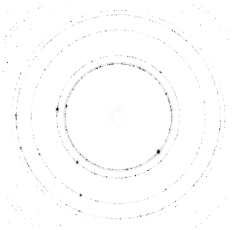

(d) 2D diffraction pattern at 18 seconds of holding.

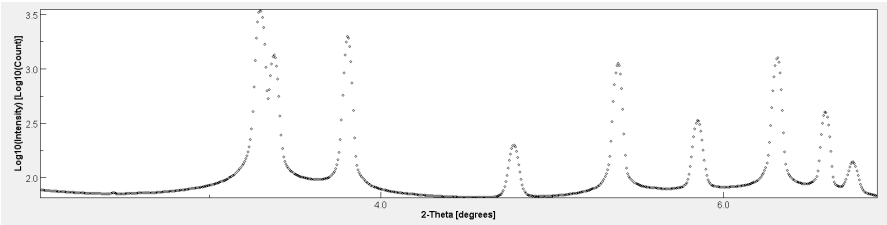

(e) 1D diffraction pattern at 38 seconds of holding.

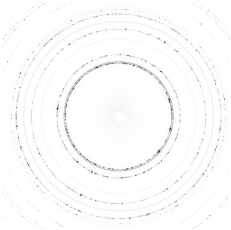

(f) 2D diffraction pattern at 38 seconds of holding.

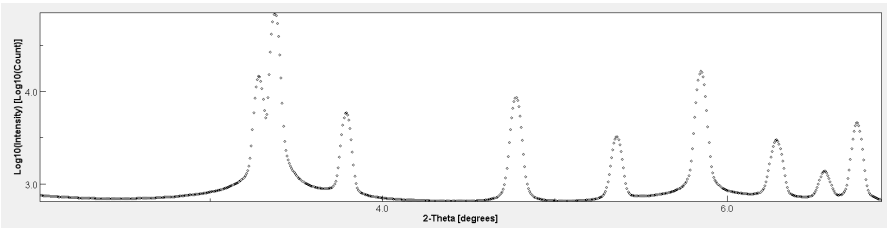

(g) 1D diffraction pattern at 584 seconds of holding.

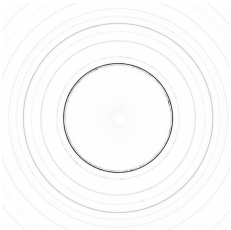

(h) 2D diffraction pattern at 584 seconds of holding.

Figure C1: Evolution of the effect of large prior austenite grains on XRD patterns in 1100-440.

For comparison Figure C2 presents 1D and 2D diffraction patterns recorded at the beginning and at the end of the bainitic phase transformation in experiment 900-440. Figure C2b shows that there are no spots in the 2D diffraction pattern due to the smaller prior austenite grain size of the sample.

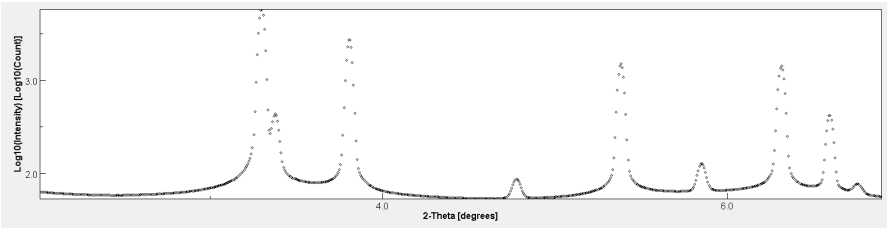

(a) 1D diffraction pattern at 6 seconds of holding.

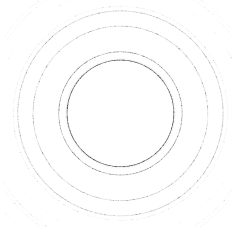

(b) 2D diffraction pattern at 6 seconds of holding.

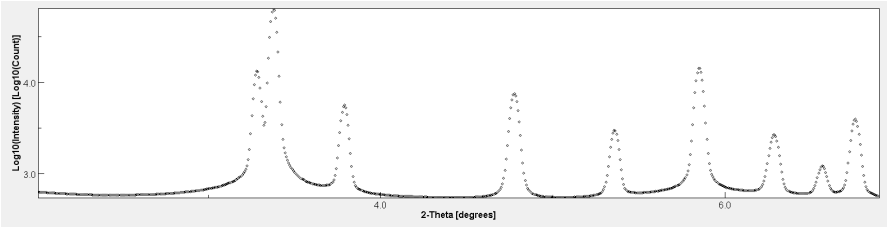

(c) 1D diffraction pattern at 592 seconds of holding.

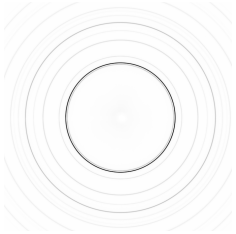

(d) 2D diffraction pattern at 592 seconds of holding.

Figure C2: XRD patterns recorded at the beginning and end of the isothermal holding in experiment 900-440.

D Rietveld refinement

The following tables present a documentation of the Rietveld refinements performed for the specimens transformed at 440°C, 410°C and 380°C. The columns show the following data:

General information:

- Nr.: Number of the refinement.
- Holding time: Time of isothermal holding at the transformation temperature relative to the specified start time.
- Temperature: Temperature measured by the thermocouple.

Evaluation fit:

- Sigma: Standard deviation of the profile function.
- R_{wp}: Weighted profile R-factor.

Lattice parameter in Å:

- Alpha: Lattice parameter determined for bainitic ferrite.
- Gamma: Lattice parameter determined for austenite.
- Gamma+: Lattice parameter determined for carbon-rich austenite.
- Average gamma: Average austenite lattice parameter based on the average of the lattice parameters determined for austenite and carbon-rich austenite weighted by their phase fractions.
- Relative change: Change of the average austenite lattice parameter relative to its starting value.

Fraction in wt.% :

- Alpha: Fraction of bainitic ferrite.
- Error fraction alpha: The positive and negative error predicted for the bainitic ferrite fraction. The error is given in wt.%. The software MAUD was only able to give accurate error predictions for refinements without carbon-rich austenite.
- Gamma: Fraction of austenite.
- Gamma+: Fraction of carbon-rich austenite.

Microstrain:

- Alpha: Microstrain determined for bainitic ferrite.
- Gamma: Microstrain determined for austenite.
- Gamma+: Microstrain determined for carbon-rich austenite.

Visual fit:

- Comments on the visual fit of the refined function.

Comments:

- Comments on the detection of ferrite or carbides.

General information			Evaluation fit		Lattice parameter in Å					Fraction in wt.%				Microstrain			Visual fit	Comments
Nr.	Holding time in s	Temperature in °C	Sigma	Rwp	Alpha	Gamma	Gamma+	Average gamma	Relative change gamma	Alpha	Error fraction alpha	Gamma	Gamma+	Alpha	Gamma	Gamma+		
1	-9,73	900,03	0,08	7,21	0,0000	3,6490	0,0000	3,6490		0,0	0,0	100,0	0,0	0,0000	0,0015	0,0000	First two gamma peaks are broader at the bottom and peak positions of the refined function do not match perfectly.	Ferrite peaks are visible.
2	3,51	440,73	1,18	10,30	2,8806	3,6110	0,0000	3,6110	0,0000	5,3	0,4	94,7	0,0	0,0056	0,0019	0,0000	First two gamma peaks are broader at the bottom and peak positions of the function do not match perfectly. Alpha peak positions and shape are not matched well, due to relatively small fraction.	
3	8,32	441,01	1,35	11,39	2,8783	3,6108	0,0000	3,6108	-0,0002	5,9	0,3	94,1	0,0	0,0045	0,0018	0,0000	First two gamma peaks are broader at the bottom and peak positions of the function match better now. Alpha peak positions match better but peak shape is not matched well, due to relatively small fraction.	
4	18,35	441,75	0,99	8,05	2,8782	3,6106	0,0000	3,6106	-0,0004	9,5	0,2	90,5	0,0	0,0035	0,0015	0,0000	First two gamma peaks match better at the bottom and peak position matches good. Alpha peaks match better.	
5	38,41	440,44	1,06	7,92	2,8784	3,6117	0,0000	3,6117	0,0007	19,4	0,2	80,6	0,0	0,0031	0,0015	0,0000	Gamma peaks match well, alpha peaks match well.	
6	58,67	439,92	1,28	9,07	2,8787	3,6128	0,0000	3,6128	0,0018	30,3	0,3	69,7	0,0	0,0029	0,0016	0,0000	Gamma peaks match well, alpha peaks match well.	
7	78,43	440,01	1,57	10,86	2,8790	3,6119	3,6290	3,6140	0,0030	42,1		50,8	7,1	0,0029	0,0015	0,0050	Gamma peaks match well, alpha peaks match well.	
8	84,00	439,96	1,62	11,07	2,8790	3,6117	3,6276	3,6145	0,0035	45,3		45,2	9,5	0,0028	0,0015	0,0047	Gamma peaks match well, alpha peaks match well.	
9	98,59	439,97	1,58	10,83	2,8790	3,6115	3,6287	3,6158	0,0048	52,4		35,8	11,8	0,0028	0,0016	0,0045	Gamma peaks match well, alpha peaks match well.	
10	118,65	439,94	1,55	11,06	2,8790	3,6115	3,6304	3,6178	0,0068	59,8		26,7	13,5	0,0028	0,0018	0,0045	Gamma peaks match well, alpha peaks match well.	Carbide peaks were detected.
11	133,19	439,98	1,51	10,32	2,8790	3,6114	3,6331	3,6191	0,0081	63,9		23,4	12,8	0,0027	0,0019	0,0038	Gamma peaks match well, alpha peaks match well.	Carbide peaks were detected.
12	134,10	440,00	1,56	10,68	2,8790	3,6107	3,6278	3,6175	0,0065	64,1		21,6	14,3	0,0027	0,0018	0,0045	Gamma peaks match well, alpha peaks match well.	Carbide peaks were detected.
13	134,50	440,07	1,51	10,32	2,8790	3,6114	3,6339	3,6188	0,0078	64,2		24,0	11,8	0,0027	0,0020	0,0038	Gamma peaks match well, alpha peaks match well.	Carbide peaks were detected.
14	135,50	440,03	1,50	10,26	2,8790	3,6115	3,6336	3,6193	0,0083	64,4		23,1	12,5	0,0027	0,0019	0,0038	Gamma peaks match well, alpha peaks match well.	Carbide peaks were detected.
15	168,15	440,08	4,76	10,45	2,8790	3,6133	3,6389	3,6211	0,0101	69,9		20,8	9,2	0,0027	0,0023	0,0030	Gamma peaks match well, alpha peaks match well.	Carbide peaks were detected.
16	187,25	440,08	4,75	10,44	2,8789	3,6128	3,6363	3,6225	0,0115	71,9		16,5	11,7	0,0027	0,0023	0,0033	Gamma peaks match well, alpha peaks match well.	Carbide peaks were detected.
17	280,60	440,07	4,75	10,42	2,8789	3,6257	0,0000	3,6257	0,0147	76,2	1,5	23,8	0,0	0,0026	0,0041	0,0000	Gamma peaks match well, alpha peaks match well.	Carbide peaks were detected.
18	408,30	439,98	4,79	10,52	2,8787	3,6268	0,0000	3,6268	0,0158	77,8	1,1	22,2	0,0	0,0025	0,0038	0,0000	Gamma peaks match well, alpha peaks match well.	Carbide peaks were detected.
19	583,90	440,02	4,80	10,55	2,8788	3,6270	0,0000	3,6270	0,0160	78,9	1,1	21,1	0,0	0,0024	0,0035	0,0000	Gamma peaks match well, alpha peaks match well.	Carbide peaks were detected.
20	639,65	27,09	3,59	7,84	2,8617	3,6006	0,0000	3,6006		83,1	1,3	16,9	0,0	0,0025	0,0035	0,0000	Gamma peaks match well, alpha peaks match well.	Carbide peaks were detected.

Figure D1: Documentation of the Rietveld refinements performed for 1100-440.

General information			Evaluation fit		Lattice parameter in Å					Fraction in wt.%				Microstrain			Visual fit	Comments
Nr.	Holding time in s	Temperature in °C	Sigma	Rwp	Alpha	Gamma	Gamma+	Average gamma	Relative change gamma	Alpha	Error fraction alpha	Gamma	Gamma+	Alpha	Gamma	Gamma+		
1	0	900,01	1,556	13,581	0	3,65	0	3,65		0	0	100	0	0	0,0025	0	First two gamma peaks are broader at the bottom and peak positions of the refined function do not match perfectly.	Ferrite peaks are visible.
2	3,11	411,19	1,883	17,645	2,875	3,6078	0	3,6078	3,6078	5,8919	0,6898	94,1081	0	0,0035	0,0015	0	First two gamma peaks are a bit broader at the bottom but peak positions of the function match okay. Alpha peak positions and shape are not matched well, due to relatively small fraction.	
3	13,14	411,19	1,608	14,2	2,876	3,6075	0	3,6075	3,6075	8,1706	0,6526	91,8294	0	0,0033	0,0013	0	Gamma peak shapes and positions of the function match better now. Alpha peaks match better.	
4	23,18	411,5	1,372	11,272	2,877	3,6078	0	3,6078	3,6078	12,535	0,3444	87,4655	0	0,0038	0,0011	0	Gamma peaks match well, alpha peaks match well.	
5	33,21	410,53	1,465	11,291	2,877	3,6083	0	3,6083	3,6083	17,402	0,3506	82,5978	0	0,0038	0,0012	0	Gamma peaks match well, alpha peaks match well.	
6	43,24	410,47	1,598	11,716	2,878	3,6086	0	3,6086	3,6086	22,682	0,3851	77,3176	0	0,0038	0,0014	0	Gamma peaks match well, alpha peaks match well.	
7	63,31	410,12	1,76	12,2	2,878	3,609	0	3,609	3,609	34,961	0,4867	64,0391	0	0,0036	0,0046	0	Gamma peaks match well, alpha peaks match well.	Carbide peaks were detected.
8	78,5	409,96	1,753	11,968	2,878	3,6085	3,6248	3,610645	3,610645187	45,165		47,6187	7,2167	0,0035	0,0012	0,0067	Gamma peaks match well, alpha peaks match well.	Carbide peaks were detected.
9	83,38	410,02	1,762	11,985	2,878	3,6085	3,625	3,611056	3,61105581	48,276		43,7125	8,012	0,0035	0,0012	0,00653	Gamma peaks match well, alpha peaks match well.	Carbide peaks were detected.
10	103,45	410,13	1,8	12,199	2,878	3,6082	3,6256	3,613001	3,613000876	59,776		29,1257	11,0983	0,0034	0,0013	0,00616	Gamma peaks match well, alpha peaks match well.	Carbide peaks were detected.
11	123,51	410,02	1,715	11,637	2,878	3,608	3,6264	3,615463	3,615463328	67,965		19,0414	12,9941	0,0033	0,0014	0,00587	Gamma peaks match well, alpha peaks match well.	Carbide peaks were detected.
12	146,09	410,08	5,245	11,433	2,878	3,6076	3,6269	3,618208	3,61820794	73,906		11,7518	14,3421	0,0033	0,0012	0,00568	Gamma peaks match well, alpha peaks match well.	Carbide peaks were detected.
13	184,24	410,05	5,125	11,184	2,878	3,6069	3,6284	3,622132	3,622132335	79,188		6,0671	14,7449	0,0032	0,0011	0,00538	Gamma peaks match well, alpha peaks match well.	Carbide peaks were detected.
14	227,14	410,03	5,136	11,177	2,878	3,606	3,6283	3,624963	3,624963315	81,884		2,7106	15,4051	0,0032	0,0006	0,00528	Gamma peaks match well, alpha peaks match well.	Carbide peaks were detected.
15	303,54	409,92	5,115	11,156	2,878	3,6275	0	3,6275	3,6275	83,871	1,5421	16,1292	0	0,0031	0,0052	0	Gamma peaks match well, alpha peaks match well.	Carbide peaks were detected.
16	406,54	410,01	5,104	11,136	2,878	3,6293	0	3,6293	3,6293	84,936	1,6042	15,0637	0	0,0031	0,0049	0	Gamma peaks match well, alpha peaks match well.	Carbide peaks were detected.
17	548,94	410,04	5,121	11,153	2,877	3,6299	0	3,6299	3,6299	85,538	1,6442	14,4624	0	0,003	0,0046	0	Gamma peaks match well, alpha peaks match well.	Carbide peaks were detected.
18	615,75	25,11	3,883	8,444	2,861	3,6056	0	3,6056		87,196	1,2428	12,8044	0	0,0029	0,004	0	Gamma peaks match well, alpha peaks match well.	Carbide peaks were detected.

Figure D2: Documentation of the Rietveld refinements performed for 1100-410.

General information			Evaluation fit		Lattice parameter in Å					Fraction in wt.%				Microstrain			Visual fit	Comments
Nr.	Holding time in s	Temperature in °C	Sigma	Rwp	Alpha	Gamma	Gamma+	Average gamma	Relative change gamma	Alpha	Error fraction alpha	Gamma	Gamma+	Alpha	Gamma	Gamma+		
1	-10,74	900,15	0,88	9,3941	0	3,6487	0	3,6487		0	0	100	0	0	0,0017	0	First three gamma peaks are broader at the bottom and peak positions of the refined function do not match perfectly.	Ferrite peaks are visible.
2	6,56	381,22	1,017	11,0166	2,873	3,6042	0	3,6042	3,6042	2,9864	0,2974	97,0136	0	0,00337	0,0013	0	First three gamma peaks are a bit broader at the bottom but peak positions of the function match okay. Alpha peak positions and shape are not matched well, due to relatively small fraction.	
3	9,62	381,23	1,064	11,272	2,873	3,6046	0	3,6046	3,6046	4,3144	0,3257	95,6856	0	0,0057	0,0013	0	Gamma peak shapes and positions of the function match better now. Alpha peak positions and shape are not matched well, due to relatively small fraction.	
4	19,79	381,35	1,031	9,9775	2,875	3,6045	0	3,6045	3,6045	6,2963	0,2431	93,7037	0	0,00494	0,0013	0	Gamma peak shapes and positions of the function match better now. Alpha peaks match better.	Carbide peaks were detected.
5	40,14	380,47	1,186	10,4036	2,875	3,6041	0	3,6041	3,6041	16,0391	0,2842	83,9609	0	0,00376	0,0011	0	Gamma peaks match well, alpha peaks match well.	Carbide peaks were detected.
6	60,5	379,98	1,293	10,8719	2,875	3,6044	0	3,6044	3,6044	32,3268	0,4048	67,6732	0	0,00383	0,0016	0	Gamma peaks match well, alpha peaks match well.	Carbide peaks were detected.
7	75,5	379,98	1,264	10,5213	2,875	3,6041	3,628	3,605563	3,605563024	45,3118		51,3404	3,3477	0,00385	0,0017	0,00827	Gamma peaks match well, alpha peaks match well.	Carbide peaks were detected.
8	80,85	379,78	1,241	10,3066	2,875	3,604	3,6253	3,605801	3,60580109	49,2871		46,4248	4,2882	0,00384	0,0017	0,00818	Gamma peaks match well, alpha peaks match well.	Carbide peaks were detected.
9	101,3	380,06	1,188	9,8398	2,875	3,6036	3,6244	3,607091	3,607090986	61,769		31,8143	6,4165	0,00384	0,0018	0,00748	Gamma peaks match well, alpha peaks match well.	Carbide peaks were detected.
10	121,66	379,9	1,168	9,6663	2,875	3,6032	3,6241	3,608626	3,608626339	69,6137		22,497	7,8893	0,00382	0,0019	0,0072	Gamma peaks match well, alpha peaks match well.	Carbide peaks were detected.
11	129,69	380,1	1,202	9,8819	2,875	3,6034	3,624	3,609589	3,609589381	71,4743		19,955	8,5707	0,00382	0,002	0,00792	Gamma peaks match well, alpha peaks match well.	Carbide peaks were detected.
12	162,35	380,2	3,787	10,0417	2,875	3,603	3,6242	3,612367	3,61236719	77,8621		12,3563	9,7816	0,00379	0,002	0,00743	Gamma peaks match well, alpha peaks match well.	Carbide peaks were detected.
13	191,05	379,96	3,812	10,136	2,875	3,6029	3,6243	3,614538	3,614537744	81,0257		8,6557	10,3186	0,00376	0,0021	0,00718	Gamma peaks match well, alpha peaks match well.	Carbide peaks were detected.
14	225,7	379,93	3,814	10,1409	2,875	3,6028	3,6245	3,616732	3,616732074	83,3722		5,9522	10,6755	0,00374	0,0021	0,00698	Gamma peaks match well, alpha peaks match well.	Carbide peaks were detected.
15	272,55	379,98	3,814	10,1528	2,875	3,6031	3,625	3,619379	3,619378638	85,4299		3,7399	10,8302	0,00371	0,0021	0,00678	Gamma peaks match well, alpha peaks match well.	Carbide peaks were detected.
16	318,4	379,91	3,727	9,9201	2,875	3,6026	3,623	3,620557	3,620556811	86,9243		1,566	11,5097	0,00368	0,001	0,0065	Gamma peaks match well, alpha peaks match well.	Carbide peaks were detected.
17	436,3	379,95	3,739	9,9923	2,875	3,6236	0	3,6236	3,6236	88,5052	1,8852	11,4948	0	0,00364	0,0062	0	Gamma peaks match well, alpha peaks match well.	Carbide peaks were detected.
18	580,8	380,08	3,753	10,0089	2,875	3,626	0	3,626	3,626	89,3721	1,9766	10,6279	0	0,00361	0,0058	0	Gamma peaks match well, alpha peaks match well.	Carbide peaks were detected.
19	636,99	26,62	2,88	7,6406	2,86	3,6052	0	3,6052		90,9806	1,5324	9,0194	0	0,00354	0,0048	0	Gamma peaks match well, alpha peaks match well.	Carbide peaks were detected.

Figure D3: Documentation of the Rietveld refinements performed for 1100-380.

General information			Evaluation fit		Lattice parameter in Å					Fraction in wt.%				Microstrain			Visual fit	Comments
Nr.	Holding time in s	Temperature in °C	Sigma	Rwp	Alpha	Gamma	Gamma+	Average gamma	Relative change gamma	Alpha	Error fraction alpha	Gamma	Gamma+	Alpha	Gamma	Gamma+		
1	-9,43	900,08	1,567	13,2656	0	3,6486	0			0	0	100	0	0	6E-05	0	First gamma peak is broader at the bottom but peak positions match okay.	
2	2,71	442,72	1,488	11,42	2,876	3,6103	0	3,6103	3,6103	3,0481	0,1808	96,9519	0	0,00294	4E-05	0	First gamma peak is broader at the bottom but peak positions match okay. Alpha peak positions and shape are not matched well, due to relatively small fraction.	
3	5,62	442,61	1,533	11,7284	2,877	3,6103	0	3,6103	3,6103	5,0277	0,2131	94,9723	0	0,00334	0,0007	0	First gamma peak matches better at the bottom and peak positions match well. Alpha peak positions and shape are not matched well, due to relatively small fraction.	
4	10,64	441,96	1,571	11,9548	2,877	3,6104	0	3,6104	3,6104	8,6729	0,249	91,3271	0	0,00294	0,0009	0	Gamma peak shapes and positions of the function match better now. Alpha peaks match better.	
5	20,67	440,64	1,625	12,3468	2,877	3,6106	0	3,6106	3,6106	17,704	0,3287	82,296	0	0,00251	0,0002	0	Gamma peaks match well, alpha peaks match well.	
6	40,75	440,4	1,569	11,8692	2,878	3,6112	3,6337	3,613061	3,613061064	39,7925		55,2275	4,98	0,00247	0,0011	0,00394	Gamma peaks match well, alpha peaks match well.	
7	46	440,42	1,556	11,771	2,878	3,6112	3,6285	3,613942	3,613941683	44,9958		46,2872	8,717	0,00244	0,001	0,00369	Gamma peaks match well, alpha peaks match well.	
8	60,82	439,94	1,532	11,5516	2,878	3,6115	3,6328	3,616193	3,616193032	55,9739		34,3252	9,7001	0,00239	0,0014	0,00358	Gamma peaks match well, alpha peaks match well.	
9	68,81	440,06	1,53	11,448	2,878	3,6117	3,6329	3,617584	3,617583722	60,546		28,5041	10,9498	0,00236	0,0015	0,00345	Gamma peaks match well, alpha peaks match well.	
10	80,89	439,92	1,516	11,4287	2,878	3,6121	3,6334	3,61934	3,619339813	65,1077		23,0325	11,8598	0,00234	0,0017	0,00328	Gamma peaks match well, alpha peaks match well.	
11	100,97	439,99	1,526	11,4526	2,878	3,6132	3,6344	3,621845	3,621844865	70,0591		17,7317	12,2092	0,00229	0,0019	0,003	Gamma peaks match well, alpha peaks match well.	
12	121,04	439,89	1,53	11,4372	2,878	3,6148	3,6353	3,623554	3,623553618	72,8553		15,5537	11,5909	0,00229	0,0019	0,003	Gamma peaks match well, alpha peaks match well.	
13	173,34	439,98	4,88	11,685	2,878	3,6261	0	3,6261	3,6261	76,2116	1,1632	23,7884	0	0,00217	0,0034	0	Gamma peaks match well, alpha peaks match well.	Carbide peaks were detected.
14	217,84	440	4,901	11,7679	2,878	3,627	0	3,627	3,627	77,1809	1,198	22,8191	0	0,00212	0,0032	0	Gamma peaks match well, alpha peaks match well.	Carbide peaks were detected.
15	286,29	440	4,988	11,9574	2,878	3,6276	0	3,6276	3,6276	77,6685	1,2242	22,3315	0	0,00207	0,0031	0	Gamma peaks match well, alpha peaks match well.	Carbide peaks were detected.
16	354,69	440,04	4,94	11,8614	2,878	3,6277	0	3,6277	3,6277	78,2339	1,2433	21,7661	0	0,00201	0,0029	0	Gamma peaks match well, alpha peaks match well.	Carbide peaks were detected.
17	443,99	440,04	4,977	11,9057	2,878	3,6275	0	3,6275	3,6275	78,5898	1,2613	21,4102	0	0,00197	0,0027	0	Gamma peaks match well, alpha peaks match well.	Carbide peaks were detected.
18	591,74	439,97	4,983	11,9234	2,878	3,6272	0	3,6272	3,6272	79,1231	1,2843	20,8769	0	0,00192	0,0026	0	Gamma peaks match well, alpha peaks match well.	Carbide peaks were detected.
19	641,13	26,56	3,637	8,6789	2,86	3,5988	0	3,5988		80,0447	0,8973	19,9553	0	0,0019	0,0025	0	Gamma peaks match well, alpha peaks match well.	Carbide peaks were detected.

Figure D4: Documentation of the Rietveld refinements performed for 900-440.

General information			Evaluation fit		Lattice parameter in Å					Fraction in wt.%				Microstrain			Visual fit	Comments
Nr.	Holding time in s	Temperature in °C	Sigma	Rwp	Alpha	Gamma	Gamma+	Average gamma	Relative change gamma	Alpha	Error fraction alpha	Gamma	Gamma+	Alpha	Gamma	Gamma+		
1	-10,31	900,16	1,485	12,4663	0	3,6482	0	3,6482		0	0	100	0	0	6E-06	0	First gamma peak is broader at the bottom but peak positions match okay.	Ferrite peaks are visible.
2	3,24	412,99	1,532	11,5481	2,876	3,6078	0	3,6078	3,6078	3,6948	0,2914	96,3052	0	0,00399	0,0008	0	First gamma peak is broader at the bottom but peak positions match okay. Alpha peak positions and shape are not matched well, due to relatively small fraction.	
3	6,27	412,28	1,494	11,2673	2,876	3,6077	0	3,6077	3,6077	4,9345	0,2077	95,0655	0	0,0037	0,0009	0	First gamma peak matches better at the bottom and peak positions match well. Alpha peak positions and shape are not matched well, due to relatively small fraction.	
4	16,37	410,86	1,56	11,6997	2,875	3,6075	0	3,6075	3,6075	9,8965	0,2461	90,1035	0	0,003	0,0001	0	Gamma peak shapes and positions of the function match better now. Alpha peaks match better.	
5	26,48	410,38	1,474	10,9947	2,876	3,6077	0	3,6077	3,6077	17,323	0,2902	82,677	0	0,00297	0,0004	0	Gamma peaks match well, alpha peaks match well.	
6	36,59	410,41	1,478	10,9739	2,876	3,6081	0	3,6081	3,6081	26,1381	0,357	73,8619	0	0,00298	0,0008	0	Gamma peaks match well, alpha peaks match well.	
7	46,69	410,46	1,476	10,9397	2,876	3,6082	3,6362	3,609256	3,609255721	35,2595		62,2996	2,441	0,00297	0,0014	0,00586	Gamma peaks match well, alpha peaks match well.	
8	58,82	410	1,477	10,9244	2,876	3,6082	3,6339	3,610304	3,610303776	45,1789		50,3335	4,4876	0,00296	0,0012	0,00471	Gamma peaks match well, alpha peaks match well.	
9	66,91	409,94	1,456	10,7591	2,876	3,6081	3,6248	3,610761	3,610761051	50,7671		41,388	7,845	0,00292	0,0012	0,0058	Gamma peaks match well, alpha peaks match well.	
10	87,12	409,96	1,431	10,5595	2,877	3,6083	3,6305	3,613717	3,613717211	61,4185		29,1669	9,4146	0,00288	0,0014	0,0047	Gamma peaks match well, alpha peaks match well.	Carbide peaks were detected.
11	107,33	410,03	1,452	10,658	2,876	3,6078	3,627	3,615141	3,61514126	68,3052		19,576	12,1187	0,00286	0,0015	0,00507	Gamma peaks match well, alpha peaks match well.	Carbide peaks were detected.
12	127,55	410,04	1,433	10,5375	2,876	3,6082	3,6307	3,618329	3,618328949	72,7392		14,9886	12,2721	0,00283	0,0017	0,00439	Gamma peaks match well, alpha peaks match well.	Carbide peaks were detected.
13	148,07	410,01	4,545	10,722	2,876	3,6078	3,63	3,620114	3,620113999	75,8872		10,7378	13,375	0,00279	0,0017	0,00439	Gamma peaks match well, alpha peaks match well.	Carbide peaks were detected.
14	192,72		4,594	10,8493	2,876	3,6096	3,6338	3,623638	3,623638299	79,367		8,6639	11,9691	0,00274	0,0022	0,00374	Gamma peaks match well, alpha peaks match well.	Carbide peaks were detected.
15	241,17	409,87	4,572	10,8189	2,876	3,6106	3,6324	3,625817	3,625817413	81,1163		5,702	13,1817	0,0027	0,0023	0,00381	Gamma peaks match well, alpha peaks match well.	Carbide peaks were detected.
16	315,82	410,06	4,583	10,8869	2,876	3,618	3,6368	3,627578	3,627577565	82,2974		8,6841	9,0185	0,00265	0,0031	0,00347	Gamma peaks match well, alpha peaks match well.	Carbide peaks were detected.
17	424,87	409,98	4,596	10,9085	2,876	3,6285	0	3,6285	3,6285	83,0081	1,4001	16,9919	0	0,0026	0,0039	0	Gamma peaks match well, alpha peaks match well.	Carbide peaks were detected.
18	577,82	409,97	4,593	10,9054	2,876	3,629	0	3,629	3,629	83,4864	1,4225	16,5136	0	0,00255	0,0037	0	Gamma peaks match well, alpha peaks match well.	Carbide peaks were detected.
19	611,72	25,44	3,53	8,2832	2,861	3,6035	0	3,6035		84,4927	1,0451	15,5073	0	0,00248	0,0034	0	Gamma peaks match well, alpha peaks match well.	Carbide peaks were detected.

Figure D5: Documentation of the Rietveld refinements performed for 900-410.

General information			Evaluation fit		Lattice parameter in Å					Fraction in wt.%				Microstrain			Visual fit	Comments
Nr.	Holding time in s	Temperature in °C	Sigma	Rwp	Alpha	Gamma	Gamma+	Average gamma	Relative change gamma	Alpha	Error fraction alpha	Gamma	Gamma+	Alpha	Gamma	Gamma+		
1	-9,99	900,02	1,899	15,9936	0	3,6514	0	3,6514		0	0	100	0	0	6E-06	0	First gamma peak is broader at the bottom but peak positions match okay.	Ferrite peaks are visible.
2	4,07	383,24	1,361	10,4253	2,875	3,6062	0	3,6062	3,6062	2,5337	0,1396	97,4663	0	0,00266	0,0004	0	First gamma peak is broader at the bottom but peak positions match okay. Alpha peak positions and shape are not matched well, due to relatively small fraction.	
3	7,58	381,79	1,476	11,1485	2,875	3,6058	0	3,6058	3,6058	3,2894	0,2266	96,7106	0	0,003	0,0007	0	First gamma peak is broader at the bottom but peak positions match okay. Alpha peak positions and shape are not matched well, due to relatively small fraction.	
4	12,6	381,19	1,572	11,8194	2,877	3,6057	0	3,6057	3,6057	5,2982	0,2339	94,7018	0	0,00509	0,0009	0	First gamma peak matches better at the bottom and peak positions match well. Alpha peak positions and	
5	22,63	380,49	1,57	11,7515	2,876	3,6058	0	3,6058	3,6058	10,1203	0,265	89,8797	0	0,00401	0,0009	0	Gamma peak shapes and positions of the function	Carbide peaks were detected.
6	42,7	380,31	1,554	11,5455	2,876	3,6061	0	3,6061	3,6061	27,4235	0,5503	72,5765	0	0,00355	0,0007	0	Gamma peaks match well, alpha peaks match well.	Carbide peaks were detected.
7	62	379,88	1,557	11,619	2,876	3,6064	0	3,6064	3,6064	45,3042	0,5568	54,6958	0	0,00349	0,0015	0	Gamma peaks match well, alpha peaks match well.	Carbide peaks were detected.
8	62,78	380,02	1,544	11,4461	2,876	3,6064	0	3,6064	3,6064	45,9285	0,7888	54,0715	0	0,0035	0,0015	0	Gamma peaks match well, alpha peaks match well.	Carbide peaks were detected.
9	82,85	379,95	1,487	11,0467	2,876	3,606	3,6283	3,609171	3,609170691	57,8242		36,1791	5,9967	0,00348	0,0014	0,00823	Gamma peaks match well, alpha peaks match well.	Carbide peaks were detected.
10	102,92	379,78	1,478	10,9588	2,876	3,606	3,6275	3,610859	3,610859424	65,9861		26,2772	7,7367	0,00345	0,0016	0,00734	Gamma peaks match well, alpha peaks match well.	Carbide peaks were detected.
11	122,99	380,01	1,485	10,95	2,876	3,6059	3,6277	3,612616	3,612615602	71,3996		19,7899	8,8105	0,0034	0,0017	0,00688	Gamma peaks match well, alpha peaks match well.	Carbide peaks were detected.
12	137,15	380,01	1,474	10,9	2,876	3,6059	3,6278	3,613819	3,613818918	74,1824		16,4821	9,3355	0,0034	0,0018	0,00665	Gamma peaks match well, alpha peaks match well.	Carbide peaks were detected.
13	163,6	379,93	4,709	11,153	2,876	3,6057	3,6278	3,616172	3,616172256	77,9821		11,5846	10,4334	0,0034	0,0018	0,0064	Gamma peaks match well, alpha peaks match well.	Carbide peaks were detected.
14	186,15	380,13	4,627	11,0427	2,876	3,6053	3,6287	3,617635	3,617635112	80,4451		9,2467	10,3082	0,00334	0,0018	0,00574	Gamma peaks match well, alpha peaks match well.	Carbide peaks were detected.
15	208,9	380,02	4,63	11,0619	2,876	3,6053	3,6292	3,619208	3,619207678	82,0629		7,4993	10,4378	0,00332	0,0019	0,0056	Gamma peaks match well, alpha peaks match well.	Carbide peaks were detected.
16	312,3	380,08	4,68	11,1716	2,876	3,6085	3,6368	3,624389	3,624388911	85,7915		6,2312	7,9773	0,00327	0,0031	0,00454	Gamma peaks match well, alpha peaks match well.	Carbide peaks were detected.
17	403,1	380,01	4,681	11,1734	2,876	3,6259	0	3,6259	3,6259	87,0029	1,8517	12,9971	0	0,00322	0,0055	0	Gamma peaks match well, alpha peaks match well.	Carbide peaks were detected.
18	584,35	380,02	4,722	11,1287	2,876	3,6284	0	3,6284	3,6284	88,1135	1,9424	11,8865	0	0,00318	0,0051	0	Gamma peaks match well, alpha peaks match well.	Carbide peaks were detected.
19	637,6	26,49	3,781	8,9211	2,861	3,6069	0	3,6069		89,4505	1,5498	10,5495	0	0,00313	0,0044	0	Gamma peaks match well, alpha peaks match well.	Carbide peaks were detected.

Figure D6: Documentation of the Rietveld refinements performed for 900-380.

E Prior austenite grain size distribution

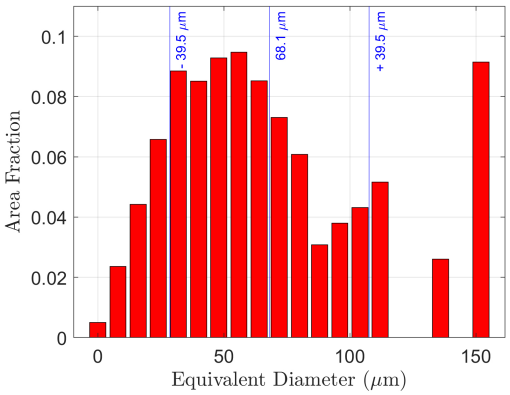

(a) 1100-410

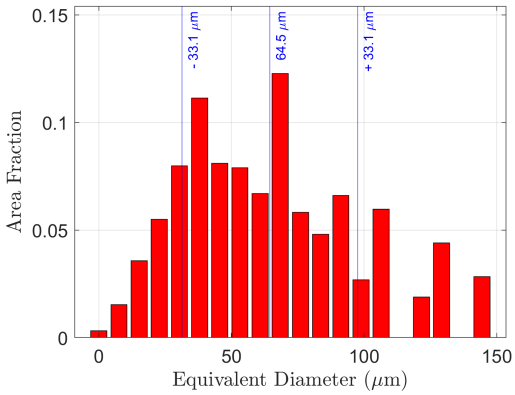

(b) 1100-360

Figure E1: Prior austenite grain size distribution in 1100-410 and 1100-360.

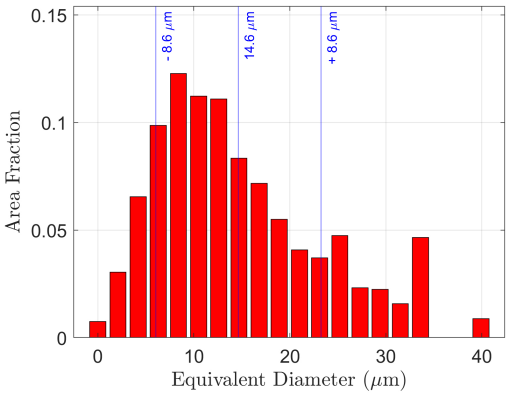

(a) 900-410

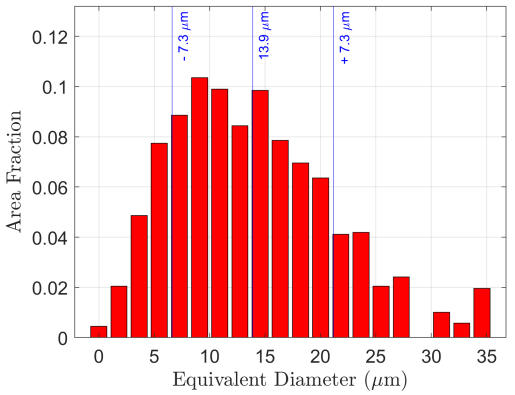

(b) 900-360

Figure E2: Prior austenite grain size distribution in 900-410 and 900-360.

F Ferrite remaining after austenitization

Figure F1 and Figure F2 present XRD patterns recorded at the end of the austenitization treatment for all six experiments. Very small ferrite peaks can be detected in Figure F1a, Figure F1b, Figure F1c, Figure F2b and Figure F2c when the XRD patterns are analyzed on the logarithmic scale. The ferrite peaks are indicated by arrows. It is visible that the dimensions of the ferrite peaks do not differ significantly in the five experiments. In Figure F2a no ferrite peaks can be detected.

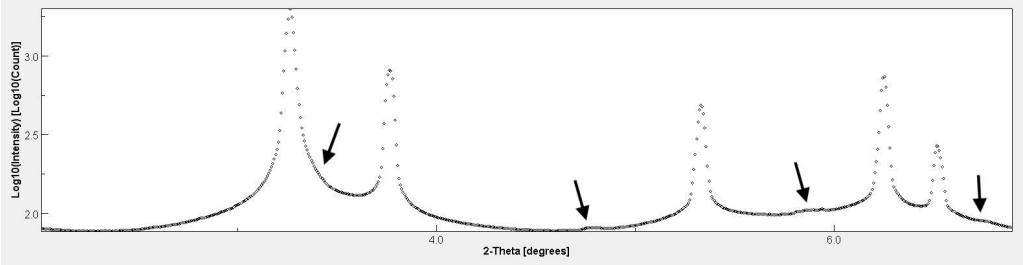

(a) 1100-440

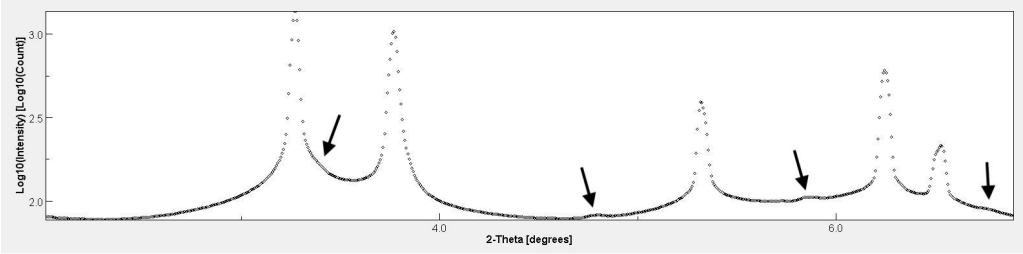

(b) 1100-410

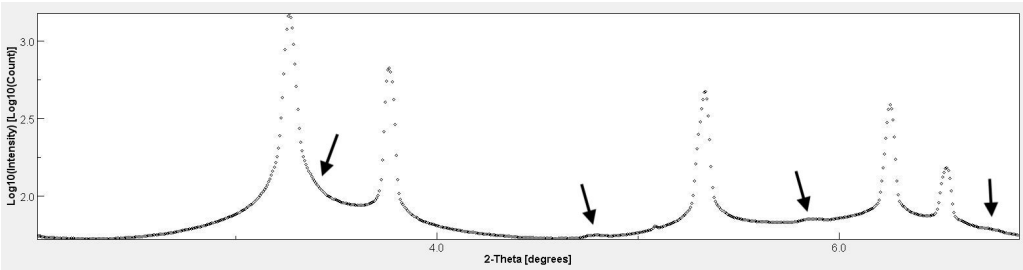

(c) 1100-380

Figure F1: Ferrite peaks in XRD patterns recorded at the end of the austenitization treatment in experiments 1100-440, 1100-410 and 1100-380.

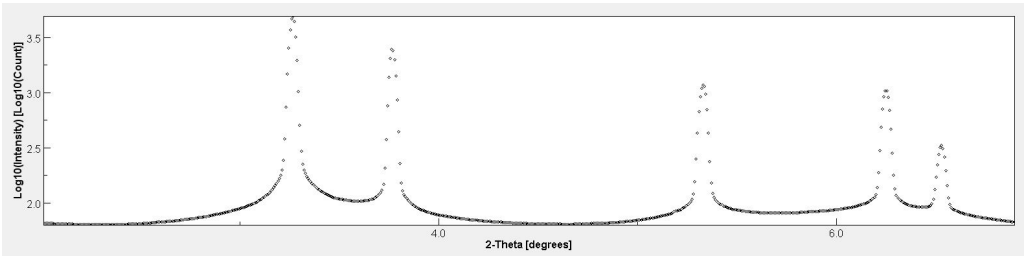

(a) 900-440

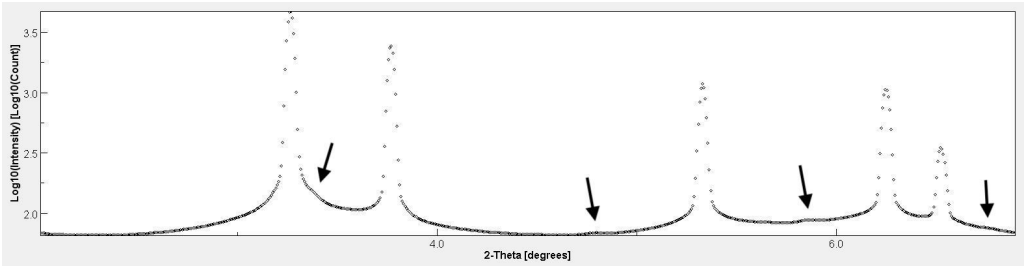

(b) 900-410

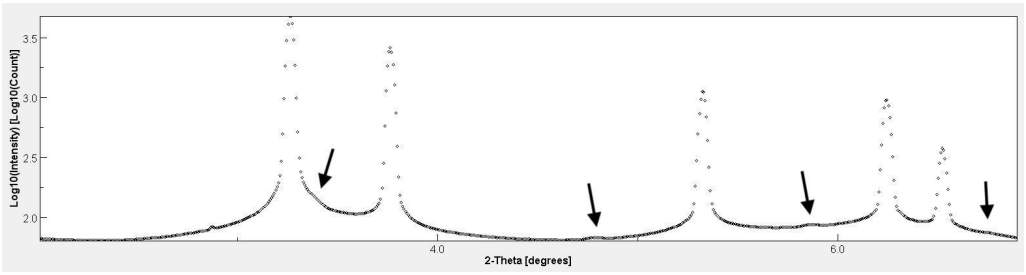

(c) 900-360

Figure F2: Ferrite peaks in XRD patterns recorded at the end of the austenitization treatment in experiments 900-440, 900-410 and 900-380.

G Carbide fraction

Figure G1 presents XRD patterns on logarithmic scale recorded at the end of the isothermal holding for all six experiments. Arrows point to carbide peak positions. Carbide peaks can be observed in Figure G1c, Figure G1d, Figure G1e and Figure G1f. The carbide peaks observed in the XRD patterns of the experiments transformed at 380°C appear to be larger than the carbide peaks present in the XRD patterns of the experiments transformed at 410°C. Figure G2 shows enlarged parts of the images presented in Figure G1 and it can be observed that all XRD patterns exhibit carbide peaks. It is visible that the carbide peaks become more pronounced as the transformation temperature is decreased.

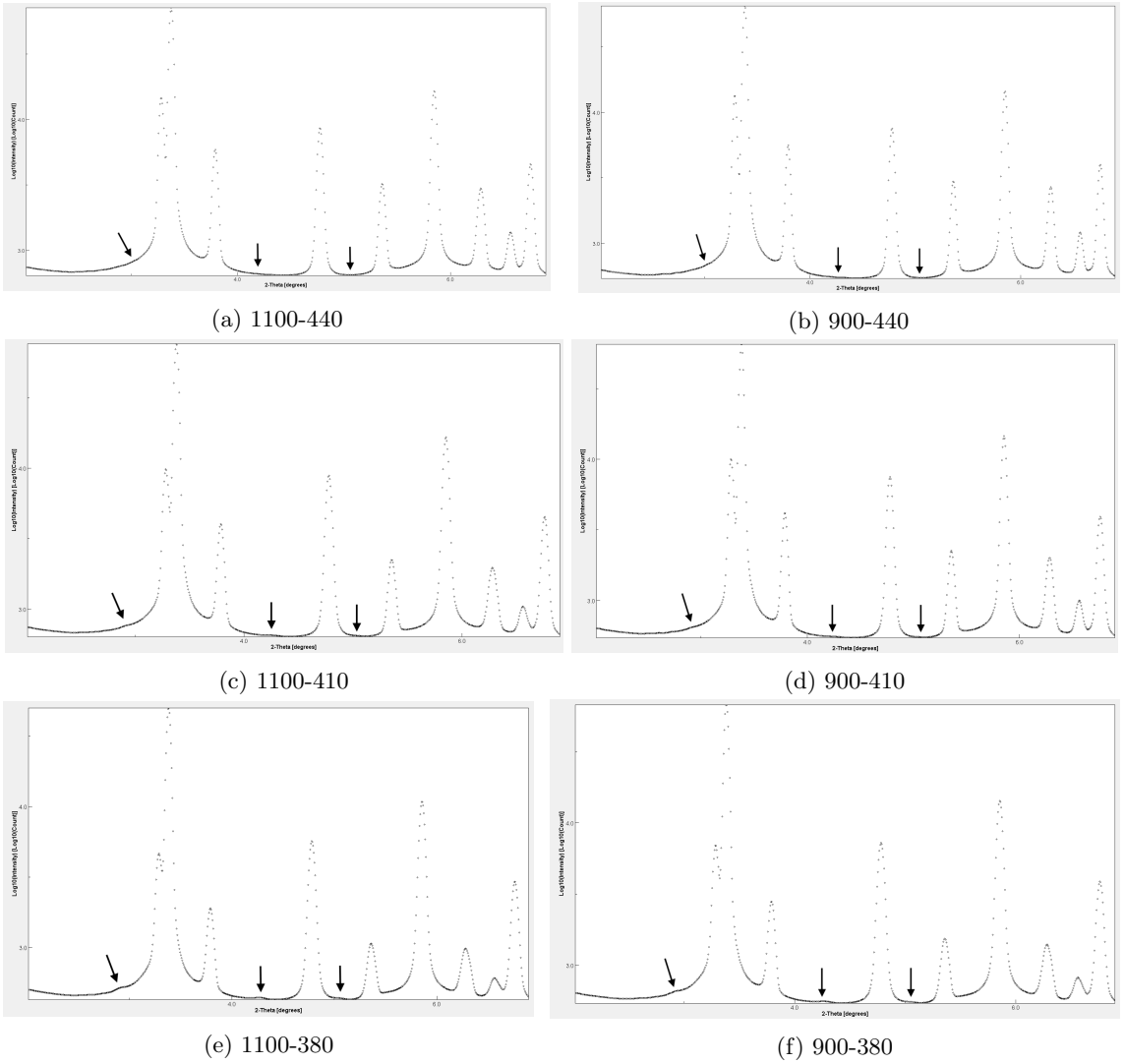

(a) 1100-440 (b) 900-440

(c) 1100-410 (d) 900-410

(e) 1100-380 (f) 900-380

Figure G1: Carbide peaks present in XRD patterns recorded at the end of the isothermal phase transformation.

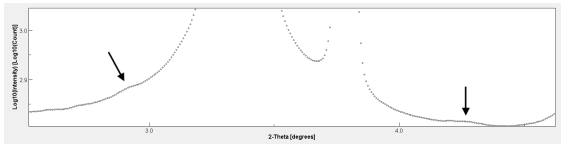

(a) 1100-440

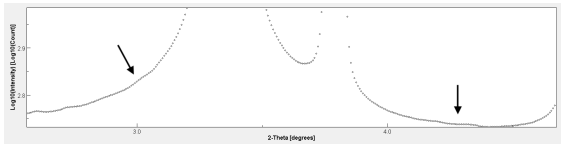

(b) 900-440

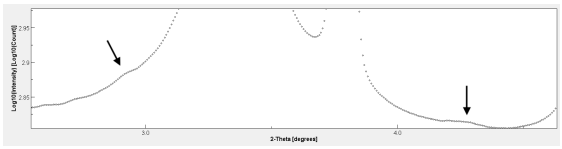

(c) 1100-410

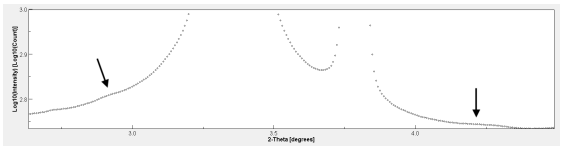

(d) 900-410

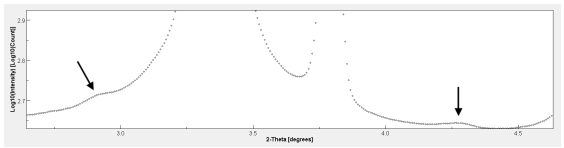

(e) 1100-380

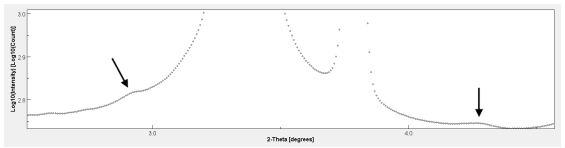

(f) 900-380

Figure G2: Enlarged parts of the XRD patterns presented in Figure G1.

H Example of fitting error

The model used for the simulations determines ΔQ based on the bainitic ferrite fraction vs. time curves provided as data input. It determines the activation energies for grain boundary and autocatalytic nucleation, as well as the bainitic ferrite fractions that have formed at each nucleation site. During the refinement of the XRD patterns, it is not possible to distinguish between the bainitic ferrite fraction and the ferrite fraction that was present before the onset of the phase transformation to bainite in the determined BCC phase fractions. Therefore, the initial BCC fraction is unrealistically high, resulting in a high transformation rate followed by an unexpected drop at the beginning of the phase transformation to bainite, as it is presented in Figure H1.

The fraction of bainitic ferrite formed at the beginning of the phase transformation is determined by grain boundary nucleation. The specimens with fine prior austenite grains provide many potential nucleation sites at prior austenite grain boundaries and hence a relatively high fraction of bainitic ferrite could form by grain boundary nucleation. However, the fraction of bainitic ferrite that can form by grain boundary nucleation is much lower in the specimens with coarse prior austenite grains, which is the reason why the presence of ferrite at the beginning of the phase transformation has a significant effect on ΔQ predicted for this experiment group. The model compensates for the initially high BCC fraction by predicting an increased formation of bainitic ferrite by grain boundary nucleation and hence a very low activation energy for grain boundary nucleation, Q_{GB}, in the samples with coarse prior austenite grains. By simultaneously fitting the bainitic ferrite vs. time curves for experiments with fine and coarse prior austenite grains at the same transformation temperature, the initial part of the curve of the experiments with coarse prior austenite grains can be disregarded, which made it possible to determine ΔQ at a specific transformation temperature.

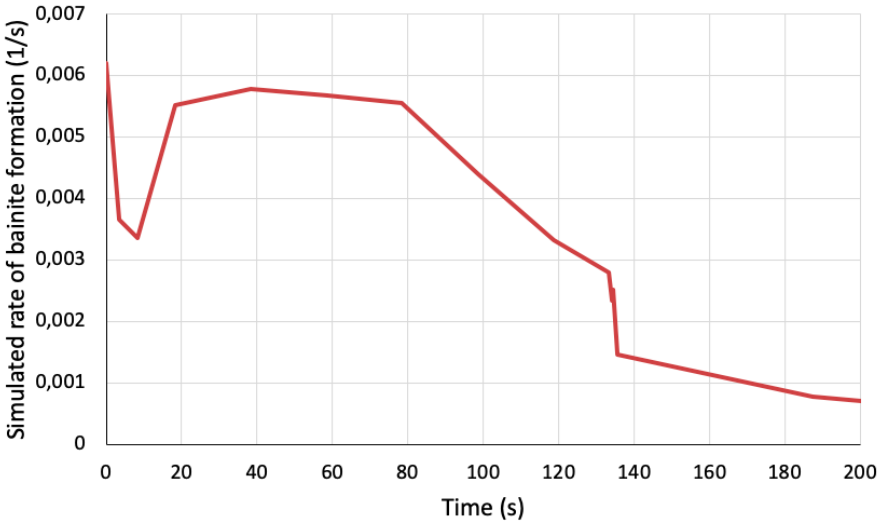

Figure H1: Simulated transformation rate of bainitic ferrite in 1100-440.